

THESIS FOR THE DEGREE OF DOCTOR OF PHILOSOPHY

Millimeter-wave Communication and Radar Sensing
— Opportunities, Challenges, and Solutions

Sining An



Microwave Electronics Laboratory
Department of Microtechnology and Nanoscience
Chalmers University of Technology
Gothenburg, Sweden 2021

Millimeter-wave Communication and Radar Sensing — Opportunities, Challenges, and Solutions

Sining An

ISBN 978-91-7905-479-3

© Sining An, 2021

Doktorsavhandlingar vid Chalmers tekniska högskola
Ny series nr 4946
ISSN 0346-718X

Chalmers University of Technology
Department of Microtechnology and Nanoscience – MC2
Microwave Electronics Laboratory
SE-412 96 Goteborg, Sweden
Phone: 46 (0) 31 772 10 00

Printed by Chalmers Reproservice
Gothenburg, Sweden 2021

To my family.

Abstract

With the development of communication and radar sensing technology, people are able to seek a more convenient life and better experiences. The fifth-generation (5G) mobile network provides high-speed communication and internet services with a data rate up to several gigabits per second (Gbps). In addition, 5G offers great opportunities for emerging applications, for example, manufacturing automation with the help of precise wireless sensing. For future communication and sensing systems, increasing capacity and accuracy is desired, which can be realized at the millimeter-wave spectrum from 30 GHz to 300 GHz with several tens of GHz available bandwidth. Wavelength reduces at a higher frequency. This implies more compact transceivers and antennas, high sensing accuracy and imaging resolution. Challenges arise with these application opportunities when it comes to realizing prototypes or demonstrators in practice. This thesis proposes some solutions addressing such challenges in a laboratory environment.

High data rate millimeter-wave transmission experiments have been demonstrated with the help of advanced instrumentations. These demonstrations show the potential of transceiver chipsets. On the other hand, the real-time communication demonstrations are limited to either low modulation order signals or low symbol rate transmissions. The reason for that is the lack of commercially available high-speed analog-to-digital converters (ADCs); therefore, conventional digital synchronization methods are difficult to implement in real-time systems at very high data rates. In this thesis, two synchronous baseband receivers are proposed with carrier recovery subsystems that only require low-speed ADCs [A][B].

Besides synchronization, high-frequency signal generation is also a challenge in millimeter-wave communications. The frequency divider is a critical component of a millimeter-wave frequency synthesizer. Having both a wide locking range and high working frequencies is a challenge. In this thesis, a tunable delay gated ring oscillator topology is proposed for dual-mode operation and bandwidth extension [C].

Millimeter-wave radar offers advantages for high accuracy sensing. Traditional millimeter-wave radar with frequency-modulated continuous-wave (FMCW), or continuous-wave (CW), all have their disadvantages. Typically, the FMCW radar cannot share the spectrum with other FMCW radars. With limited bandwidth, the number of FMCW radars that could coexist in the same area is limited. CW radars have a limited ambiguous distance of a wavelength. In this thesis, a phase-modulated radar with micrometer accuracy is presented [D]. It is applicable in a multi-radar scenario without occupying more bandwidth, and its ambiguous distance is also much larger than the CW radar. Orthogonal frequency-division multiplexing (OFDM) radar has similar properties. However, its traditional fast calculation method, inverse fast Fourier

transform (IFFT), limits its measurement accuracy. In this thesis, an accuracy enhancement technique is introduced to increase the measurement accuracy up to the micrometer level [E].

Keywords: Millimeter-wave, communication system, mobile network, high data rate, carrier recovery, synchronization, dynamic, frequency divider, SiGe, BiCMOS, wide-band, radar, sensing, micrometer, range accuracy, monitoring, distance measurement, phase modulated, OFDM, IFFT.

List of Publications

Appended papers

The thesis is based on the work contained in the following papers:

- [A] *S. An*, Z. S. He, J. Chen, H. Han, J. An and H. Zirath, "A Synchronous Baseband Receiver for High-Data-Rate Millimeter-Wave Communication Systems," in *IEEE Microwave and Wireless Components Letters*, vol. 29, no. 6, pp. 412-414, June 2019, doi: 10.1109/LMWC.2019.2910661.
- [B] *S. An*, Z. S. He, J. Li, X. Bu and H. Zirath, "Coded Pilot Assisted Baseband Receiver for High Data Rate Millimeter-Wave Communications," in *IEEE Transactions on Microwave Theory and Techniques*, vol. 68, no. 11, pp. 4719-4727, Nov. 2020, doi: 10.1109/TMTT.2020.2993789.
- [C] *S. An*, Z. S. He, F. Dielacher and H. Zirath, "A D-Band Dual-Mode Dynamic Frequency Divider in 130-nm SiGe Technology," in *IEEE Microwave and Wireless Components Letters*, vol. 30, no. 12, pp. 1169-1172, Dec. 2020, doi: 10.1109/LMWC.2020.3033076.
- [D] *S. An*, Z. S. He, J. Li, J. An and H. Zirath, "Micrometer Accuracy Phase Modulated Radar for Distance Measurement and Monitoring," in *IEEE Sensors Journal*, vol. 20, no. 6, pp. 2919-2927, 15 March 15, 2020, doi: 10.1109/JSEN.2019.2955746.
- [E] J. Li, *S. An*, J. An, H. Zirath and Z. S. He, "OFDM Radar Range Accuracy Enhancement Using Fractional Fourier Transformation and Phase Analysis Techniques," in *IEEE Sensors Journal*, vol. 20, no. 2, pp. 1011-1018, 15 Jan. 15, 2020, doi: 10.1109/JSEN.2019.2946003.

Other papers

The following papers have been published but are not included in the thesis. The content partially overlaps with the appended papers or is outside the scope of the thesis.

- [a] *S. An*, J. Chen, Z. He, S. Wang and H. Zirath, "A 40 Gbps DQPSK modem for millimeter-wave communications," *2015 Asia-Pacific Microwave Conference (APMC)*, Nanjing, China, 2015, pp. 1-3, doi: 10.1109/APMC.2015.7411747.
- [b] *S. An*, Z. S. He, J. Chen, Y. Li and H. Zirath, "An 8 Gbps E-band QAM transmitter using symbol-based outphasing power combining technique," *2017 IEEE International*

Symposium on Radio-Frequency Integration Technology (RFIT), Seoul, Korea (South), 2017, pp. 150-152, doi: 10.1109/RFIT.2017.8048232.

- [c] S. Wang, *S. An*, X. Miao, Y. Ma and S. Luo, "Compressed Sensing Assisted Joint Channel Estimation and Detection for DS-CDMA Uplink," in *IEEE Communications Letters*, vol. 19, no. 10, pp. 1730-1733, Oct. 2015, doi: 10.1109/LCOMM.2015.2439036.
- [d] Z. S. He, *S. An*, J. Liu and C. Jin, "Variable High Precision Wide D-Band Phase Shifter," in *IEEE Access*, vol. 8, pp. 140438-140444, 2020, doi: 10.1109/ACCESS.2020.3012596.
- [e] T. Huang, *S. An*, J. Bergsten, S. He and N. Rorsman, 2019. A power detector based on GaN high-electron-mobility transistors for a gigabit on-off keying demodulator at 90 GHz. *Japanese Journal of Applied Physics*, 2019 May 20, 58(SC):SCCD19.
- [f] Z. S. He, C. Jin, *S. An*, L. Kong and J. Liu, "Integrated-EBG Ridge Waveguide and Its Application to an E-Band Waveguide 32×32 Slot Array Antenna," in *IEEE Open Journal of Antennas and Propagation*, vol. 1, pp. 456-463, 2020, doi: 10.1109/OJAP.2020.3017887.
- [g] C. Jin, Q. Lv, B. Zhang, J. Liu, *S. An*, Z. S. He and Z. Shen, "Ultra-Wide-Angle Bandpass Frequency Selective Surface," in *IEEE Transactions on Antennas and Propagation*, doi: 10.1109/TAP.2021.3061144.
- [h] A. Hassona, V. Vassilev, A. U. Zaman, Y. Yan, *S. An*, Z. S. He, O. Habibpour, S. Carpenter, M. Bao and H. Zirath, "Nongalvanic Generic Packaging Solution Demonstrated in a Fully Integrated D-Band Receiver," in *IEEE Transactions on Terahertz Science and Technology*, vol. 10, no. 3, pp. 321-330, May 2020, doi: 10.1109/TTHZ.2020.2972362.

Thesis

- [i] S. An, "Multi-Gigabaud Solutions for Millimeter-wave Communication," Tekn. Lic. Thesis, Dept. of Microtechnology and Nanoscience, Chalmers University of Technology, Gothenburg, Sweden, 2019.

As part of the author's doctoral studies, some of the work presented in this thesis has previously been published in [i]. Figures, tables and text from [i] may therefore be fully or partially reproduced in this thesis.

Abbreviations

2/3/4/5G	Second/Third/Fourth/Fifth-generation of mobile communications technology
AC	Alternating current
ADC	Analog to digital converter
APP	Application
ASK	Amplitude shift keying
ATM	Automated teller machine
AWG	Arbitrary waveform generator
BER	Bit error rate
BERT	Bit error rate tester
BPF	Bandpass filter
BPSK	Binary phase shift keying
CDMA	Code-division multiple access
CR	Carrier recovery
CT	Computed tomography
CW	Continuous wave
DAC	Digital to analog converter
DC	Direct current
DQPSK	Differential quadrature phase shift keying
DSP	Digital signal processing
DSSS	Direct sequence spread spectrum
EVM	Error vector magnitude
FMCW	Frequency-modulated continuous-wave
FPGA	Field programmable gate array
FWMF	full waveform matched filter
GPRS	General Packet radio services
HD	High-definition
IF	Intermediate frequency
IFFT	Inverse fast Fourier transform
ILFD	Injection-locked frequency divider
IoT	Internet of things
LNA	Low noise amplifier
LO	Local oscillator
LPF	Low pass filter
MIMO	Multiple input and multiple output
Modem	Modulator and demodulator

NCO	Numerical controlled oscillator
OFDM	Orthogonal frequency division multiplexing
OOK	On-off keying
PAM	Pulse amplitude modulation
PFD	Phase/frequency detector
PLL	Phase-locked loop
PN	Pseudorandom noise
PNCP	Pseudorandom noise coded pilot
PRBS	Pseudo-random binary sequence
QAM	Quadrature amplitude modulation
QPSK	Quadrature phase shift keying
RAN	Radio access network
RBPM	Random binary phase modulated
RF	Radio frequency
RX	Receiver
SAW	Surface acoustic wave
SNR	Signal-to-noise ratio
SSB	Single side band
TDGRO	Tunable delay gated ring oscillator
TL	Transmission line
TX	Transmitter
VCO	Voltage control oscillators

Contents

Abstract v

List of Publications vii

Abbreviations..... ix

1	Introduction	1
1.1	Background.....	1
1.2	Mobile network evolution.....	2
1.3	Opportunities and challenges for millimeter-wave communications	3
1.4	Overview of published millimeter-wave communication demonstrators	5
1.5	Overview of industry revolution	6
1.6	Overview of non-contacting sensing technology.....	6
1.7	Thesis scope and outline.....	8
2	Millimeter-wave Wideband Synchronous Receivers	9
2.1	Overview of published millimeter-wave transmissions	10
2.2	Considerations of the pilot tone insertion.....	12
2.3	The proposed millimeter-wave communication system.....	13
2.4	Direct sequence spread spectrum	14
2.5	Advantages of using PNCP	16
2.6	Two carrier recovery subsystems	17
2.6.1	Carrier recovery subsystem with the CW pilot	17
2.6.2	Carrier recovery subsystem with the PNCP	18
2.7	System limitations	19
2.8	Performance verification and discussion	21
3	Millimeter-wave Frequency Divider	27
3.1	Millimeter-wave frequency synthesizer	28
3.2	Overview of frequency dividers	29
3.3	Proposed frequency divider topology	31
3.4	Circuit structure and tunable delay simulation	33
3.5	Performance verification and discussion	35
4	Millimeter-wave Radar Sensing	39
4.1	Overview of millimeter-wave radar systems	40

4.2	Three radar principles	41
4.2.1	CW radar	41
4.2.2	Phase modulated radar	41
4.2.3	OFDM radar	42
4.3	Proposed radar systems	44
4.3.1	Phase modulated radar system.....	44
4.3.2	OFDM radar system.....	47
4.3.3	Fine estimation.....	48
4.3.4	Multi-user interference resistance	49
4.4	Performance verification and discussion	49
4.4.1	Coarse estimation	50
4.4.2	Fine estimation.....	51
4.4.3	Discussion	52
5	Conclusions and future work.....	53
5.1	Conclusions	53
5.2	Future work	54
	Acknowledgment.....	55
	References	57

Chapter 1

Introduction

1.1 Background

With the development of communication technology, the daily life around us becomes more and more convenient. It is nothing but normal for us to shop online, chat with friends through Facetime, watch high-definition (HD) movies at home, get cash from an automated teller machine (ATM), reply to an e-mail on transportations. With the help of all kinds of software applications (APPs), we are equipped with a “superpower” of controlling things at a distance. For example, only with several taps on the cellphone from the office, the vacuum at home could start cleaning, the refrigerator could report back if the vegetables inside are fresh or not, and it can even give a suggested recipe for the dinner. Credit cards, metro tickets, maps, fictions, movies etc. are all put together in a single cellphone waiting for your requests at any time.

The mobile network has developed to its fifth-generation. People are getting more and more used to high-speed communication experience and want more of that. 5G services subscriptions are expected to reach 3.5 billion by the end of 2026 [1]. Besides providing the traditional mobile network and internet services, the 5G network has a great opportunity to open up new dimensions of use cases. The enhanced mobile broadband services will provide immersive experiences with augmented reality and virtual reality. Interactive, multiple-participant and remote applications will also be developed with 5G network. In the automotive areas, real-time vehicle to vehicle, and vehicle to infrastructure communications and interactions will be achieved with the help of 5G technologies. In the healthcare areas, the high-speed connection between doctors and patients can reduce traveling and make the best use of healthcare resources. With the 5G network, remote monitoring, medication, and remote operations become possible. In the manufacturing areas, 5G technology will permit the manufacturing industry to move from process automation to flow management and remote supervision, and ultimately cloud robotics and remote control. For energy and utilities, mobile broadband communications are already used extensively for metering and smart grid applications. 5G will enable sophisticated resource management and automation and increase the possibilities of machine intelligence and real-time control [2-6]. Besides high-speed communication, another key technology for realizing these applications is precise sensing.

Beyond the frequency that 5G is using now, 28 GHz and 32 GHz, the next frequency band of interest will be the millimeter-wave band. Millimeter-wave frequency band, from 30 to 300 GHz, offers several tens of GHz available bandwidth, enables the possibility to build compact ultra-fast data transmission systems. Besides the wide available bandwidth, it also has a short wavelength of several millimeters, enabling precise sensing opportunities.

1.2 Mobile network evolution

The capacity of communication networks developed rapidly in the past few decades. Taking the mobile networks as an example, the first-generation network was only able to provide voice call in 1983. In the 1990s, the second generation (2G) system was introduced, which started to provide multimedia message services through the digital cellular systems at a speed of 64 kbps. Then the 2.5G and the 2.75G networks, the 2G technology combined with general packet radio service (GPRS), improved the data rate up to 144 kbps. Next, the third generation (3G) technology was launched around the year 2000, which allows data services at a speed of 144 kbps to 384 kbps in broad coverage areas and a peak data rate of 2 Mbps in the local coverage area. The fourth-generation (4G) mobile system, launched in 2012, offers voice, data services, and multimedia services. The communication speed of the 4G network reaches up to 100 Mbps for quick-moving devices and 1 Gbps for slow-moving or stationary devices. The fifth-generation mobile network, launched in 2020, aims to achieve ultra-low latency around 1 ms, significantly fast data transmission at a maximum speed of several Gbps, and an increase of the total capacity by a thousand times [7-9].

The data volume is increasing exponentially. The data traffic of mobile networks per month increases 18 times compared to seven years ago, according to Ericsson mobility report 2020. Global total mobile data traffic is estimated to reach around 51 EB per month by the end of 2020 and is projected to grow by a factor of around 4.5 to reach 226 EB per month in 2026. Smartphone users to consume a global average of 24 GB per month in 2025 from 7.2 GB currently, as video usage increases and new services become available. The total number of cellular internet of things (IoT) connections is estimated to reach five billion by the end of 2025, from 1.3 billion by the end of 2019 [1][10]. The capacity enhancement of the communication network is a challenge.

The massive data increase brings great challenges to the radio access network (RAN). The three main transport mediums used in RAN are copper cables, optical fibers, and wireless links. Copper cables have been widely used for the past 100 years. With the growing demand for high data rate communications, copper cables become obsolete due to their narrow bandwidth and short transmission distance. On the other hand, optical fibers have become more and more popular for their large bandwidth and robust long-distance transmission. However, it is expensive and time-consuming to install optical fibers in the field. As a cost-efficient and flexible alternative of the fibers, wireless communication has been earning attention recently. However, wireless technologies need to offer comparable capacity as the fibers to take over the market eventually. In today's mobile networks, the mobile backhaul is evolving with a mixture of fiber and wireless links. More than 65 percent of all radio sites will be connected by microwave wireless links in 2022 [11].

1.3 Opportunities and challenges for millimeter-wave communications

The data rate in a communication system can be described as

$$W = K \times \log_2(m), \quad (1.1)$$

where W is the achievable data rate with the unit of bit per second (bps). K is the symbol rate. m is the modulation order stands for the total number of different symbols, which is also related to spectrum efficiency [12]. As a result, either using a higher modulation order signal or increasing the bandwidth can increase the data rate of a communication system.

The microwave bands, from 6 to 42 GHz, usually have a narrow bandwidth of several hundreds MHz due to the regulation, which limits the communication data rate. On the other hand, millimeter-wave bands (30 – 300 GHz) provide a great opportunity to realize high data rate communications. Millimeter-wave bands such as E-band (71-76 GHz, 81-86 GHz), D-band (110-170 GHz) and G-band (140-220 GHz) provide sufficient bandwidth to support tens of Gbps communications [13].

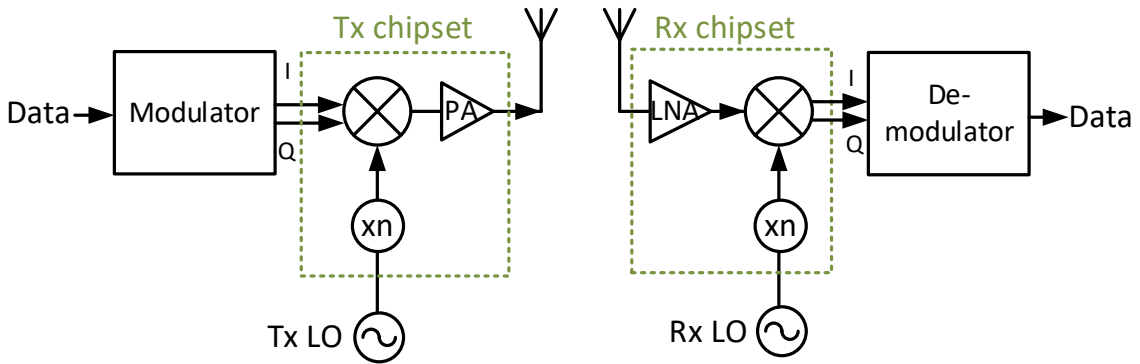


Fig. 1.1 A simplified block diagram of a communication system.

A simplified communication system structure is shown in Fig. 1.1. The user data is first modulated into two basebands I/Q channel orthogonal signal. Then the baseband signal will be up-converted to radio frequency (RF) and amplified before sent out. The up-conversion is achieved by mixing the baseband signal with the RF carrier signal. At the receiver side, the received signal gets amplified by a low noise amplifier (LNA). Then, it is down-converted by mixing with the carrier signal. Then the baseband I/Q signal will be demodulated to recover the transmitted information.

For the RF carrier signal, if it is at a low frequency, it can be directly generated by a local oscillator (LO). However, for frequencies above millimeter-wave, usually, a multiplier is needed to multiple a low-frequency carrier signal to the desired RF frequencies. In the published millimeter-wave transmitter and receiver frontend chips, multiplier with a multiplication factor of 3 and 6, or subharmonic mixers are widely used [14-16]. The millimeter-wave signal synthesis is a challenge.

Signal sources based on voltage control oscillators (VCOs) above millimeter-wave have been reported [17-20]. Free-running signal sources usually suffer from frequency fluctuation and drift. It is also sensitive to temperature or process variations. A phase-locked loop (PLL) is normally needed to stabilize the oscillation frequency and lower the phase noise [21-27]. A simplified PLL block diagram is shown in Fig. 1.2.

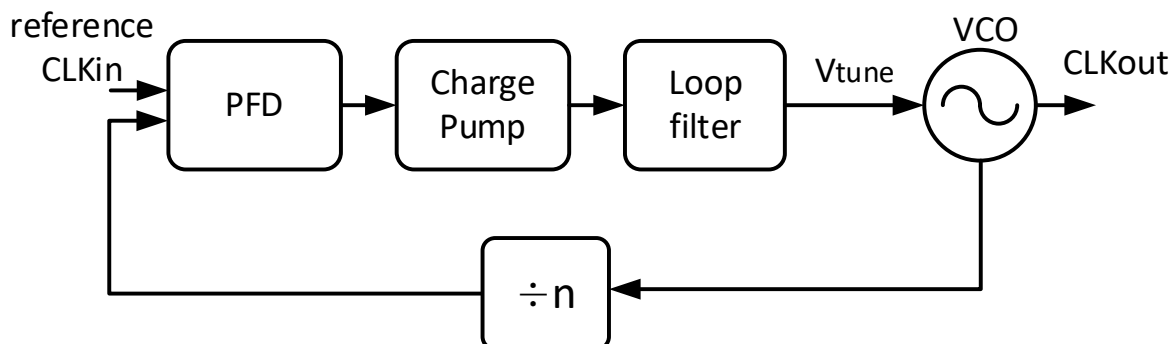


Fig. 1.2 A simplified PLL block diagram.

In a PLL block, a VCO generates the signal around the desired frequency. It is divided by a frequency divider to a low frequency and compared with a reference clock. A stable low-frequency LO is used as a reference. A phase/frequency detector (PFD) analysis the phase and frequency difference between the VCO and the reference LO. A charge pump converts the phase/ frequency difference information into a voltage signal. The loop filter placed after the charge pump controls the tuning voltage to tune the VCO. Inside a PLL block, the frequency divider is a key component that translates the oscillation frequency from the VCO output down to the reference frequency. For this purpose, frequency dividers should have a wide operational frequency band that covers the entire VCO operation frequency range.

In addition, to make good usage of the wide band spectrum in millimeter-wave, the transmitter and receiver need to have wide working bandwidth to handle the wide band signal. Besides, to increase the data rate, a higher modulation order signal needs to be used. In this case, the transmitter and the receiver need to be able to work with high modulation order signals, as well. As Fig. 1.1 shows, two individual LOs are used at the transmitter and receiver sides so that they are not synchronized. For demodulation, there are two kinds of signal detection methods, coherent detection and non-coherent detection [28]. For non-coherent detection, the carrier's phase is not recovered at the receiver side, so that no carrier synchronization is needed. However, the non-coherent detection is normally implemented with low modulation order signals, such as on-off keying (OOK), differential quadrature phase-shift keying (DQPSK), and amplitude-shift keying (ASK). The spectrum efficiency is limited by using low modulation order signals. For higher modulation order signals, such as sixteen quadrature amplitude modulation (16-QAM), or multi-carrier modulated signal, such as OFDM, coherent detection is needed. For coherent detection, the carrier phase synchronization is the major task of the receiver. As a result, a wide-band synchronous receiver is required to realize high data rate communication.

1.4 Overview of published millimeter-wave communication demonstrators

A summary of published millimeter-wave transmission experiments is shown in Fig. 1.3, including spectrum efficiency and the single-channel data rate. The published results can be categorized into three groups: transmission with shared LO, where the transmitter (TX) and the receiver (RX) are sharing a single LO source; off-line demodulation, where TX and RX use different LOs, and the demodulation is implemented in off-line digital signal processing (DSP) platforms; real-time transmission, where TX and RX use different LOs and the demodulation is implemented in real-time.

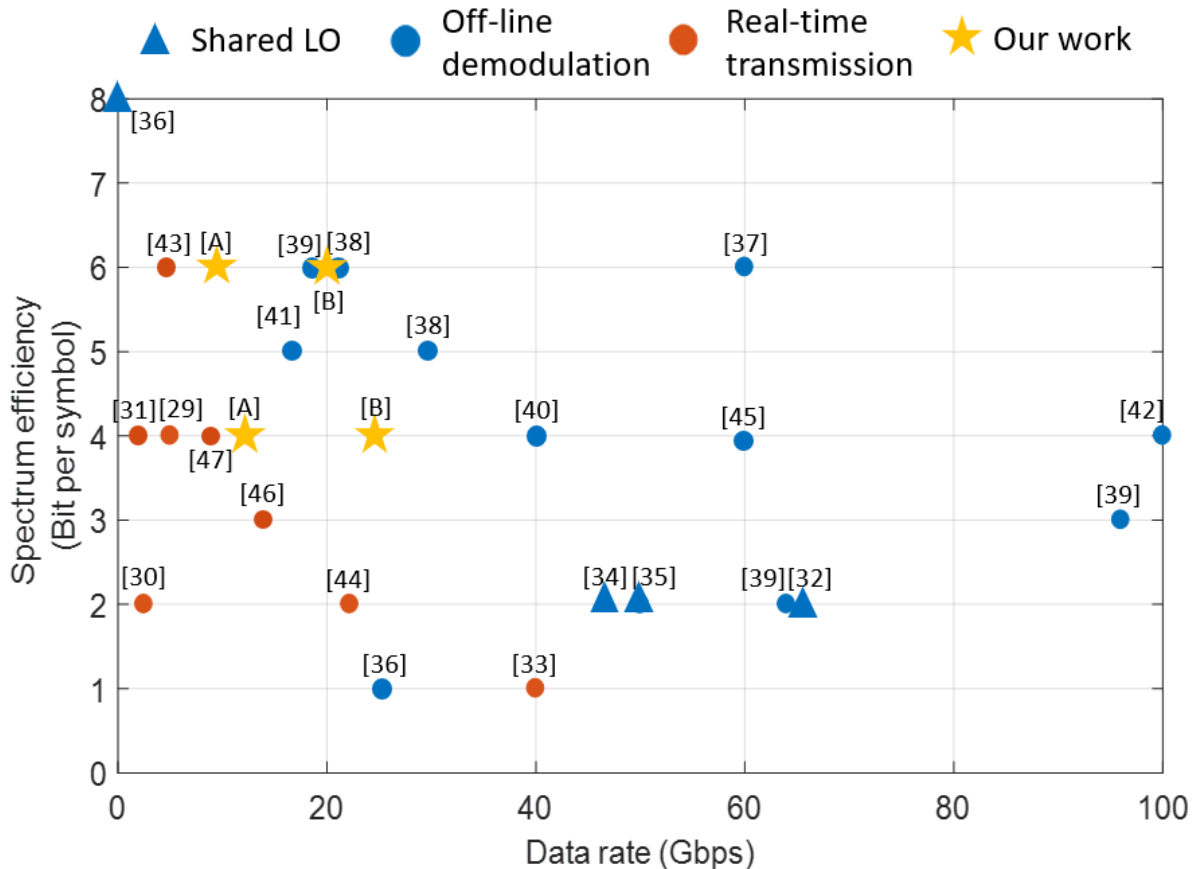


Fig. 1.3 An overview of published millimeter-wave communication demonstrators with a single carrier, single-polarization and single pair of transceiver modules.

With a shared LO source, data transmission up to 65 Gbps has been verified [32] [34-36]. Besides, with the help of offline digital signal processing, a 64-QAM signal with a data rate up to 60 Gbps has been transmitted over D-band [37]. Wireless data transmission at 240 GHz carrier frequency over a distance of 40 meters has been demonstrated with a 96 Gbps 8-PSK signal [39]. A 100 Gbps wireless transmission using 16-QAM over 2.22 meters is achieved [42]. These experiments exhibit the bandwidth potential of the transceiver chipsets.

In real-time transmission systems, lower modulation order signals such as ASK and OOK signal can be recovered by direct detection. BPSK and QPSK signals can be demodulated by using differential coding and detection. For higher-order QAM signals such as 16-QAM or 64-QAM,

DSP platforms are commonly needed to realize carrier recovery (CR). Normally CR is accomplished by analyzing the received IF signal. Due to the lack of high-speed analog to digital converters, the real-time transmissions with high modulation order (higher than 16-QAM) signals in DSP platforms have only been demonstrated with a data rate below 10 Gbps [48]. In papers [A] and [B], two synchronous baseband receivers are proposed. The synchronization is implemented in an analog-digital hybrid way.

1.5 Overview of industry revolution

We have experienced four industrial revolutions driven by groundbreaking innovations. The first industrial revolution realized mechanization by using the power of water and steam to exceed the limitations of human and animal power. After this revolution, hand production is replaced by factory manufacturing. The second industrial revolution used electrical power to drive massive automated production. This has led to the rise of heavy industry, such as electric power plants, electrical manufacturing, cast iron, railroads, and chemicals. The third industrial revolution, known as the digital revolution, used electronic devices and information technology to eliminate human influence to improve the precision and automation of industrial manufacturing. The invention and application of atomic energy technology, electronics, computer technology, and bioengineering technology were appeared [49].

Industry 4.0 or the fourth industrial revolution is first introduced by the German government, aiming at improving the competitiveness of German industry and taking the lead in the new industrial revolution. Industry 4.0 refers to the use of the IoT and large-scale machine-to-machine communication to achieve full automation: improving communication, enable self-monitoring, and creating smart machines that can analyse and diagnose issues without the need for human intervention. Sensors will play a key role in the future Industry 4.0 systems that monitor the production process and control the product quality. Deploying a large scale sensor network can be difficult, especially with contact sensors. As a result, high precision non-contact sensing technology is the key for industry 4.0 [50-53].

1.6 Overview of non-contacting sensing technology

There are several traditional wireless sensing technologies widely used in the industry, such as laser, ultrasonic, and radar. These technologies use similar principles to make a range measurement. They all emit a signal that reflects from the target surface, and the sensor electronics calculate the range from the time of flight. Whereas different types of signals are used for each technology, each technology is suitable for different applications.

Laser is widely used in distance measurement applications. A laser ruler can be easily found in shops with a range accuracy of millimeters. Nowadays, in many advanced cell phones and depth cameras, the laser has been used as a lidar to detect distance. For autonomous driving, Lidar and radars are both used for sensing. Laser is the abbreviation for “light amplification by stimulated emission of radiation”. It is basically a very narrow beam of powerful light. The narrow beam can be easily blocked by a small object which means the laser cannot be used in a dusty environment. It also requires a certain surface of the target that enough reflected light

will come back to the sensor. Besides, the power of the light is concentrated in a small spot so that it is very powerful. It can be used for cutting in the industry. At the same time, it can be harmful to the human body depends on its power level and wavelength [54].

Ultrasonic is another technology that is widely used in distance sensing and imaging. It was widely used in military, medical, and industrial applications. In military applications, the ultrasonic is used for positioning. In medical applications, it is commonly used for medical imaging diagnosis, where ultrasonic can visualize soft tissues such as muscles and internal organs, including their size, structure and pathological lesions. Obstetric ultrasonography is widely used for prenatal diagnosis at the time of pregnancy. Compared with X-ray and computed tomography (CT), the ultrasonic diagnostic is non-radioactive, which means it is safe for the human body. Ultrasonic is a sound wave with frequencies from 30 kHz and 240 kHz, which is a mechanical wave. It requires a medium to travel through. In this case, any change of the medium will affect the traveling speed of the ultrasonic. If the measurement environment changes during the process, an error will occur. As a result, the ultrasonic sensors are more suitable for measurement stationary environment or with less accuracy requirement. The beam angle of the ultrasonic is normally wide, around 10 degrees. The widespread acoustic waves will interfere with other sensors. Ultrasonic sensors are usually used for relatively short-range detections. It can only detect objects around ten meters away [55-56].

Radar is the abbreviation for “radio detection and ranging”. The electromagnetic energy is emitted into space directionally. The direction and speed of the object can be calculated. The shape of the object can be detected. Radar was first developed for detecting the object in a non-visible condition before world war II. During the extreme weather condition, foggy days and nights, radar was used to assist cargo ships in avoiding the collision. Then, radar started to be widely used in the military area for detecting and tracking our and enemies’ tanks, airplanes, missiles and etc. During world war II, radar technology has been developed rapidly. Nowadays, radar has been given a wide range of uses, such as weather forecasting, human activity monitoring for rescuing, autonomous-driving assisting, and etc. In automatic manufacturing, radar plays an important part in precise monitor and control. For radar sensors, it transmits an electromagnetic wave, which implies the signal transmission doesn’t require a medium (unlike ultrasonic). As a piece of evidence, radar is often used for space-related applications [57]. At lower frequencies, with the help of high-power amplifiers, radar can detect objects thousands of kilometers away. However, their long wavelength often has limited ranging resolution, and the large-scale antennas are difficult to be deployed. With the frequency increasing, the wavelength of the signal decreases, the measurement accuracy increases accordingly. At the same time, the power of the signal decreases so that high-frequency radar sensors are suitable for short-range and small object detection. The short wavelength of millimeter-wave provides opportunities for achieving high precision radar sensing. The challenges of achieving high accuracies, long measurable distance and suitable for multi-user scenarios will be discussed. To address these challenges, two millimeter-wave radar systems are presented [D][E].

1.7 Thesis scope and outline

The thesis scope is addressed in Fig. 1.4 as a three-layer structure. The theme of the thesis on the top two layers is given in the first chapter. The first chapter introduces the basic knowledge about millimeter-wave. In addition, the opportunities brought by the millimeter-wave for communication and radar sensing systems are also discussed in Chapter I. In Chapter II, the difficulties in realizing wideband synchronization in millimeter-wave communication systems are first discussed. Then, two hardware efficient baseband receivers [A][B] with a carrier recovery subsystem are presented. Real-time transmissions through E-band are demonstrated. These works are modulation independent baseband receiver solutions that only require a low-speed ADC. In Chapter III, the necessity of having a high frequency, wide-band, multi-modulus frequency divider in frequency synthesizers is first discussed. Next, a summary of published frequency dividers is presented to show that the multi-modulus dividers are mostly with low frequency and narrow operational bandwidth. Then, a D-band dual-mode frequency divider [C] is introduced. The dual-mode division demonstrates the highest frequency among the dividers that divide both by-2 and by-3, and a state-of-the-art operational bandwidth among divide-by-3 (41.5%) dividers to the best author's knowledge. In Chapter IV, the millimeter-wave radar system is introduced. Different kinds of radars are compared and discussed with their advantages and shortages. Difficulties in having precision, long measurable distance, and capability of been used in a multi-user scenario are introduced. Two radar systems with different distance estimation methods are presented [D][E]. Their advantages and limitations are discussed. Finally, the conclusion and discussions are given in Chapter V.

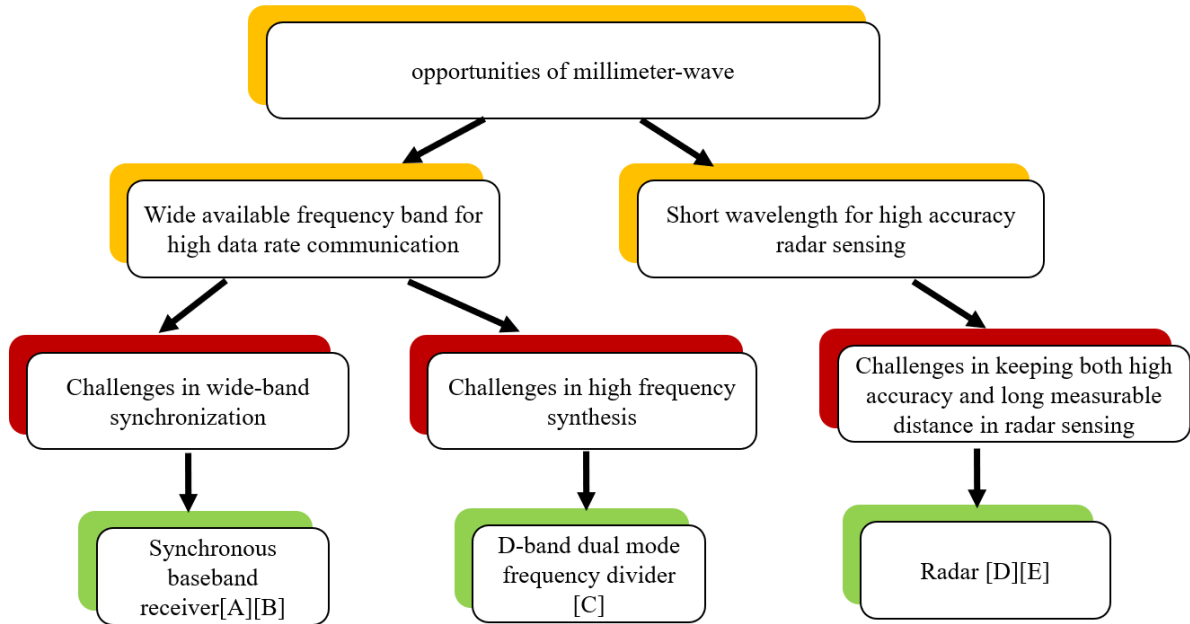
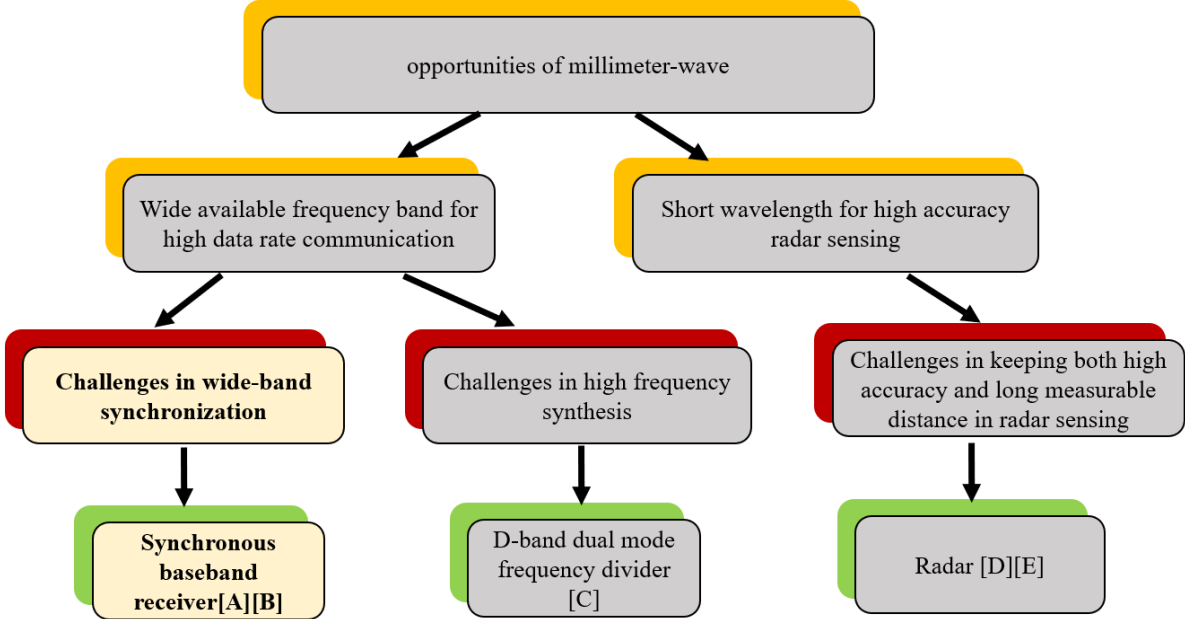


Fig. 1.4 The thesis outline in block diagrams.

Chapter 2

Millimeter-wave Wideband Synchronous Receivers



2.1 Overview of published millimeter-wave transmissions

Communications in millimeter-wave frequencies have been demonstrated in recent publications. It can be sorted into two groups: with or without real-time demodulation. With the help of advanced laboratory equipment and off-line DSP, the non-real-time transmission has been demonstrated at a very high data rate up to 100 Gbps [42]. These results indicate the millimeter-wave frequency frontend transceiver chipsets already have the capabilities to support high data rate transmissions.

Table 4.1 summarizes some published real-time transmission experiments over millimeter-wave bands. Real-time transmissions are demonstrated with either a high data rate of few bits per symbol or a low data rate of many bits per symbol. The maximum data rate in real-time millimeter-wave transmissions at the moment is 42 Gbps using a 2-ASK signal [33]. Among the published papers, the highest modulation order that has been successfully transmitted in real-time is 64-QAM, with a single-channel data rate of 5.3 Gbps [43].

For low modulation order signals, such as OOK, ASK, BPSK or QPSK, real-time demodulation can be realized by non-coherent detections. Such as OOK and ASK signals, by detecting the amplitude of the received signals, the transmitted data can be recovered. For BPSK and QPSK signals, as illustrated in Chapter 2, differential coding and detection could help in realizing real-time demodulation. For PSK signals, there are two well-known methods to implement demodulation, Costas loop [30] and multiplication [58]. However, the structure of the Costas loop becomes more complicated with the increased PSK modulation order. To recover the carrier frequency by multiplication, a frequency multiplier and divider are needed. For a QPSK signal, a frequency quadrupler and a four times frequency divider are needed. This makes the demodulator more complex. Therefore this solution is limited to low modulation order signals.

For high modulation order (more than 4) QAM signals, real-time coherent demodulation is accomplished with a recovered carrier signal. Carrier recovery is commonly implemented in digital signal processing (DSP) platforms on the received intermediated frequency (IF) signals. Limited by the ADC sampling speed, the highest single-channel data rate in real-time millimeter-wave communication with DSP platforms is below 10 Gbps [48]. Paper [A] and [B] demonstrate real-time millimeter-wave communication systems with two proposed synchronous baseband receivers. Two CR subsystems in the receiver are implemented in a digital and analog hybrid way. The received signal is down-converted to baseband instead of the IF stage for carrier recovery. Furthermore, the required ADC sampling speed in the proposed CR subsystems are only 100 MSps and 40 MSps, which are much lower than previously reported DSP platforms of CR solutions.

Table 2.1 Published real-time transmission experiments over millimeter-wave bands.

Ref	Data rate per channel (Gbps)	Modulation	ADC sampling rate (GSps)	Frequency band	Receiver topology
[44]	22.2	DQPSK		120 GHz	IF (DQPSK)
[47]	8	16-QAM	Without DAC	73.5 GHz	IF (analog PLL)
[33]	42	2-ASK		300 GHz	IF (direct detection)
[30]	2.5	QPSK		87 GHz	Baseband (Costas loop)
[59]	2.5	QPSK	3.52	60 GHz	IF (digital)
[60]	1.5	8-PSK	2	E-Band	IF (digital)
[61]	1.25	16-QAM	0.9375	E-Band	IF (digital)
[62]	1.58	16-QAM	3.456	60 GHz	IF (digital)
[31]	3	16-QAM	3	340 GHz	IF (digital)
[43]	5.3	64-QAM	Not mention	143 GHz	IF (digital)
[29]	5	16-QAM	1.25	E-Band	IF (digital)
[A]	9/16	64-QAM/ QPSK	0.1	E-Band	Baseband (hybrid)
[B]	18/24	64-QAM/ 16-QAM	0.04	E-Band	Baseband (hybrid)

2.2 Considerations of the pilot tone insertion

Besides the synchronization methods mentioned in the previous section, there is another traditional solution of achieving synchronization by using a pilot signal. The pilot signal carries the information that is pre-known by the receiver. By analysing the phase of the pilot signal, the carrier can be recovered. One widely used pilot is a single tone continuous wave (CW) signal, which can be inserted in the spectrum of the transmitted signal. As shown in Fig. 2.1, the pilot tone can be inserted at different frequency offsets from the transmitted carrier frequency. Three examples are discussed in this section: the pilot in the center of the carrier, the pilot outside the modulated signal, and the pilot embedded in the modulated signal.

In the first case shown in Fig. 2.1 (a), the pilot tone is inserted at the center of the transmitted signal. This is a common pilot insertion method since the carrier leakage exists naturally at the transceiver frontend modules. In the heterodyne receiver, the RF signal is down-converted to an IF frequency. The pilot signal contains the IF information. By extracting the pilot tone, the signal can be down-converted with no frequency offset. A digital feed-forward structure as Fig. 2.2 (a) or an analog feed-forward structure as Fig. 2.2 (b) can be used in this case. In paper [63], an analog feed-forward structure is proposed. It uses an injection locking voltage oscillator to extract the pilot tone. In a homodyne receiver, this pilot tone is down-converted close to DC. In this case, the frequency of the pilot signal is the offset frequency. However, most of the high-speed ADC requires AC-coupled input. The low-frequency pilot signal can possibly be filtered out.

The pilot tone can also be inserted outside the signal band, as Fig. 2.1 (b) shows. In this case, it can be easily extracted by a bandpass filter (BPF) and then be used for carrier recovery or phase noise mitigation. The drawback of this method is the spectrum efficiency degradation due to the extra needed bandwidth. The feedback structure is shown in Fig. 2.2 (c) can be used in this case. The feedback loop can be realized in both analog and digital ways.

As another alternative depicted in Fig. 2.1(c), the pilot tone is inserted in-band regarding the transmitted data. In this case, the spectrum efficiency remains the same as the case without the pilot. On the other hand, the power of the pilot tone needs to be adjusted carefully so that the pilot tone has little impact on the quality of the transmission signal since the pilot cannot be filtered out at the receiver side. The structure shown in Fig. 2.2 (c) could be applied in this case to realize carrier recovery. Furthermore, in a homodyne receiver, the pilot tone is closer to the DC compare with the second case, which allows a lower sampling rate for the ADC and DAC in the DSP platform.

Besides the single tone pilot, sequences are also widely used as pilot signals [64-66]. There are two traditional ways to insert the sequence. First, the sequence can be placed ahead of the data in the time domain, as Fig. 2.3 (a) shows. Second, the sequence can be placed in a separate frequency band beside the data so that it can be extracted at the receiver side by a BPF, as Fig. 2.3 (b) shows. With these two methods, the pilot signal either takes additional time or additional bandwidth. Alternatively, the pilot can also be inserted inside the baseband signal, as Fig. 2.3

(c) shows. In this case, the pilot and the data overlap each other. Therefore a special processing technique is needed to separate them.

Two pilot-assisted synchronous homodyne receivers are proposed in paper [A] and paper [B] and presented in this thesis. A single tone CW pilot [A] and a pseudorandom noise coded pilot (PNCP) signal [B] are used to assisting the carrier recovery, respectively. In both cases, pilots are superimposed within the baseband signal. The single tone CW pilot is inserted, as Fig. 2.1 (c) shows, and the PNCP is inserted as Fig. 2.3 (c) shows.

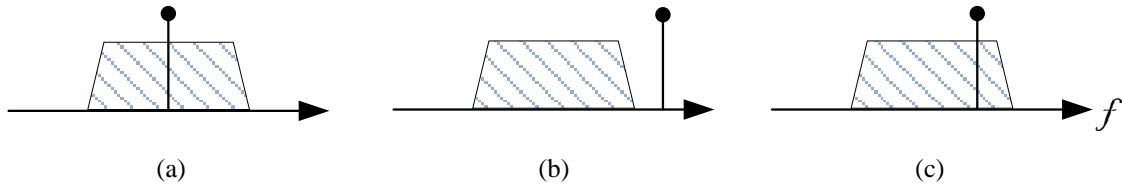


Fig.2.1. Choices of a pilot tone insertion: (a) at carrier frequency; (b) out-of-band; (c) in-band.

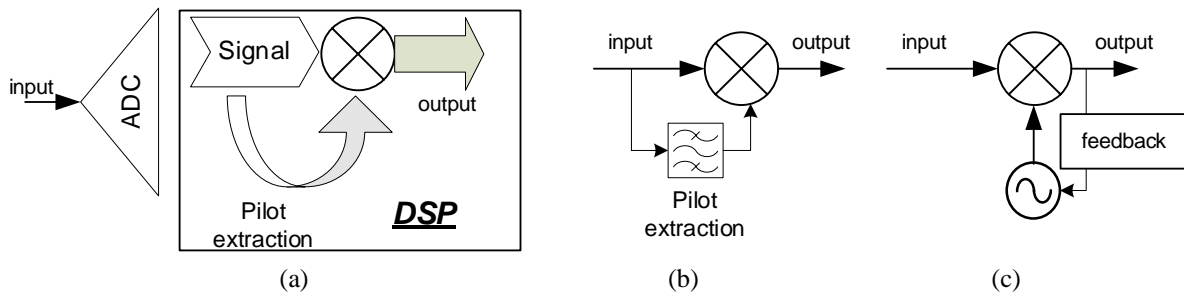


Fig.2.2. Pilot extraction methods: (a) full digital feed-forward; (a) analog feed-forward; (a) analog feedback.

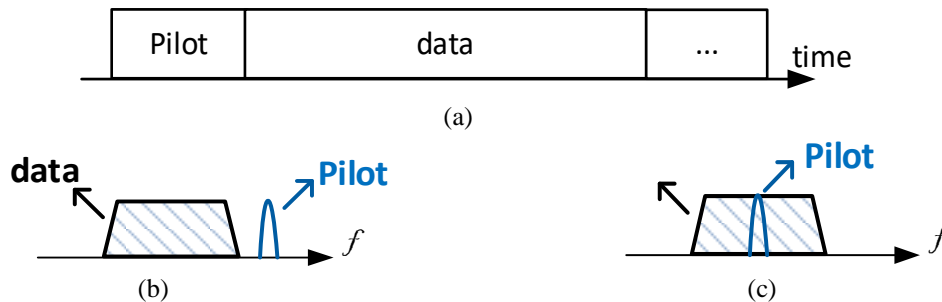


Fig. 2.3 Choices of a sequence pilot insertion: (a) ahead of the data in the time domain; (b) out-of-band; (c) in-band.

2.3 The proposed millimeter-wave communication system

The system structures proposed in paper [A] and [B] are similar. The difference is their pilot extraction parts at receivers. An E-band communication system structure is proposed and shown in Fig. 2.4. At the transmitter side, a pilot is superimposed within the signal band. It should be noted, different types of pilots are used in these works, respectively. In paper [A], the pilot is a CW signal, as the yellow line shows. In paper [B], a PNCP is used, as the red curve indicated. The pilot is upconverted to E-band together with the modulated signal using an E-band TX module. At the receiver side, the received signal is down-converted to the baseband by an E-band RX module. There is a frequency offset that remained with the baseband signal due to the frequency difference of two separate LOs in the transmitter and the receiver. A CR subsystem

is proposed to remove the frequency offset. This CR subsystem includes a DSP platform and analog components. In the DSP platform, the pilot is extracted from the baseband signal and helps to identify the frequency offset. Then the LO frequency is adjusted accordingly by analog components to remove the frequency offset.

At the receiver side, the pilots are extracted by a DSP platform with low-speed ADCs and DACs. For the CW pilot, analog and digital BPFs are used to extract it. For the PNCP, its spectrum is spread at the transmitter side first, and a digital matched filter is used to extract it. The power of the pilot needs to be chosen carefully since it is an interference to the high-speed baseband signal. Meanwhile, the power must be large enough so that the pilot can be detected at the receiver side.

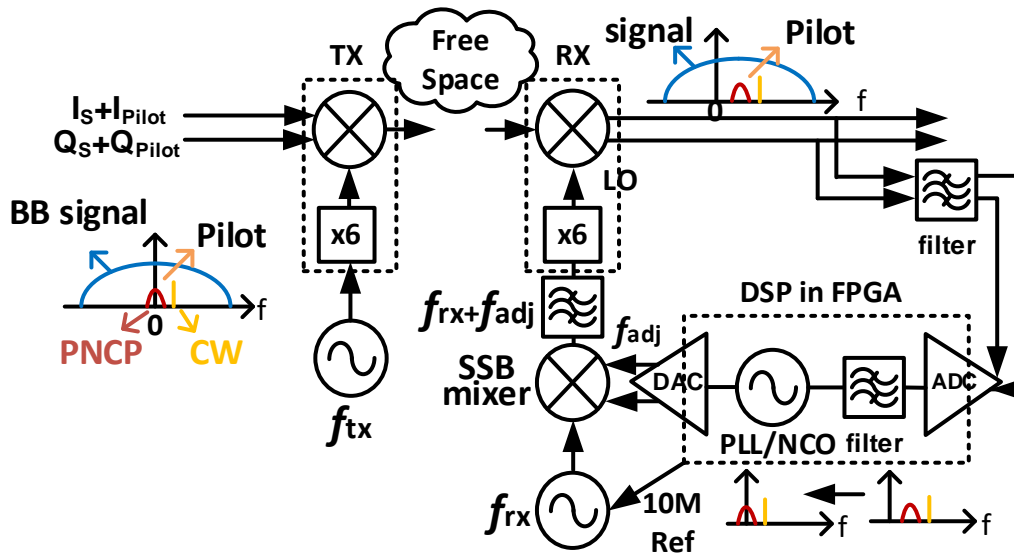


Fig. 2.4 Proposed E-band link structure [A][B].

2.4 Direct sequence spread spectrum

Direct sequence spread spectrum (DSSS) is a frequency spreading modulation technique for data transmission. The idea is to spread a signal using a specified bit sequence. Each symbol in the original low-speed signal is replaced by a high-speed bit sequence code to create the spread spectrum signal. In this case, the spectrum of the signal becomes wider as the high-speed sequence so that it is spread. The spectrums before and after the spreading are shown in Fig. 2.5. The spread-spectrum signal occupies larger bandwidth so that its power spectral density becomes lower. The technique is used to make the signal more robust against interference with the help of correlation at the receiver. The high-speed bit sequence is often referred to as a “chip” or “spreading code”. At the receiver side, the spread spectrum signal passes through a matched filter to correlate with the same chip for demodulation. The correlation will make the power concentrated again to a narrow bandwidth. The spread spectrum signal is turned into a low-speed impulses signal which contains the original low-speed signal information. By analyzing the phase of the impulses signal, the original data is recovered [67]. The time-domain signals in a spread spectrum system at the transmitter and the receiver sides are shown in Fig. 2.6. The symbol rate ratio between the chip and the original signal is defined as the spread spectrum

ratio. With a higher spread spectrum ratio, a higher processing gain is obtained after the correlation.

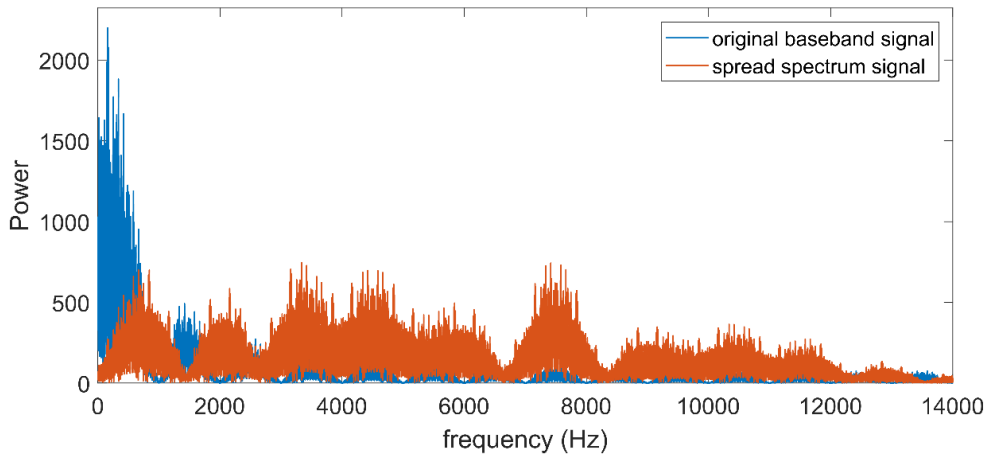


Fig. 2.5 The spectrum of the original signal and the spread spectrum signal [B].

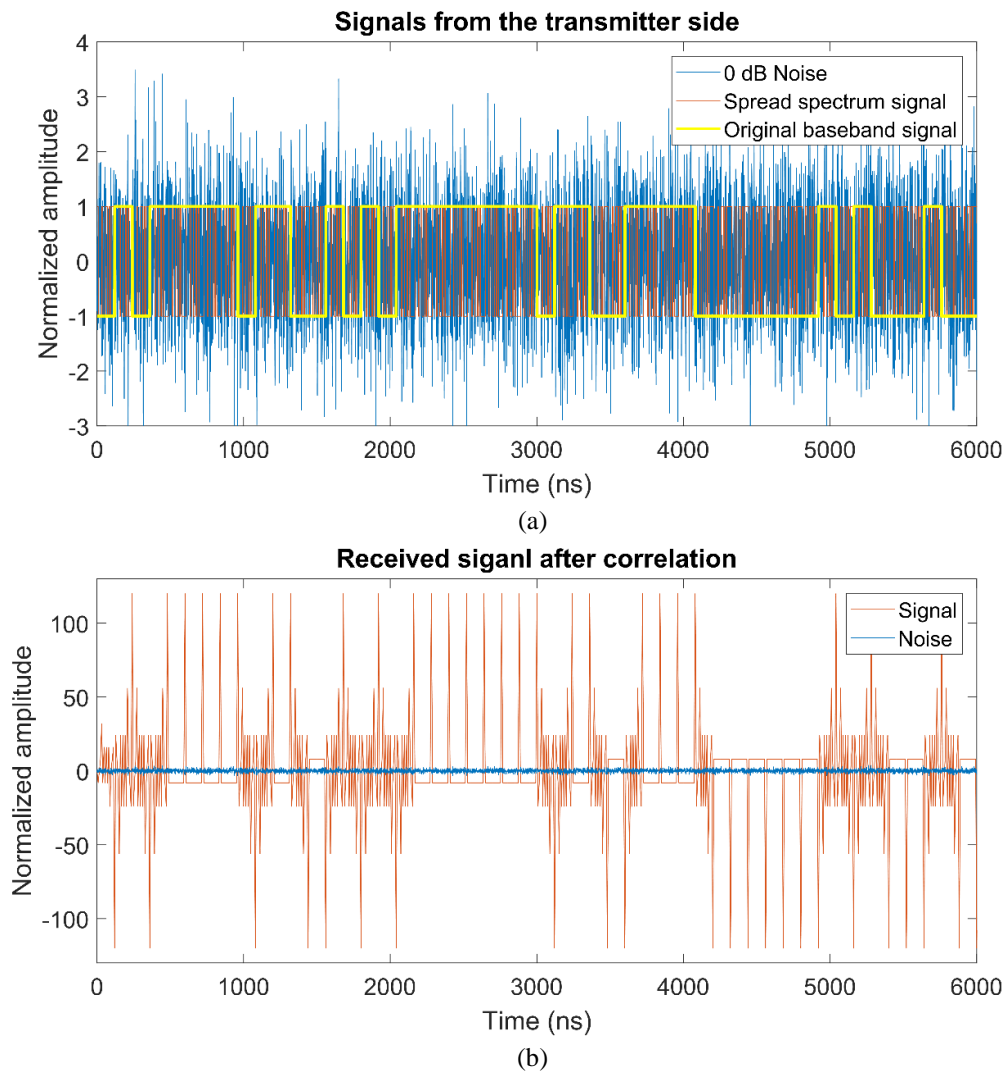


Fig. 2.6 Signals in a spread spectrum system (a) from the transmitter side; (b) from the receiver side [B].

The spread spectrum signal $x(n)$ consists of two symbols, -1 and 1. Assume the spreading code has a length of L . When $x(n)$ correlates with itself, the output is

$$\sum_{n=1}^L x(n) \times x(n - m) = \begin{cases} L, & m = 0 \\ \ll L, & m \neq 0 \end{cases} \quad (2.1)$$

When another signal $y(n)$ correlates with $x(n)$, and $x(n)$ and $y(n)$ are independent, the output is

$$\sum_{n=1}^L x(n) \times y(n - m) = P \ll L, \quad (2.2)$$

where $y(n)$'s power is normalized. P is much smaller than L . The power of $y(n)$ is not accumulated after the correlation. On the contrary, the power of $x(n)$ is accumulated after the correlation, thus obtain a high correlation peak.

For the example shown in fig. 2.6, the power ratio between the spread spectrum signal and the noise is 0 dB. The spread spectrum ratio is 15, and the oversampling ratio is 8. After the received signal passes through the matched filter, it becomes a series of impulses, as the orange curve shows. In this case, the transmitted data can be recovered with a low signal-to-noise ratio (SNR) or with strong interferences if the spread spectrum ratio is large enough.

2.5 Advantages of using PNCP

As mentioned in the previous section, the spread spectrum signal does not need a high SNR to be transmitted. The proposed PNCP uses a pseudorandom noise (PN) sequence as the spreading code to modulate the pilot data [B]. As a result, its transmission power can be lower so that it does not interfere too much with the baseband signal. By using a PNCP signal in the system, there are two fundamental advantages. First, it can carry an additional arbitrary message. Second, it enables the code-division multiple access (CDMA) by assign each transmitter a unique spreading code. In this case, the messages from different transmitters can be tracked and analyzed separately.

Fig. 2.7 (a) shows a simplified millimeter-wave point-to-point communication link with a PN pilot inserted in the baseband signal, as Fig. 2.4 shows. Besides assisting synchronization, the pilot can also carry channel information such as symbol rate, modulation format, etc. In this case, adaptive modulation can be used in the system to adapt to changes in the communication channel. As an alternative to using an additional time slot or spectrum to transmit the channel information, PNCP consumes transmission power.

In a line of sight multiple input multiple output (MIMO) system, multiple radios operate simultaneously at the same frequency band so that they suffer from the interference come from adjacent radios. A simplified MIMO system is shown in Fig. 2.7 (b). To avoid interference, spatial orthogonality is required. The received signals from the desired transmitter radio and the adjacent channel need to be 90-degree out of phase. The precise deployment of the antennas is a challenge. Equalization is normally needed to remove the non-orthogonal interference introduced by non-ideal antenna installation [68]. However, when the spatial orthogonality is

non-ideal, the capacity is reduced and cannot be regained by digital processing. With PNCP, the channel information from each transmitter can be estimated. Then, using a phase shifter between transmitter and antennas, the phase mismatch from deployment inaccuracy can be adjusted post-installation with high precision in the field to optimize system performance.

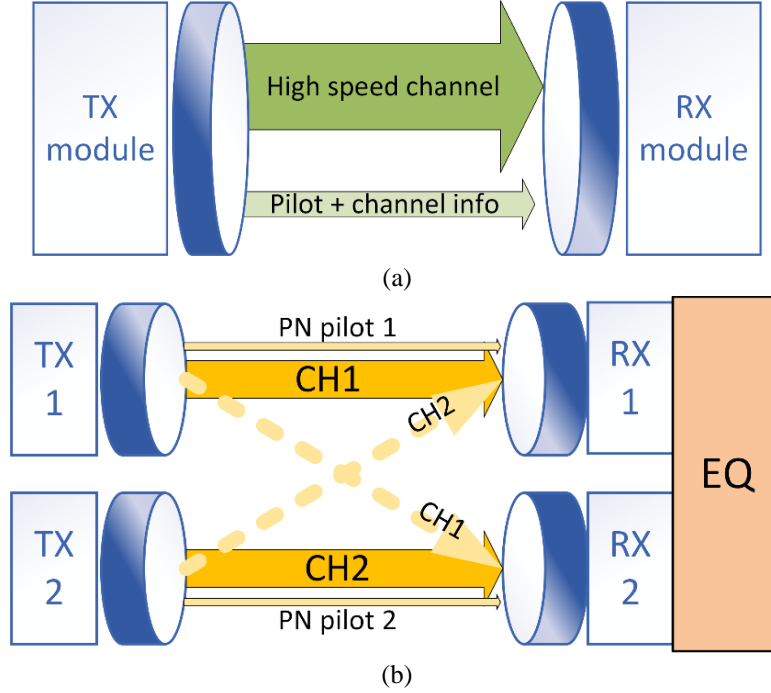


Fig.2.7. Pilot extraction methods: (a) full digital feed-forward; (a) analog feed forward; (a) analog feedback [B].

2.6 Two carrier recovery subsystems

Two carrier recovery subsystems are proposed in paper [A] and paper [B]. Two different pilots, a CW pilot and a PNCP, are used.

2.6.1 Carrier recovery subsystem with the CW pilot

In paper [A], the frequency of the CW pilot tone f_{pilot} is chosen to have a fixed relationship with the transmitter LO frequency as $f_{pilot} = f_{tx}/N$. As shown in Fig. 2.4, there is a six times frequency multiplier in the E-band module. The carrier frequency in the transmitter and the receiver are denoted $6 \times f_{tx}$ and $6 \times f_{rx}$, respectively. After the received signal is down-converted to the baseband, the received pilot signal is $f_{pilot} + 6 \times (f_{tx} - f_{rx}) = f_{pilot} + \Delta f$. This signal is sampled and send into the DSP platform, which shares a reference clock with the receiver LO. In this DSP platform, the received pilot signal $f_{pilot} + \Delta f$ is multiplied with the $1/N$ times of receiver LO frequency f_{rx} to find out the frequency offset. Then the PLL in the DSP platform generates an adjustment signal accordingly. The adjustment signal is converted to an analog signal and mixed with the original LO signal by a single side band (SSB) mixer. This mixed signal $f_{rx} + f_{adj}$ becomes the new LO. When $f_{adj} = f_{rx} - f_{tx}$, the CR loop will converge, and the received pilot signal becomes $f_{pilot} = (f_{rx} + f_{adj})/N$.

The detailed block diagram of the carrier recovery implementation is shown in Fig. 2.8 [A]. The pilot tone frequency is set at 21 MHz. The received signal passes through a surface acoustic

wave (SAW) BPF to extract the pilot signal. Then the received pilot signal is digitalized by a 100 MSps ADC and sent into an field programmable gate array (FPGA) running at 200 MHz which is fully synchronized with the receiver LO. A 30-tap digital BPF is used to further improve the pilot signal's quality. There are two numerical controlled oscillators (NCOs) in the FPGA. NCO1 is used to provide a digital copy of f_{rx} . NCO2 is a tuneable oscillator that provides the adjustment signal f_{adj} . By summing up the outputs of two NCOs, a replica of the SSB mixer output $f_{rx} + f_{adj}$ is created. It is divided by N in order to extract the frequency difference with the received pilot signal utilizing a phase detector. The phase detector consists of a digital mixer and a loop filter. If the received pilot tone is outside the BPF, the NCO2 will sweep the frequency until the pilot tone is captured.

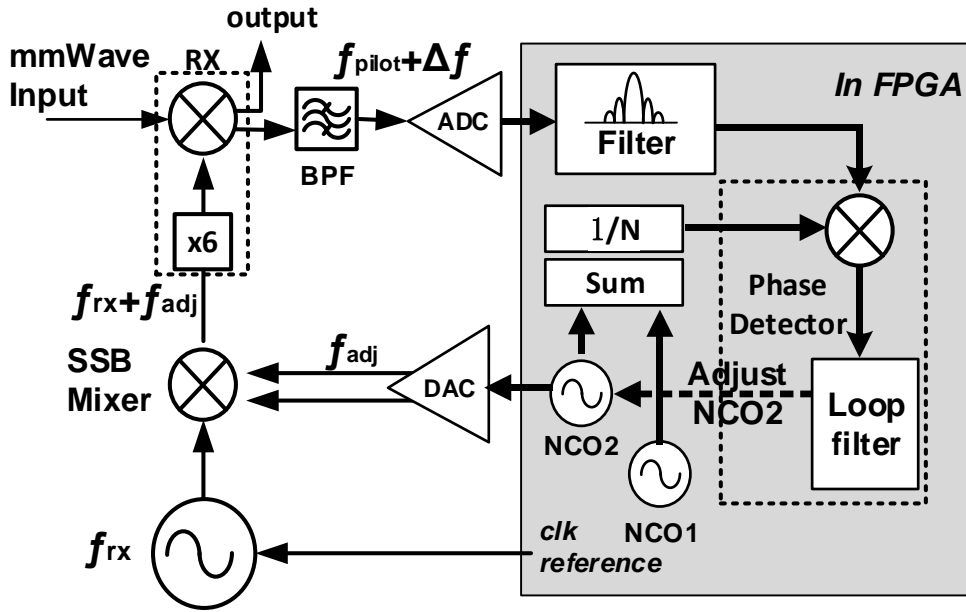


Fig. 2.8 A block diagram of the synchronous baseband receiver with CW pilot [A].

2.6.2 Carrier recovery subsystem with the PNCP

In paper [B], a PNCP is superimposed within the baseband signal with a low symbol rate of 5 Mbaud. A PN sequence with a length of L is used as the spreading code. The PNCP's spectrum is spread by using DSSS modulation technique to lower its transmission power. As Fig. 2.4 shows, the PNCP is sent together with the baseband signal. The frequency offsets within the PNCP and the baseband signal are the same. By applying the CR to the low-speed PNCP signal, the high-speed data signal is also synchronized. The PNCP is only 5 Mbaud in this work [B], which allows the low-speed ADC, DAC and DSP platform to be used in the system.

The block diagram of the proposed CR subsystem is shown in Fig. 2.9. A 5 MHz bandwidth low pass filter (LPF) is placed after the down-conversion mixer to extract the PNCP. Then the PNCP is sampled by a 40-MSps ADC and goes into an FPGA for digital processing. Inside the FPGA, the pilot samples pass a matched correlation filter to further improve the SNR, as Fig. 2.6 shows. The phase of the pilot signal can be calculated accordingly. Increasing the length of the PN sequence can further increase the SNR, however, at the expense of increased computation complexity and latency. With a higher spread spectrum ratio, the matched filter

must have more taps, which introduces an additional delay to the CR feedback loop. In this case, the bandwidth of this feedback loop is limited by the number of taps of the matched filter.

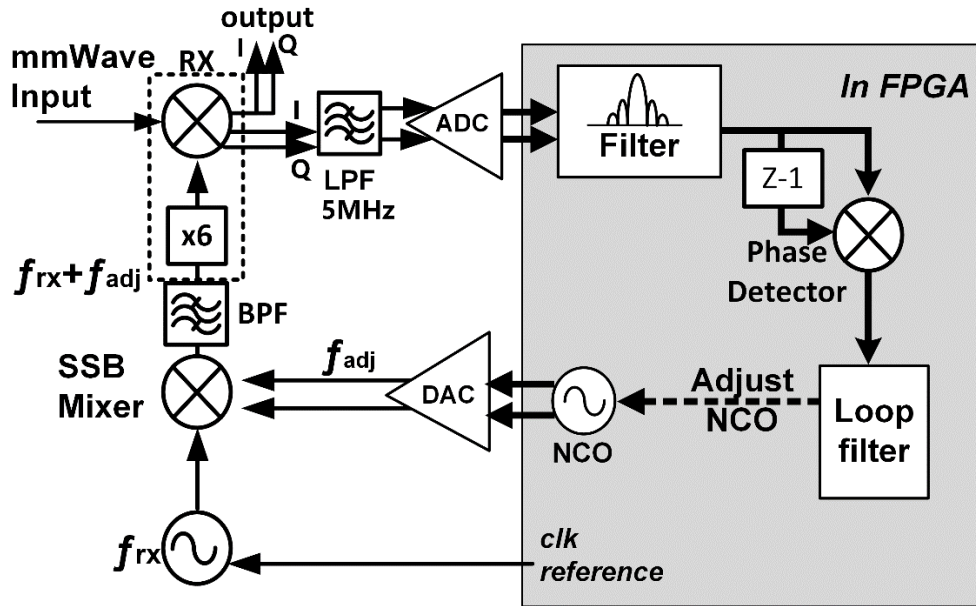


Fig. 2.9 A Block diagram of the synchronous baseband receiver with PNCP [B].

A delay unit (Z^{-1}) and a phase detector are used to calculate the change in phase. The output from them controls the loop filter, which decides how many phases and frequency adjustments should be made. Then the NCO is tuned accordingly to provide the quadrature adjusting signal with a frequency of f_{adj} . This adjusting signal mixes with the LO signal f_{rx} by an SSB mixer. A BPF is placed after the mixer to further suppress the unwanted spurs and sideband tones. The mixed-signal $f_{rx} + f_{adj}$ goes into the receiver as a new LO signal. The feedback loop converges when $f_{rx} + f_{adj} = f_{tx}$, the phase detector outputs 0.

The bandwidth of the processed signal is only 5 MHz in this work. It is even lower than the previous work [A]. Compare with the full digital CR solution where the processed signal has several GHz bandwidths, the hardware implementation complexity of the proposed two CR subsystem is much lower.

2.7 System limitations

The limitation of the proposed communication system comes from three aspects. One of the limitations is introduced by the commercial E-band transmitter and receiver modules in use. The highest data rate and the highest modulation order that a pair of transceiver modules can transmit is limited by their output power, linearity, etc. A pair of commercial E-band modules from Gotmic AB is used in both works [A][B].

The second limitation of this system is the sideband suppression of the adjusted receiver carrier signal $f_{rx} + f_{adj}$. The LO frequencies, f_{tx} and f_{rx} , are chosen to be 40 MHz different from each other at the beginning, so that an RF frequency difference is 240 MHz (transceiver with a built-in sextupler). In this case, f_{adj} is centered at 40MHz. After mixing f_{adj} and f_{rx} by the

SSB mixer, the image signal $f_{rx} - f_{adj}$ is also introduced to the system as an unwanted sideband. The upper and the lower sideband are 80 MHz apart from each other. More sideband suppression gives a cleaner carrier tone. A BPF is placed at the output of the SSB mixer to further increase the sideband suppression in both work [A] and [B].

The third limitation of this system is the interference introduced by the pilot tone. The pilot tone introduces deviation and magnitude error to the constellation. The high-order modulation signals are more sensitive to the increase of the pilot tone's power. A power ratio γ is defined as the ratio between the pilot signal power and the baseband signal power. Fig. 2.10 shows the simulation result of how a PNCP power affects the error vector magnitude (EVM) of a QPSK signal with a different SNR. When there is no noise in the system, at a power ratio of -40 dB, the pilot insertion degraded the EVM by 1%. When there is noise in the system, noise and the pilot both affect the EVM. When the pilot power is very small, the noise becomes the dominant factor that limits the system performance. At this point, the pilot power does not need to reduce further.

In work [B], the DSSS modulation is used for the PNCP. With a larger spread spectrum ratio, the pilot power can be decreased at the transmitter side. Fig. 2.11 shows the relationship between the EVM and the spread spectrum ratio with a different pilot to signal power ratio and SNR. Similarly, when the noise becomes the dominant factor that limits the system performance, the spread spectrum ratio does not need to increase further.

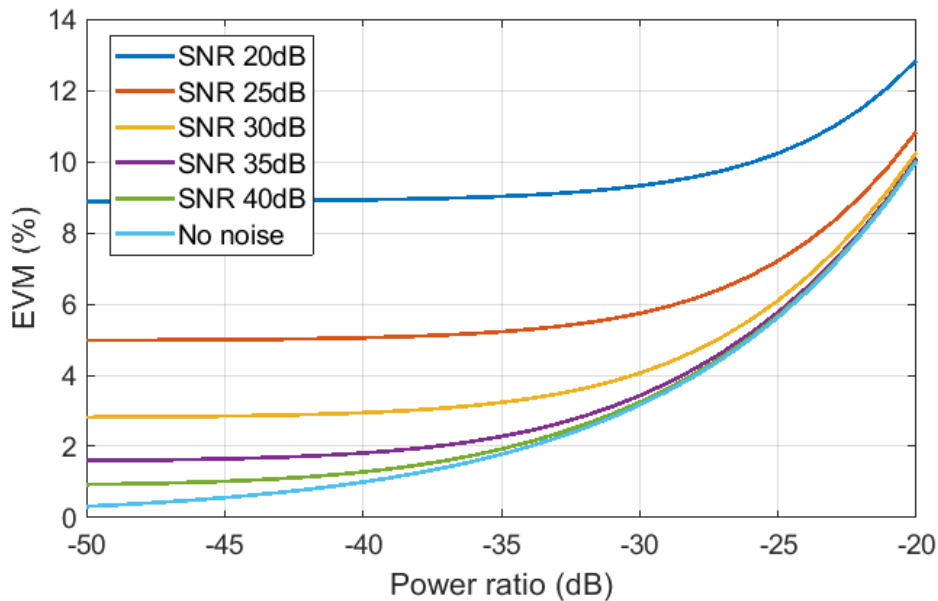


Fig. 2.10 EVM versus pilot to signal power ratio γ for different SNR at the transmitter side [B].

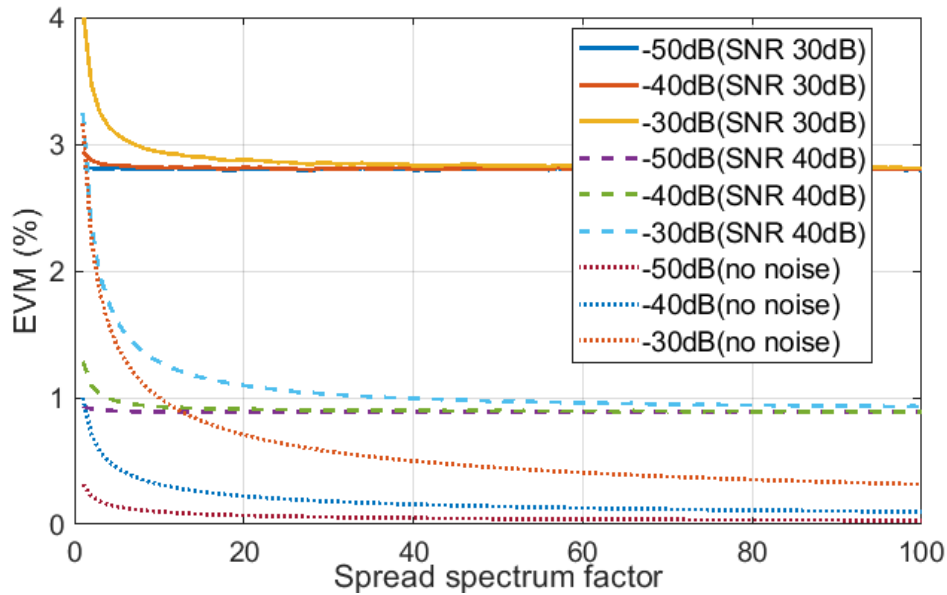


Fig. 2.11 EVM versus spread spectrum factor with a different pilot to signal power ratio and different SNR on the transmitter side [B].

2.8 Performance verification and discussion

A measurement setup shown in Fig. 2.12 is used to test the performance of the proposed millimeter-wave communication system [A][B]. The baseband signal and the pilot are generated by an arbitrary wave generator (AWG). Two commercial E-band frontend modules from Gotmic AB are used. Two signal synthesizers are used to provide LO signals. Waveguides and an attenuator connect the transmitter and the receiver modules. An oscilloscope is used to observe the constellation diagrams and estimate the EVM and the BER of the recovered signal.

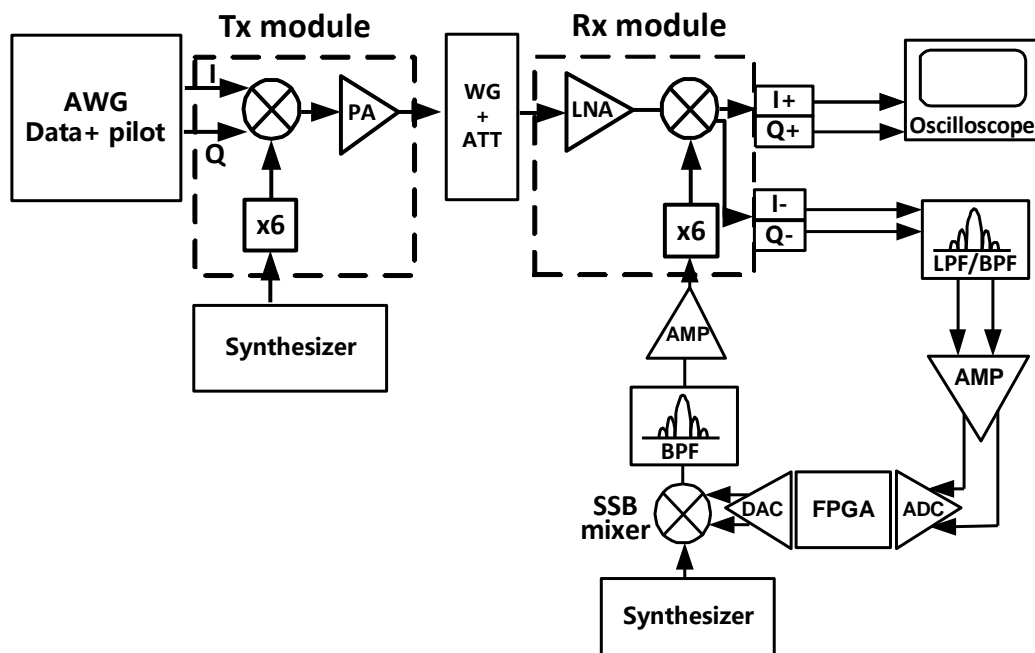


Fig. 2.12 Measurement setup [B].

In work [A], the CW pilot signal frequency is set at 21 MHz. Two LO frequencies are 13.83 GHz and 13.79 GHz. A 40 MHz LO frequency offset is introduced in advance to separate the adjusted signal and its image. The pilot signal frequency and the LO frequency are decided by available BPFs. A surface acoustic wave filter centered at 21 MHz with a 500-kHz passband and a nine-pole cavity filter centered at 13.83 GHz with a 10-MHz passband are used in the system. Besides, a 30-tap digital BPF is designed to further improve the SNR of the received pilot tone. The sampling rate of the ADC and the DAC in use are 100 MSps and 170 MSps, respectively. The proposed system has successfully transmitted QPSK, 16-QAM, 32-QAM, and 64-QAM signals with 43 MHz LO frequency offset. The carrier frequency offset is 258 MHz. The highest achieved data rate is 16 Gbps with a QPSK signal. The offset frequency is swept from 150 MHz to 330 MHz to test the system performance. Fig. 2.13 shows the EVM and BER versus offset frequencies of an 8-Gbps 16-QAM signal. The EVM and BER increase as the offset frequency deviates from 240 MHz. This is due to the decrease of the sideband suppression of the receiver carrier signal for the adjusted LO signal is moving away from the center of the BPF. The pilot-to-signal power ratio γ is tested from -60 dB to -20 dB. The minimum power ratio that keeps the CR subsystem functional is -40 dB. Fig. 2.14 shows the EVM versus power ratio γ . With a high power ratio γ , a high EVM is obtained due to the unwanted interference introduced by the pilot signal.

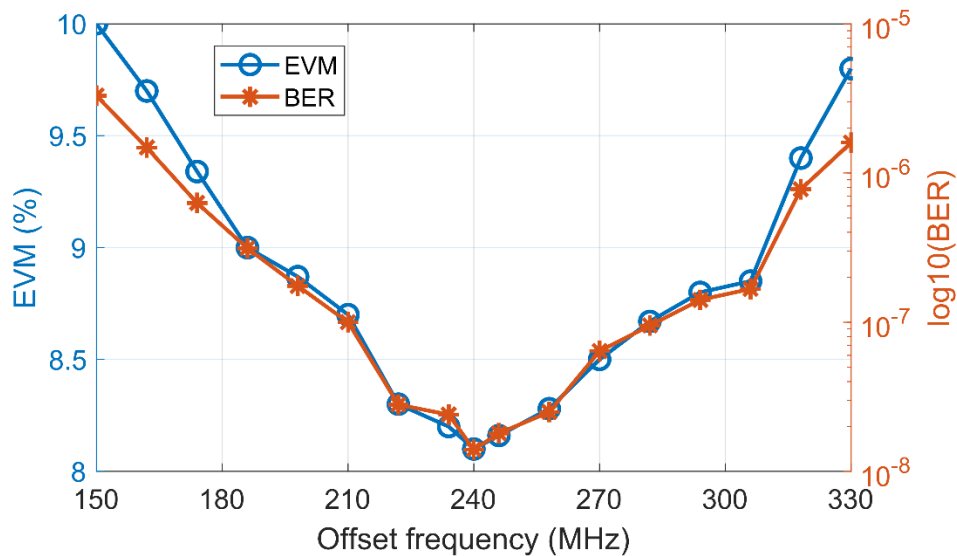


Fig. 2.13 EVM/BER versus offset frequencies of 8-Gbps 16-QAM signal [A].

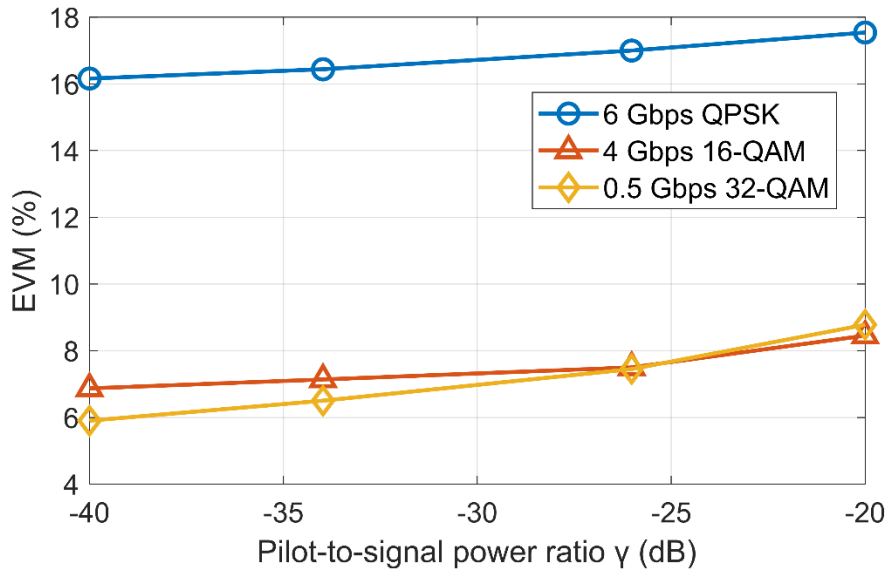


Fig. 2.14 EVM versus pilot-to-signal power ratio γ [A].

In paper [B], the PNCP is 5 Mbps and the spread spectrum ratio is 15. Two LO frequencies are 13.08 GHz and 13.04 GHz for which makes the transceiver modules a better performance. Similarly, a 5 MHz LPF and a BPF centered at 13.08 GHz are used in the system. The sampling rate of the ADC and the DAC in use are 40 MSps and 120 MSps. The same E-band transceiver modules are used in both works, and similar system performance is obtained. The highest modulation order tested is a 64-QAM signal. By using a different LO frequency in this work, a higher data rate is achieved. 24 Gbps 16-QAM has successfully been transmitted through the proposed system. Fig. 2.15 shows the EVM of the received 8 Gbps 16-QAM signal with offset frequencies from 210 MHz to 270 MHz. Fig. 2.16 shows the EVM versus power ratio γ . Under the current setup, the minimum power ratio that keeps the CR subsystem functional is also -40 dB. However, unlike the previous work [A], the power ratio in this work can be further reduced by increasing the spread spectrum ratio at the expense of narrower loop bandwidth of the CR subsystem. In this demonstration, the matched filter has 120 taps. Fig. 2.17 shows the EVM versus symbol rates with different modulation schemes in three different cases: back-to-back measurement when the transmitter and receiver are synchronized, back-to-back measurement when the transmitter and receiver are synchronized with a -40 dB PNCP as an interference, and the system measurement with the proposed CR subsystem. This figure indicates that the PNCP doesn't increase the EVM too much. The performance gap between the back-to-back system measurement and the proposed system measurement mainly comes from the insufficient sideband suppression of the adjusted LO signal.

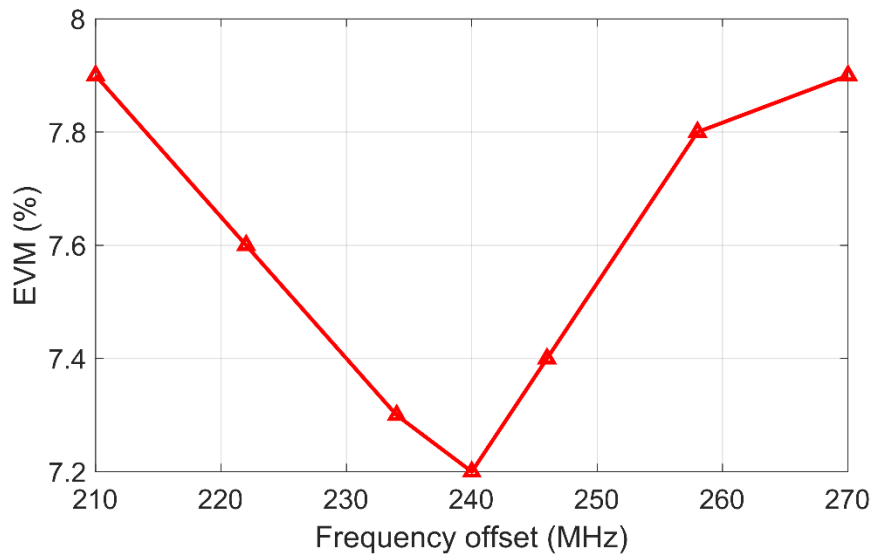


Fig. 2.15 EVM versus offset frequencies of 8-Gbps 16-QAM signal [B].

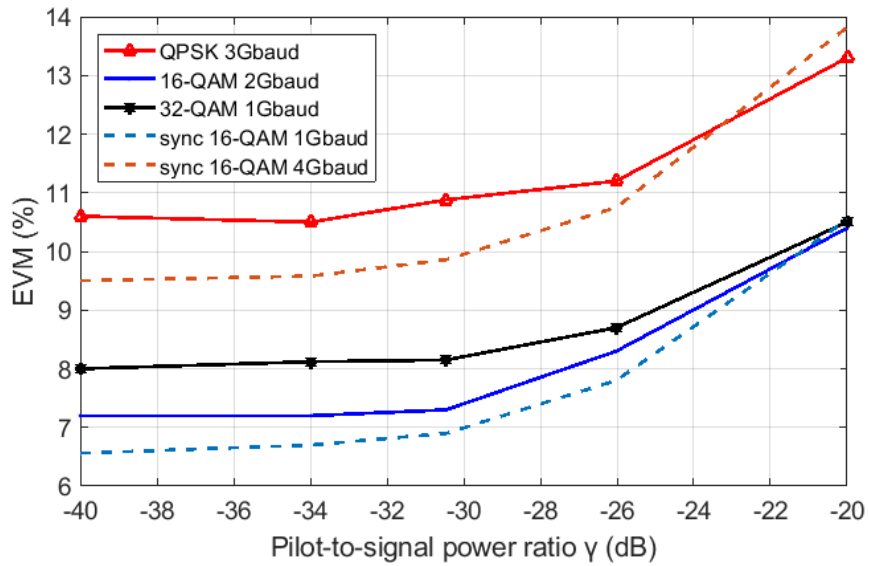


Fig. 2.16 EVM versus pilot-to-signal power ratio γ [B].

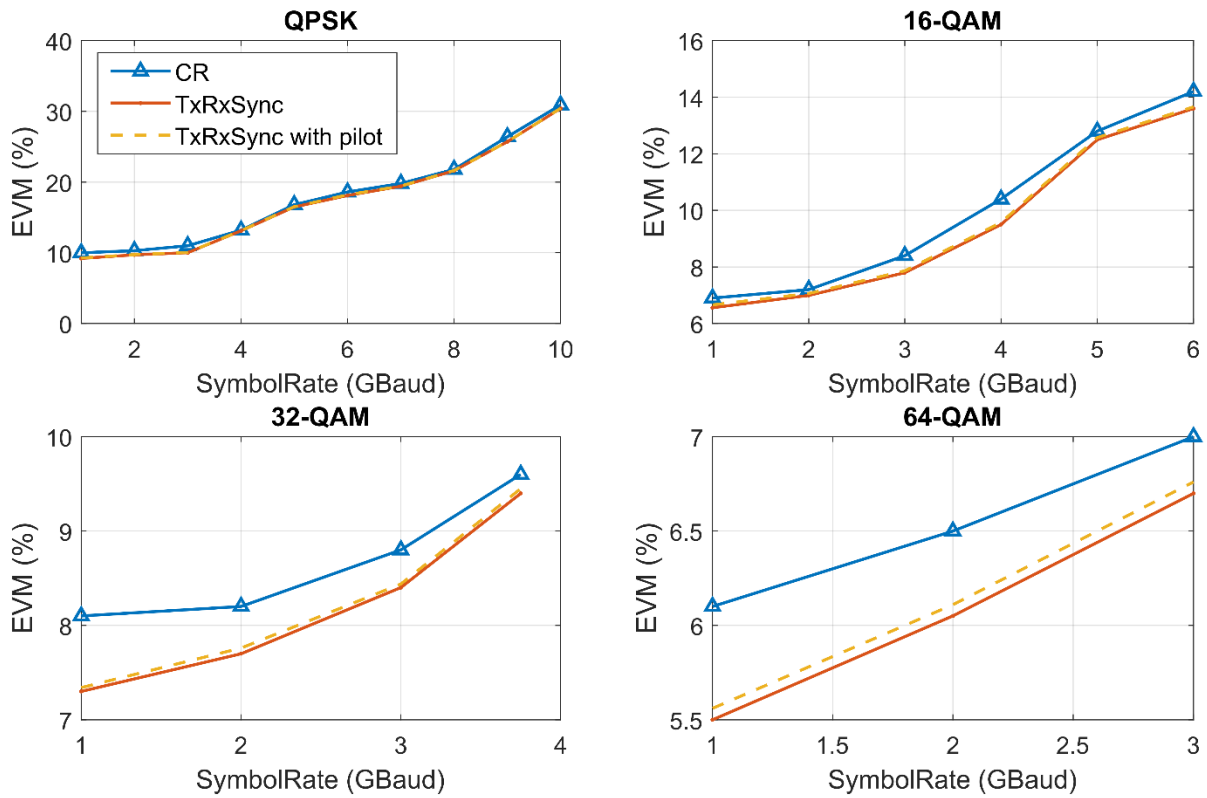
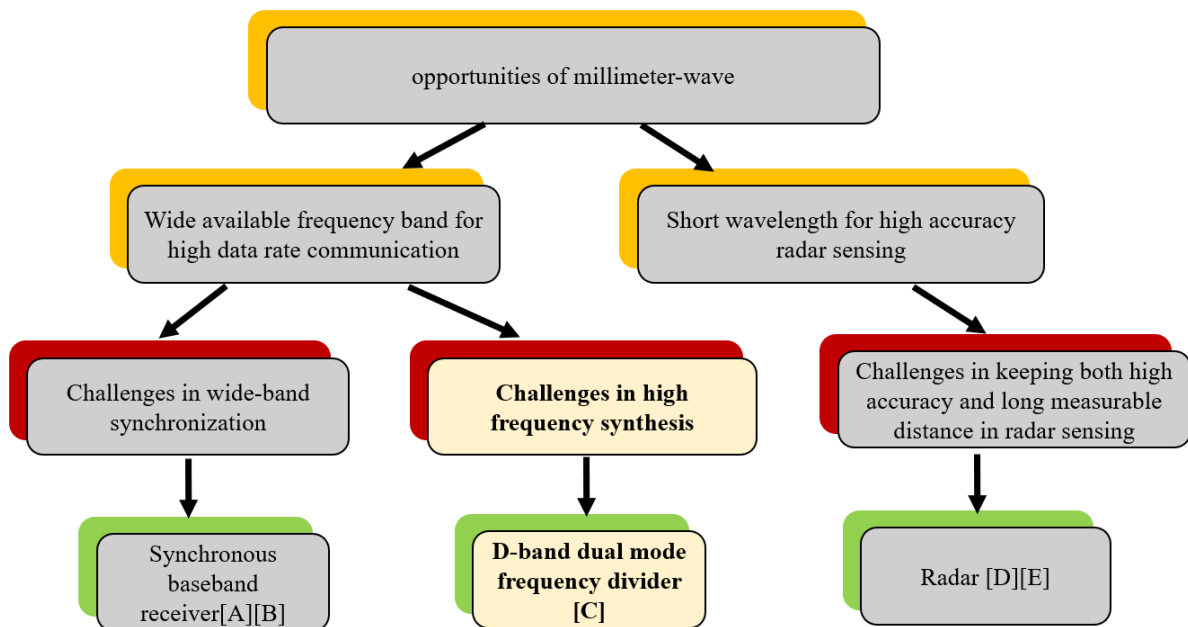


Fig. 2.17 EVM versus symbol rate with different modulation schemes [B].

Two proposed baseband receivers both use analog-digital hybrid way to realize carrier recovery with low-cost ADCs, DACs, and DPS platforms. Two proposed CR solutions are both modulation scheme independent and have no data rate restriction. Compared with recent publications on millimeter-wave transmissions with synchronization in Table 2.1, paper [B] is presently the modulation independent baseband receiver that has demonstrated the highest data rate transmission while requiring the lowest ADC sampling rate of 40 MSps. In the first CR solution with a CW pilot, a fixed ratio N between the LO and the pilot tone is defined. In the system demonstration, N is 659. The division of N in the FPGA requires a lot of resources since the offset frequency is usually quite small. The second CR solution with the PNCP has a simpler structure and requires fewer resources.

Chapter 3

Millimeter-wave Frequency Divider



3.1 Millimeter-wave frequency synthesizer

As discussed in Chapter I, generating a pure, low phase-noise, and stable millimeter-wave signal is a challenge. VCOs in Millimeter-wave have been published with a wide tuning range for several tens GHz [17-20], as Table 3.1 shows. For the millimeter-wave synthesizers, the close-loop topology, PLL, is used to stabilize the signal and lower the phase noise. In Table 3.2, recent published millimeter-wave synthesizers based on PLL are summarized and compared.

Table 3.1 Published millimeter-wave VCOs.

Ref	Centre frequency (GHz)	Tuning range (GHz)	Relative tuning range (%)	Topology	Technology
[17]	75	19.475	26	Push-Push Colpitts	130 nm SiGe BiCMOS
[18]	168	40	23.8%	Push-Push Colpitts	130 nm SiGe BiCMOS
[19]	136	19	14	Push-Push Colpitts	130 nm SiGe BiCMOS
[20]	135	30	22.2	Push-Push Colpitts	130 nm SiGe HBT

Table 3.2 Published millimeter-wave synthesizers based on PLL.

Ref	VCO tuning range (GHz)	Ref. clock center frequency (GHz)	Total divide ratio	Dividers in use (in sequence)	Technology
[69]	280-303	0.096	1024	$\div 4, \div 8, \div 8$	90nm SiGe BiCMOS
[70]	92.5-102.5	1.5	64	six $\div 2$ dividers	130 nm SiGe BiCMOS
[71]	25.4-29.7	0.05	512	$\div 2, \div 4, \div 64$	90 nm CMOS
[72]	105-117	0.45	256	$\div 2, \div 2, \div 64$	130 nm SiGe BiCMOS
[73]	48.4-54.25	0.2	256	$\div 2, \div 8, \div 16$	65 nm CMOS

The frequency divider is used to translate the high-frequency signal generated from a VCO to the reference clock frequency. The reference clock frequency is normally provided by a crystal oscillator that operates at a much lower frequency than the VCO. As Table 3.2 shows, a divider chain is often required to obtain a large divide ratio. The divider chain comprises several frequency dividers connected in series. Furthermore, the frequency divider chain is desired to have a reconfigurable divide ratio for matching a large range of VCO frequencies to a fixed reference frequency [21]. A large divide ratio is used for high oscillation frequencies, whereas a small divide ratio is used for lower oscillation frequencies. An example is shown in Fig. 3.1. If a VCO has a tuning range of 90 GHz, from 60 GHz to 150 GHz, a divide-by-3 divider translates the tuning range to 20 GHz to 50 GHz, as Fig. 3.1 (a) shows. By using a dual-mode divider with a selective divide ratio of 2 and 3, the input frequency from 100 GHz to 150 GHz

can be translated to 33.3 GHz to 50 GHz with a divide-by-3 divider, the input frequency from 60 GHz to 100 GHz can be translated to 30 GHz to 50 GHz with divide-by-2 divider as Fig. 3.1 (b) shows. The total output tuning range is 20 GHz, from 30 GHz to 50 GHz. It is 10 GHz smaller compare to the case using a single divide-by-3 divider.

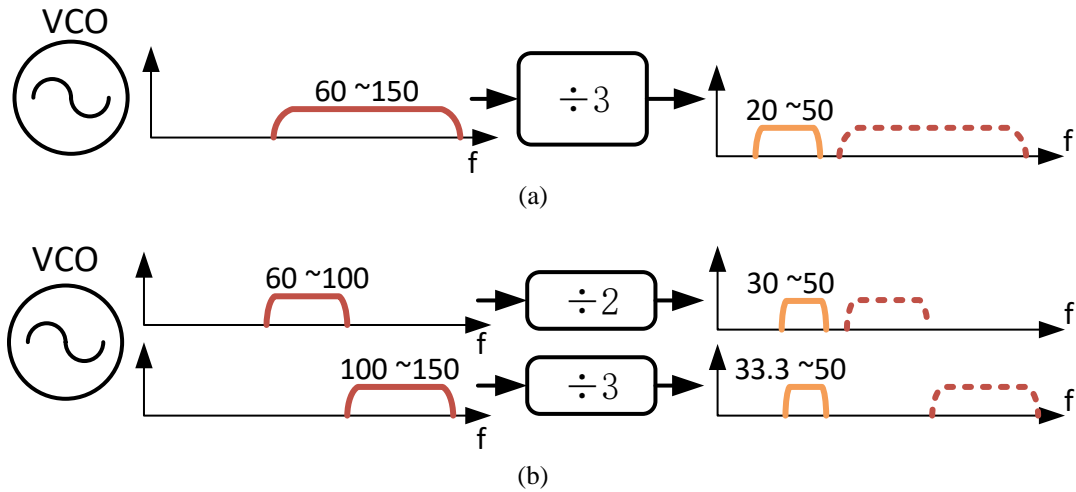


Fig. 3.1 An example shows the frequency translation of (a) a single divide-by-3 divider and (b) a dual-mode divider.

In the divider chain, the first stage divider normally has a lower divide ratio but a high working frequency and wide working bandwidth to cover the entire VCO tuning range. If the first stage divider has multiple divide ratios, the required bandwidth of later stage dividers can be smaller.

3.2 Overview of frequency dividers

There are four traditional types of traditional frequency dividers: static, dynamic, miller, and injection-locked frequency dividers (ILFD). They have different advantages for different applications. Static frequency dividers normally have a very wide operational bandwidth starting from direct current (DC). Its power consumption is normally quite high for tens to several hundred milliwatts (mW). Dynamic frequency dividers can achieve a very high operating frequency. In addition, it requires an adequate input signal power level, normally more than 0 dBm. Regenerative frequency dividers, also known as Miller dividers, obtain divided output by mixing the input signal with a feedback signal from the mixer. This feedback structure is simple, but the circuit must satisfy certain phase shift requirements. Injection locked frequency dividers can operate in a higher frequency band with much lower power consumption. However, the tuning range is limited by its resonator, and it has been considered a major barrier for practical applications [74]. Table 3.3 summarizes the different kinds of millimeter-wave frequency dividers that are recently published.

Multi-mode frequency dividers are often realized with ILFD topology [75-80]. In paper [75], a pair of switched capacitors are used as a capacitive load. When the switched capacitor is bypassed, the divider is in the divide-by-2 mode. When the switch is on, the capacitor shifts the resonator frequency of the tank, so the divider is switched to divide-by-3 mode. Similarly, in paper [76], the divide ratio is toggled using either single-ended input or differential input. When there is a differential input, the divider works in the divide-by-3 mode; when there is a single-end input, the divider works in the divide-by-2 mode. In paper [77-80], dividers are realized by

an LC-tank oscillator and an injection MOS transistor. The output signal is mixed with the input signal to realize the division. By emphasizing the first and second harmonics of the mixed-signal, the divide ratio two and three can be achieved. A BPF is used to limit the output frequency range so that the divider works either in divide-by-2 mode or divide-by-3 mode. Most of the dual-mode frequency dividers use a pair of varactors to tune the working frequency [76-78][80] so that a wide working range can be achieved.

Table 3.3 Published millimeter-wave frequency dividers.

Ref	Technology	Frequency range (÷2) (GHz)	BW (÷2) (GHz)	Frequency range (÷3) (GHz)	BW (÷3) (GHz)	Pin (dBm)	Divider type	Chip size (μm^2)	P_{DC} (mW)
[75]	0.18 μm CMOS	3.44~5.02 (37.4%)	1.58	4.28~4.81 (11.7%)	0.53	-0.5	ILFD	1200×730	3.15
[76]	0.35 μm CMOS	4.56~5.59 (20.3%)	1.03	6.94~8.41 (19.2%)	0.47	10	ILFD	762×782	15.2
[77]	0.18 μm CMOS	3.18~4.05 (24%)	0.87	4.85~5.7 (16.1%)	0.85	5	ILFD	800×800	12.5
[78]	0.18 μm CMOS	8.42~10.95 (26%)	2.53	13.66~16.03 (16%)	2.37	0	ILFD	467×716	4.17
[79]	0.35 μm CMOS	1.5~2.05 (31%)	0.55	1.74~1.95 (11.4%)	0.21	0	ILFD	56×10 ⁴	1.49
[80]	0.18 μm CMOS	5.37~7.68 (35.4%)	2.31	8.07~11.4 (34.2%)	3.33	0	ILFD	--	3
[81]	0.18 μm BiCMOS	--	--	132.5~140.4 (5.8%)	7.9	-2	ILFD	670×600	71.2
[82]	90 nm CMOS	--	--	91.8~109.8 (17.9%)	18	--	ILFD	870×775	0.13
[83]	40 nm CMOS	--	--	236.6~245.2 (3.6%)	8.6	9.5	ILFD	620×430	3.3
[84]	65 nm CMOS	--	--	58.6~67.2 (13.7%)	8.6	0	ILFD	870×530	5.2
[86]	0.13 μm BiCMOS	47~217 (129%)	170	--	--	6	Dynamic	474×446	171
[87]	0.13 μm BiCMOS	38~189 (133%)	151	--	--	5	Dynamic	474×446	217
[88]	0.13 μm BiCMOS	6~75 (170%), 100~128.7 (25%)	69, 28.7	--	--	10	Static	765×765	196
[74]	0.13 μm SiGe BiCMOS	40~90 (77%)	50	--	--	-7	Static	650×500	61.6
[89]	0.2 μm SiGe:C bipolar	51~168 (106.8%)	117	--	--	7	Miller	580×480	105
[90]	100 nm SiGe BiCMOS	122~242 (66%)	120	--	--	3	Dynamic	420×330	155.76
[91]	SiGe Bipolar	74-136 (59%)	62	--	--	0	Dynamic	1780×630	72.6
[C]	0.13 μm BiCMOS	70~114 (47.8%)	44	105~160 (41.5%)	55	-1	Dynamic	530×460	26~180

In this thesis, a dynamic frequency divider is proposed with the dual operation mode, divide-by-2 and divide-by-3. The divider is based on a novel tunable delay gated ring oscillator (TDGRO) topology. It has a very wide working range from 70-160 GHz. For divide-by-2 mode, it works from 70-114 GHz. For divide-by-3 mode, it works from 105-160 GHz. The output of the divider falls in the range of 35-57 GHz for both working modes. Compare with the published dual-mode frequency dividers shown in Table 3.3, the proposed dynamic frequency divider has the highest operating frequency of 160 GHz. Compared with the divide-by-3 frequency dividers, it also has a state-of-the-art operational bandwidth of 55 GHz.

3.3 Proposed frequency divider topology

The proposed TDGRO dynamic frequency divider has a simplified functional diagram shown in Fig. 3.2. The TDFRO topology comprises two gated differential amplifiers, Amp1 and Amp2, with a feedback connection to form a ring oscillator configuration. Two tunable delays are inserted between two amplifiers to tune the operation frequency. The tunable delay, denoted at τ , is tunable with the current. Two amplifiers are gated by the same clock, f_{in} , but with 180 phase offsets. They are turned on at high and low voltage, respectively. A similar structure without tunable delays has been used in a divide-by-2 frequency divider [85].

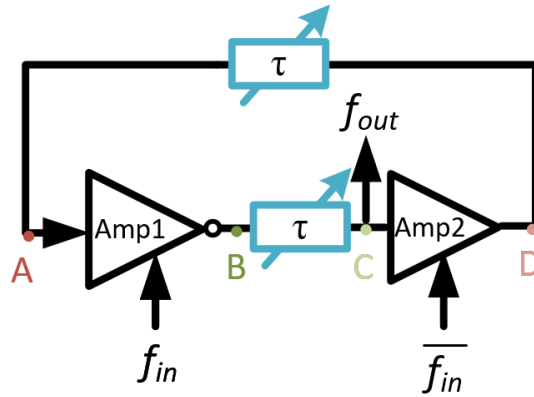


Fig. 3.2 A simplified TDGRO frequency divider topology [C].

In Fig. 3.2, four nodes are marked as A, B, C, and D, which are at the input and output of two amplifiers. The voltage state on these four nodes will be discussed and presented in Fig. 3.3 to show how this divider circuit works. Assume the initial states of four nodes are all at a low voltage state. When the clock signal is high, Amp1 operates. The state of the node B will be flipped as an opposite state of that at node A with a delay of τ_{AB} . Then, the state is passed to node C with a delay of τ_{BC} . Similarly, when the clock signal becomes low, the state of node C will be passed to node D through Amp2 with a delay of τ_{CD} . The state of node D will be further passed back to node A with a delay of τ_{DA} . There is a restriction: the state of nodes A and C can only be passed to nodes B and D within the working clock period of Amp1 and Amp2. Which means if the delay is too much, the state may not be passed to node B and D since the working clock period is passed. Considering the circuit symmetry, assume $\tau_{AB} + \tau_{BC} = \tau_{CD} + \tau_{DA} = \tau$, and $\tau_{AB} = \tau_{CD}$, $\tau_{BC} = \tau_{DA}$.

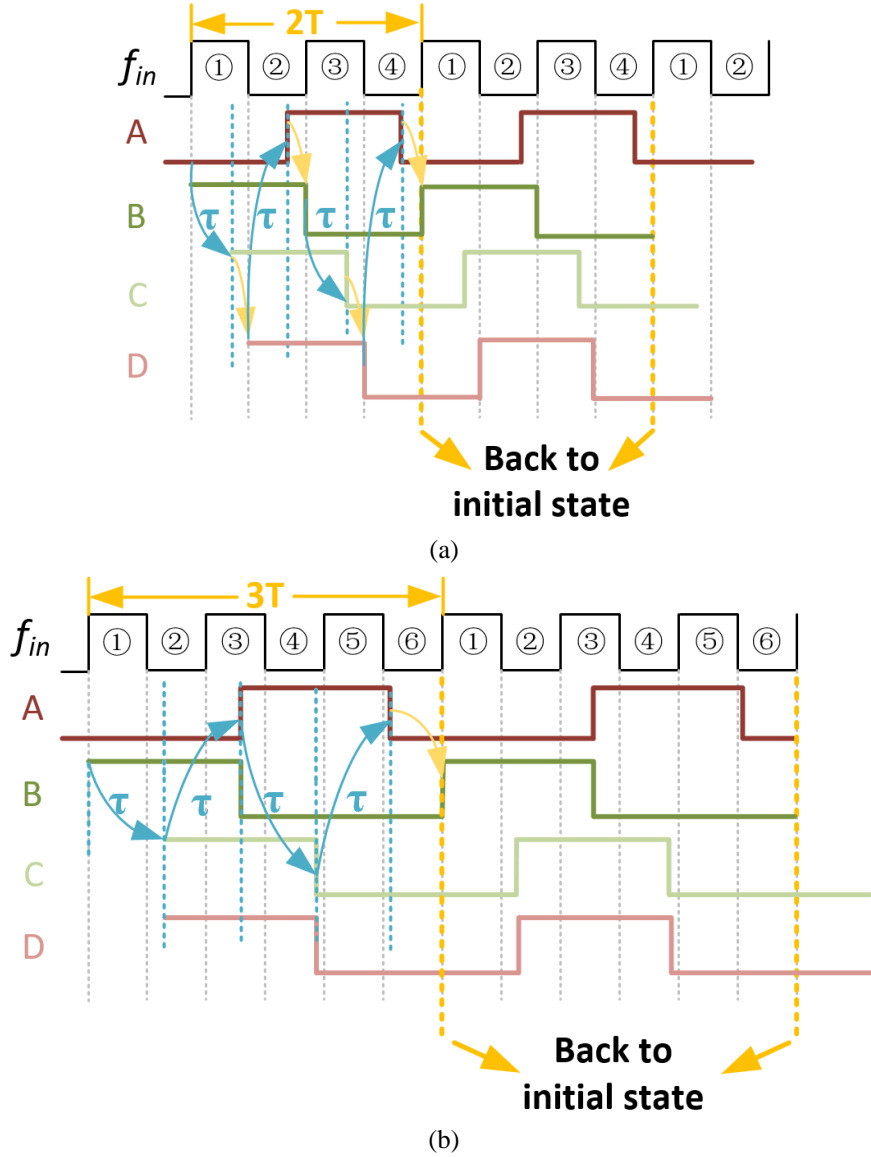


Fig. 3.3 An illustration of states of four nodes when the circuit operates as (a) divide-by-2 and (b) divide-by-3 [C].

When the frequency divider operates as divide-by-2, the states of four nodes are depicted in Fig. 3.3 (a). Clock periods are numbered from slot ① to slot ④ for a better explanation. The state of node A needs to change two times within two clock period to realize a divide-by-2 function. The state of node A changes after all the other three nodes have changed. The state of node A is passed from node C after the clock becomes negative. Under these restrictions, the rising edge of node A should be in slot ②, and the falling edge of node A should be in slot ④. The minimum time for node A to change a state is $\tau_{AB} + \tau_{BC} + \tau_{CD} + \tau_{DA} = 2\tau$. As a result, there is a time constraint of $4\tau \leq 2T$, where T is a clock period. There is no lower limit for τ . As long as $\tau \leq T/2$, node A and C are always ready to transfer the state to the next node before the working clock period comes. This waiting period is shown as the yellow arrow in Fig. 3.3. As a result, the maximum divide-by-2 operation frequency is:

$$f_{div2} \leq \frac{0.5}{\tau}, \quad (3.1)$$

where $f_{div2} = 1/T$.

When the frequency divider operates as divide-by-3, the states of four nodes are depicted in Fig. 3.3 (b). Clock periods are numbered from slot ① to slot ⑥ for a better explanation. The time constraint can be derived from the following steps.

- 1) The state of node A needs to change two times within three clock period to realize a divide-by-3 function so that

$$4\tau \leq 3T. \quad (3.2)$$

- 2) According to the previous analysis in divide-by-2 operation, the rising edge of node A should be in slot ③. Otherwise, the divider operates divide-by-2 so that

$$\tau \geq T/2. \quad (3.3)$$

- 3) The falling edge of node A needs to be in the time slot ⑥ so that all four nodes' state back to initial low state before the next three clock period. In this case,

$$2.5T \leq 4\tau \leq 3T. \quad (3.4)$$

- 4) There is a delay τ for the state passing from node C to node A so that the falling edge of node C and D must come before slot ⑥. The state of node C can only be passed to node D during a negative clock period. In this case, the falling edge of node C and D is in slot ④, and the rising edge of node C and D is in slot ②. In this case,

$$\begin{cases} 1.5T \leq 3\tau \leq 2T, \\ T/2 \leq \tau \leq T. \end{cases} \quad (3.5)$$

As a result, there is a time constrain of $0.625T \leq \tau \leq 0.67T$ for the divide-by-3 mode. The divide-by-3 frequency range can be written as:

$$0.625/\tau < f_{div3} < 0.67/\tau. \quad (3.6)$$

Eq. (3.1) and Eq. (3.6) show that for a given delay τ , the maximum working frequency can be improved by a third with the same τ .

3.4 Circuit structure and tunable delay simulation

Fig. 3.4 shows the schematic of the proposed dual-mode frequency divider. The two amplifier pairs are formed by Q1~Q2 and Q3~Q4, gated by Q9 and Q10, respectively. Q5~Q8 are emitter follower stages that work together with transmission lines (TLs) as inter-amplifier buffers. Q17~Q20 are their current mirrors. Q11~Q13 form the clock input stage. Q14~Q16 form the complementary stage.

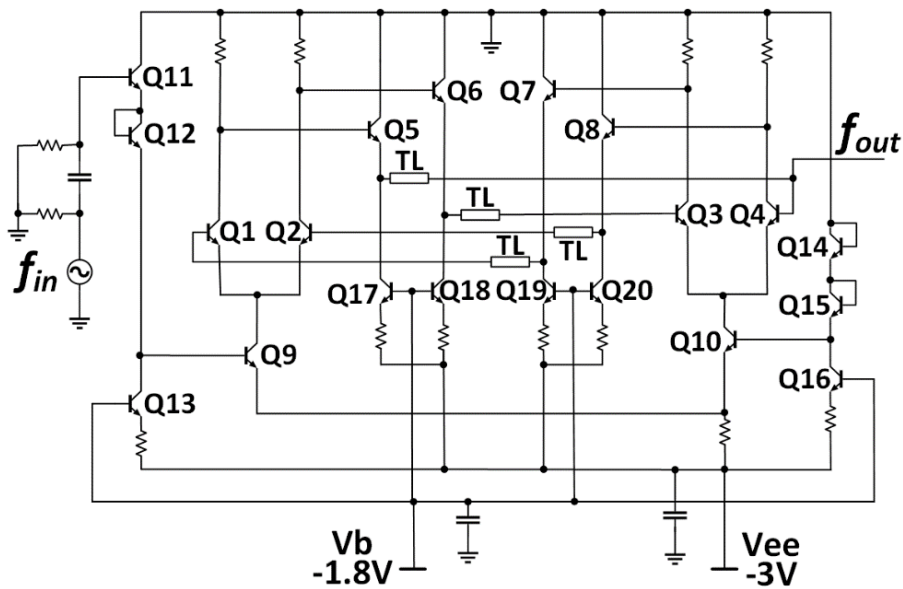


Fig. 3.4 The schematic of the proposed dual-mode frequency divider [C].

The tunable delay τ that is mentioned in the last section is formed by the delay from the transistor's bipolar junctions and transmission lines. The transmission line is an inevitable part of the layout that provides a fixed delay, while the delay from the bipolar junctions is tunable. When the current I_c at the collector changes, the delay between the base and the collector from the amplifier stage τ_{bc} changes. Moreover, the delay between the base and the emitter from the emitter follower stage τ_{be} also changes with I_c . As a result, the delay between the two amplifiers is tunable.

The fixed electric delay of the transmission line and the tunable delay from transistors are calculated in HFSS and Cadence simulation, respectively. The electric delay of the transmission line is 0.4 ps. By observing the time delay between the signals at the input of the first amplifier (base of Q1) and the input of the second amplifier (base of Q4) when the divider is free running, the total tunable delay τ is estimated.

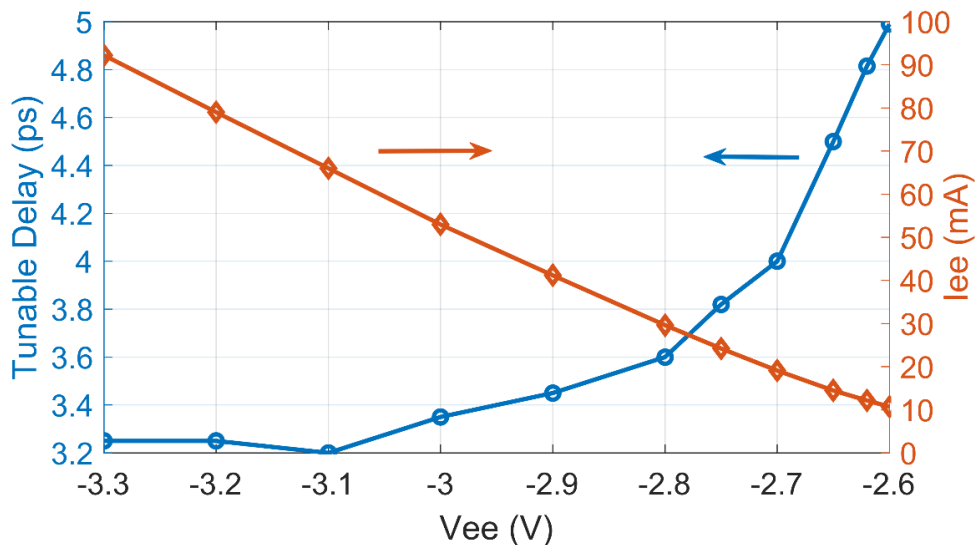


Fig. 3.5 The simulated tunable delay with different bias conditions [C].

The simulated tunable delay with different bias conditions is shown in Fig. 3.5. This delay is non-removable but can be tuned from 3.6 ps to 5.4 ps. From the analysis in the previous section, the delay τ determines the working frequency. The divide-by-2 mode should work up to 139 GHz, and the divide-by-3 mode should work from 116GHz to 186 GHz. From the desired working frequency, the delay τ can be calculated from Eq. 3.1 and Eq. 3.6. For a higher working frequency, the delay needs to be smaller. In our case, the transmission line provides a 0.4 ps delay, which is the smallest delay we can have in the layout. To reach a higher working frequency, the layout needs to be optimized with shorter transmission lines.

3.5 Performance verification and discussion

The frequency divider circuit is designed with a 130 nm gate length SiGe BiCMOS technology which has an f_t and f_{max} of 250 GHz and 370 GHz, respectively. The circuit is tested on-wafer. A picture of the layout and a photo of the on-wafer chip are shown in Fig. 6. The size of the chip is $530 \mu\text{m} \times 460 \mu\text{m}$, including probing pads. A photo of the measurement using a probe station in the lab environment is shown in Fig.3.7.

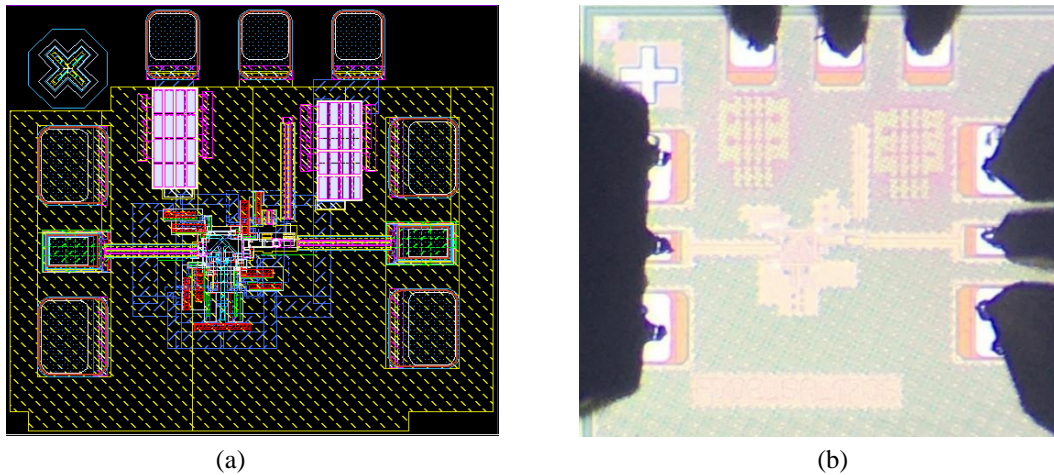


Fig. 3.6 (a) A picture of the layout, and (b) a photo of the on-wafer chip [C].

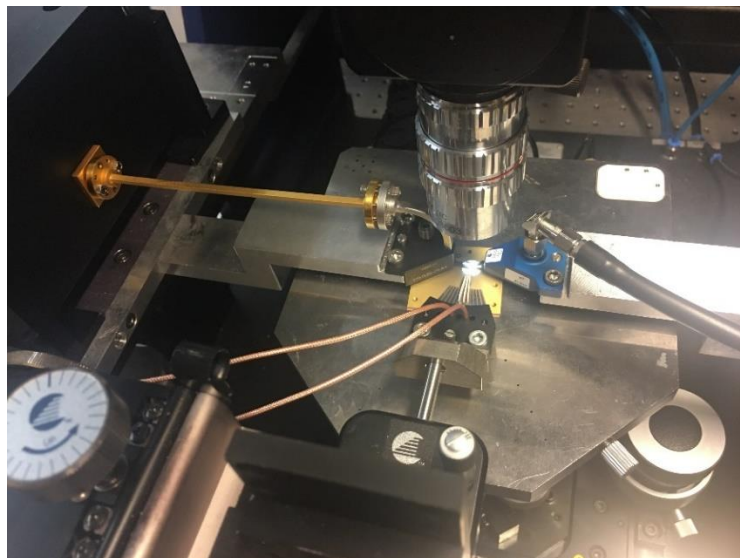


Fig. 3.7 A photo of the measurement in the lab.

The output signal power and bias conditions over input frequencies is measured and shown in Fig. 3.8. The input power is constant -1 dBm. Each curve represents a working frequency range under a single bias point. The circuit has two biases, Vee and Vb, supplied respectively at -3 V and -1.8 V. By changing the bias voltage of Vee, the frequency divider can work from 70 GHz to 160 GHz. Among that, the divide-by-2 function covers 70 GHz to 114 GHz, and the divide-by-3 function covers 105 GHz to 160 GHz. DC power consumption varies from 26 mW to 180 mW. Compare with the simulation result, there is a 25 GHz working frequency offset.

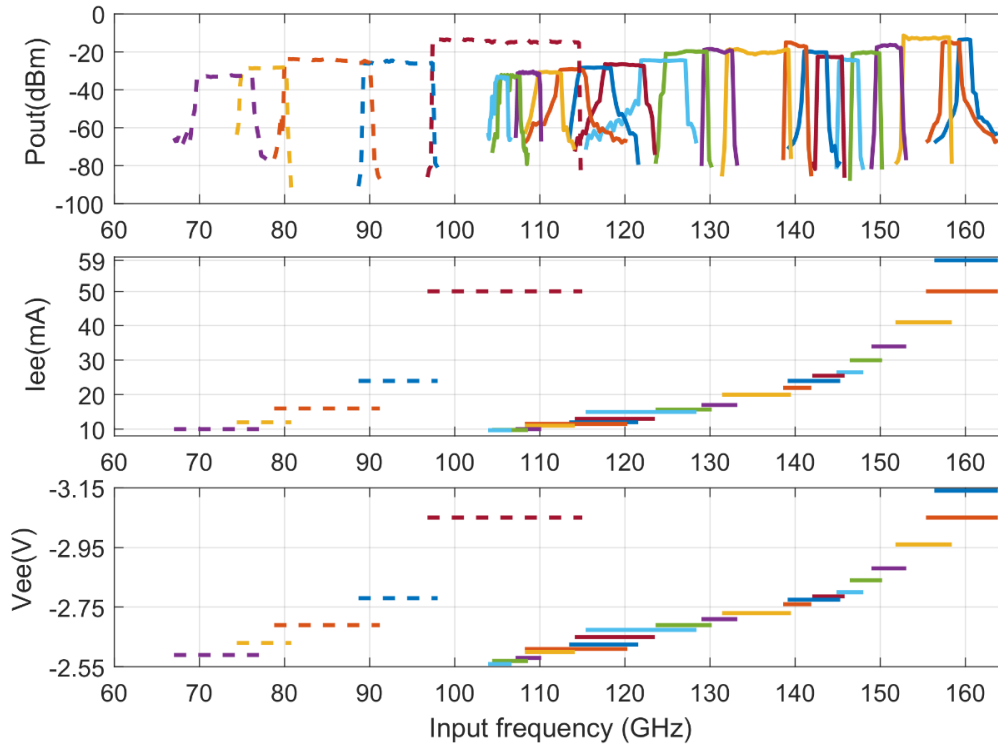


Fig. 3.8 The output signal power over input frequencies [C].

Fig. 3.9 shows the input sensitivity of the proposed frequency divider. The claimed wide working bandwidth is achieved by having -1 dBm input power. At the most sensitive part, it only needs -24 dBm input power to work. Compare with other published dynamic frequency dividers [86-87] [89-91], it is quite sensitive.

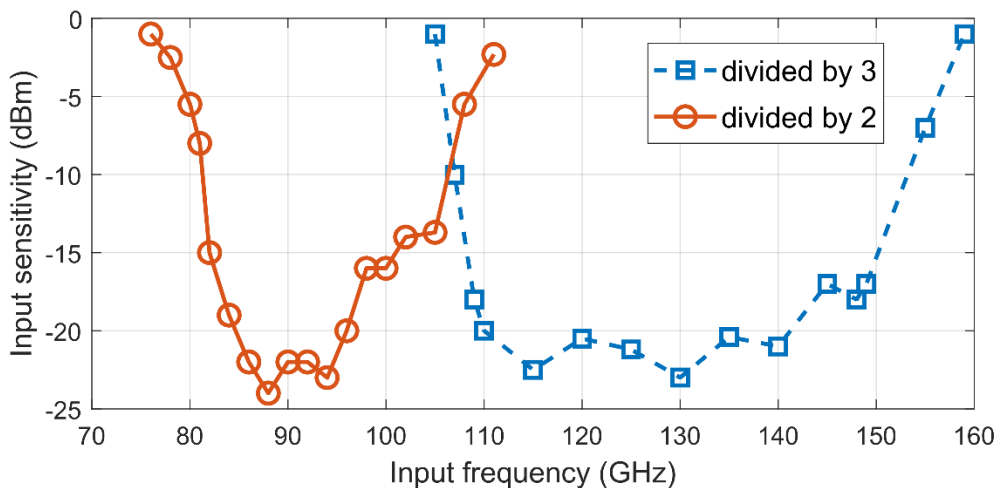


Fig. 3.9 The input power sensitivity curve of the dynamic divider [C].

Fig. 3.10 and 3.11 show the measured output spectrum of the divider under divide-by-2 and divide-by-3 mode. The input power is -1 dBm and -2.3 dBm, respectively.

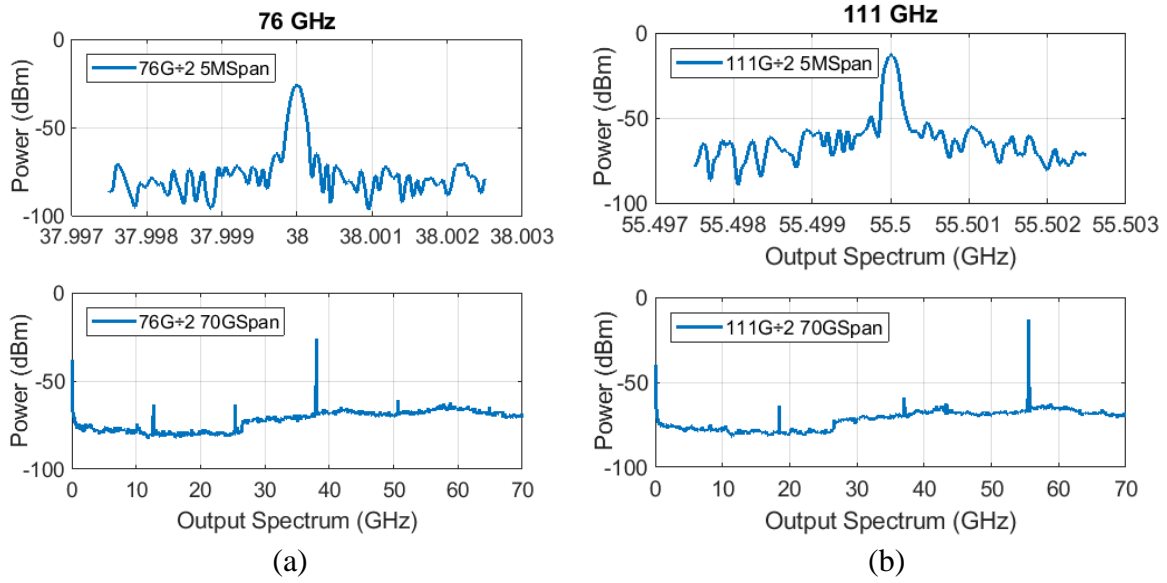


Fig. 3.10 The output signal spectrum of the divide-by-2 operation at (a) 76 GHz and (b) 111 GHz [C].

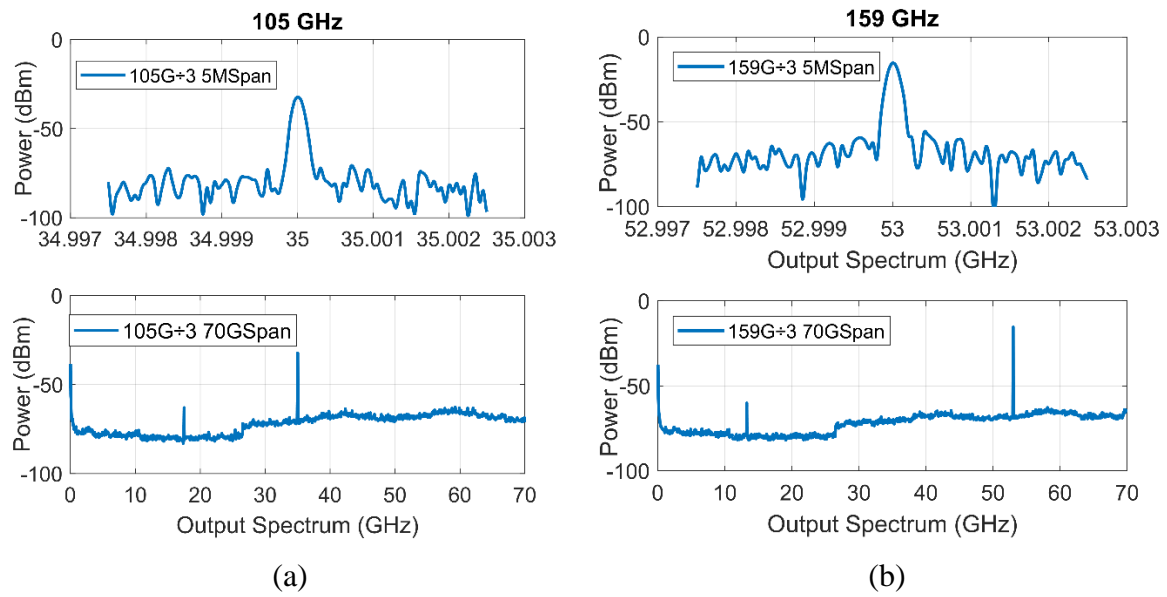
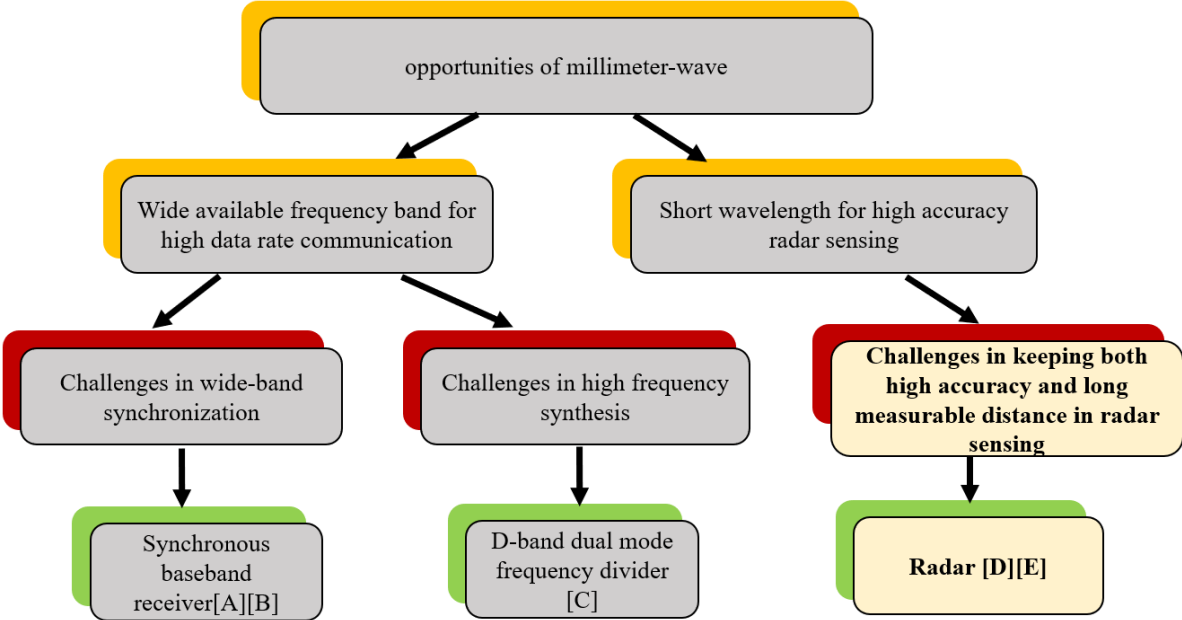


Fig. 3.11 The output signal spectrum of the divide-by-3 operation at (a) 105 GHz and (b) 159 GHz [C].

Chapter 4

Millimeter-wave Radar Sensing



4.1 Overview of millimeter-wave radar systems

There are mainly three kinds of traditional sensors for range measurement: ultrasonic, laser, and radar. They all have different advantages and limitations. As discussed in Chapter I, the ultrasonic sensor is sensitive to measurement environment changes, and its measurement distance is short; the laser requires a clear view, which is not viable in some applications; while radar sensors can detect the object in a non-visible condition and has a long measurement distance.

For millimeter-wave sensors, several radar systems are widely used. FMCW radar gains its popularity these days in the industry for its high accuracy. It transmits a chirp signal to estimate the distance and track the movement of the target. The chirp signal occupies a certain bandwidth. Wider bandwidth is required to achieve high accuracy and resolution [92-94]. In traditional FMCW radars [95-96], when bandwidth requirements exceed 1 GHz, its accuracy and resolution are limited by the linearity of the frequency slope of the chirp signal. Typically, when co-located FMCW radars share the spectrum, interference would occur unless a dedicated chirp scheduling plan is made.

Interferometric radar also has very high accuracy. It transmits a CW signal. For a millimeter-wave signal used in the radar system, it can detect micrometer level object motion. However, its unambiguous detection distance equates to half wavelength [97]. To extend the unambiguous distance, multi tones can be used. For example, two tones measurement was proposed in [98-99]. The detection window can be extended correspondingly depending on the number of tones and the tones' separation in frequency.

For phase modulated radars, a sequence of binary symbols that are modulated to a radio frequency carrier is used in the system. Different coding can ensure multiple radars coexist within the same spectrum slot. Phase modulated radar has the advantage of long measurement distance but at the expense of lower accuracy, which is often limited by the modulation bandwidth [100-104]. In paper [D], a random binary phase modulated (RBPM) radar system is proposed with enhanced accuracy. With the help of the carrier phase information, the accuracy of the proposed radar system can achieve a micrometer level.

OFDM radar waveform has been proposed in [105], which can perform radar sensing and communication simultaneously. There is data modulated on each subcarrier. By applying different signature codes to each radar sensor, OFDM radar can work in a multi-user scenario. Traditional OFDM radar has a range accuracy inverse proportional to the bandwidth B of the transmitted signal, as $\delta R = c_0/2B$, where c_0 is the speed of light. This accuracy figure is the result of using an IFFT operation. In paper [E], a fractional step IFFT method is used to enhance the accuracy of the OFDM radar. The carrier phase is also used to assist in increasing the range accuracy to $\pm 20 \mu\text{m}$.

Our work [D] and [E] are compared with the recently published high accuracy radar works in Table 4.1.

Table 4.1 Recently reported radar work [D][E].

Ref.	Freq. (GHz)	Bandwidth	Method	Accuracy (μm)	Measured Distance	Unambiguity Distance
[92]	122.5	1 GHz	FMCW	± 2	5 mm	>1 km
[93]	124	6 GHz	FMCW	± 6	35 mm	>1 km
[94]	80	10 GHz	FMCW	± 0.5	2 mm	>1 km
[97]	24	Single tone	Interferometer	± 0.5	10 μm	12.5 mm
[98]	24	Two tone	2-tone Interferometer	± 200	60 mm	60 mm
[99]	78.1	Two tone	AMCW	± 8	8 mm	15 cm
[104]	79	4 GHz	Phase modulated	15×10^4	15cm	37.5m
[D]	79	2 GHz	OFDM	± 22	8 mm	>1 km
[E]	80	2 GHz	Phase modulated	± 7	20 mm	>1 km

4.2 Three radar principles

In this section, the principles of traditional CW radar, random binary phase modulated (RBPM) radar, and OFDM radar are introduced. Their advantages and disadvantages are discussed.

4.2.1 CW radar

For the CW radar, a single tone CW signal is generated and sent out from the radar side. Then it is reflected by the target surface. The signal traveling time translates to a received signal phase rotational offset. The phase offset is normally calculated by mixing the reflected signal with the transmitted CW signal. From the phase offset, the distance from the radar to the target can be calculated by

$$d = \frac{\varphi}{2\pi} \times \frac{c}{f_c} \times \frac{1}{2}, \quad (4.1)$$

where φ is the phase offset, c is the speed of light, f_c is the CW tone frequency. To simplify the analysis, the internal delay inside the radar is ignored here. Eq. 4.1 shows that the accuracy of the distance estimation d depends on the phase offset estimation accuracy and the CW tone frequency. With a higher frequency, the same distance d will translate to a larger phase offset φ . In this case, finer distance displacement can be detected. In addition, the phase estimation error φ_e gives a smaller distance error d_e with a higher CW frequency. Thus, the distance estimation is more accurate. On the other hand, the unambiguous phase offset of a CW signal is 2π so that the range detection window for the CW radar is one wavelength. As a result, the CW radar has high accuracy with a trade-off of limited unambiguous measurement distance.

4.2.2 Phase modulated radar

In a phase modulated radar system, a random binary phase modulated (RBPM) signal is used for sensing. The traveling time is estimated by correlating the transmitted and reflected signal. The correlation is normally realized in a digital platform with a sliding correlator [101-103] so that the reflected signal is correlated with the transmitted signal with different time delays. The baseband RBPM signal can be represented as $x(n)$ with two symbols, -1 and 1. Assume the random binary sequence has a length of L , its autocorrelation property can be analyzed as follows.

The peak value of autocorrelation is a function of sequence length:

$$\int_{n=0}^L x(n) \times x(n) = L, \quad x(n) = \{-1,1\}. \quad (4.2)$$

When it correlates with $x(n + \Delta n)$, the correlator outputs

$$\int_{n=0}^L x(n) \times x(n + \Delta n) \approx 0 \ll L. \quad (4.3)$$

With the sliding correlator, Δn is tuned from $-L$ to L . When the reflected signal $x(n)$ is received by the radar side, the transmitted signal, at the same instance, can be represented as $x(n + m)$. The sliding correlator gives the highest output when $\Delta n = m$. In this case, the time delay is calculated with an accuracy of one symbol period. The unambiguous measurement distance is determined by the length of the binary sequence L and the symbol rate R_s as

$$d_{\max} = L \times \frac{c}{R_s} \times \frac{1}{2}. \quad (4.4)$$

By using a longer binary sequence or higher symbol rate, the unambiguous distance can be further increased. As a result, the phase modulated radar has a long unambiguous distance but a low accuracy of $\frac{c}{2R_s}$.

4.2.3 OFDM radar

An OFDM signal can be denoted as a composite of multiple carrier signals, modulated with different data. The carriers are orthogonal to each other so that the spectra can be overlapped, and the demodulation can be done without interference. Fig. 4.1 shows the spectrum of an OFDM signal. There are five signals modulated on five subcarriers. When it is used in a radar system, signals in each subcarrier have a different phase offset. The phase offset is related to the frequency of the subcarrier as CW radar. The phase offset of each subcarrier φ_n can be represented as

$$\varphi_n = 2\pi f_n \times \frac{2d}{c}, \quad (4.5)$$

where f_n is the frequency of the n th subcarrier. φ_n can be further represented as

$$\varphi_n = N_n \times 2\pi + \varphi_n', \quad (4.6)$$

where $\varphi_n' < 2\pi$. Only φ_n' can be observed from the phase of the transmitted and reflected signal, N_n is unknown. As a result, the unambiguous distance of a single tone CW radar is one wavelength. In OFDM radar, multiple carriers are used. When the subcarriers are closely located in the spectrum, the difference between each φ_n is very small. In this case, it is possible that N_n keeps the same for all φ_n . When two subcarriers are used in the radar system,

$$\varphi_n - \varphi_{n-1} = \varphi_n' - \varphi_{n-1}' = 2\pi(f_n - f_{n-1}) \times \frac{2d}{c}, \quad (4.7)$$

the unambiguous distance is extended to one wavelength of $\Delta f = f_n - f_{n-1}$. In addition, the modulated symbols can increase the unambiguous distance further as the phase modulated

radar. When phase error exists, the distance estimation is not accurate. When multi subcarriers are used, the phase offset of each subcarrier can be presented as Fig. 4.2. The slope of the phase offset in Fig. 4.2 corresponds to the time delay $\tau = \frac{2d}{c}$. With more subcarriers used in the radar system, the distance estimation accuracy increases.

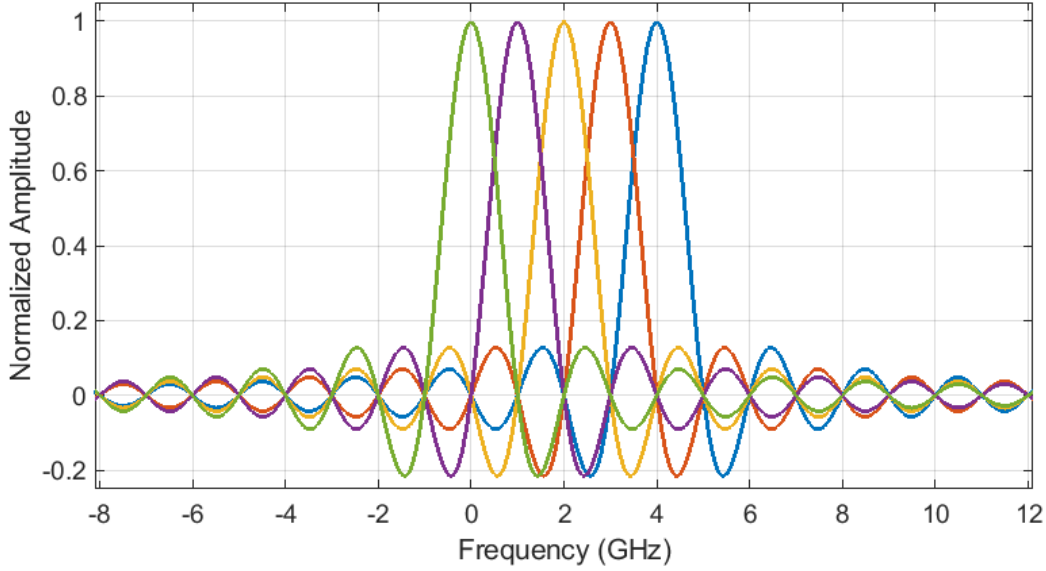


Fig. 4.1 An illustration of the spectrum of an OFDM signal.

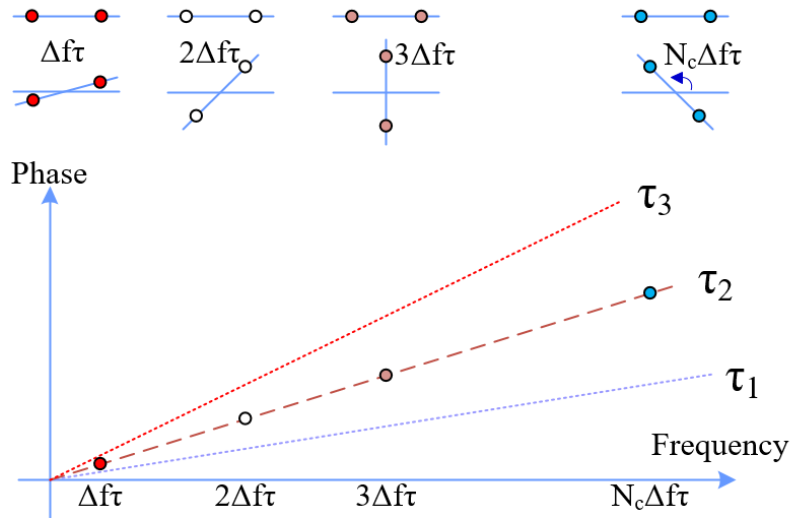


Fig. 4.2 An illustration of the phase offset at each subcarrier [E].

In a traditional OFDM radar system, the time delay estimation is done by applying inverse discrete Fourier transform (IDFT) to the group out phase offsets $[D]$ from subcarriers as

$$\begin{aligned} r(k) &= IDFT[D] = \frac{1}{N_c} \sum_{n=0}^{N_c-1} D(n) \exp\left(\frac{j2\pi}{N_c} nk\right) \\ &= \frac{1}{N_c} \sum_{n=0}^{N_c-1} \exp(-j2\pi n \Delta f \tau) \exp\left(\frac{j2\pi}{N_c} nk\right), \quad k = 0, \dots, N_c - 1. \end{aligned} \quad (4.8)$$

where N_c is the total number of subcarriers [105]. Two exponential terms would cancel each other and result in unity when

$$k = \Delta f N_c \tau. \quad (4.9)$$

In this case, $\tau = \frac{k}{\Delta f N_c}$. Using IDFT for estimation gives an advantage of being able to use a fast calculation method, inverse fast Fourier transform (IFFT), in digital platforms. On the other hand, the search step of τ is $\frac{1}{\Delta f N_c}$ so that it limits the estimation accuracy to $\frac{1}{\Delta f N_c}$, which leads to a distance estimation accuracy to $\frac{c}{2\Delta f N_c}$. The estimation accuracy is limited with the number of subcarriers and Δf .

4.3 Proposed radar systems

The previous section indicated that the CW radar has high accuracy but a short unambiguous distance. In contrast, the RBPM radar and OFDM radar have low accuracy but a long measurement distance. By combining two radar principles together, it is possible to achieve both high accuracy and long unambiguous measurement distance in a radar system. In papers [D] and [E], a two-step estimation method is used. The RBPM signal and OFDM signal are used for coarse estimation, while their carrier phase offset is used for fine estimation.

The distance between the radar and the target can be expressed as

$$d = \frac{\tau c}{2} = \frac{(N \times 2\pi + \varphi) \times c}{4\pi f_c} = \frac{N + \frac{\varphi}{2\pi}}{2} \times \lambda, \quad (4.10)$$

where f_c is the carrier frequency, λ is the carrier wavelength, $N \times 2\pi + \varphi$ is the total phase offset. N and φ are estimated during coarse estimation and fine estimation, respectively.

4.3.1 Phase modulated radar system

The proposed RBPM radar system is shown in Fig. 4.3. The baseband RBPM signal is generated from a digital platform and modulated to RF with an E-band transmitter module. An LO is used to provide the carrier signal to both transmitter and receiver modules. The reflected signal is down-converted to the baseband and correlates with the transmitted signal to estimate the distance.

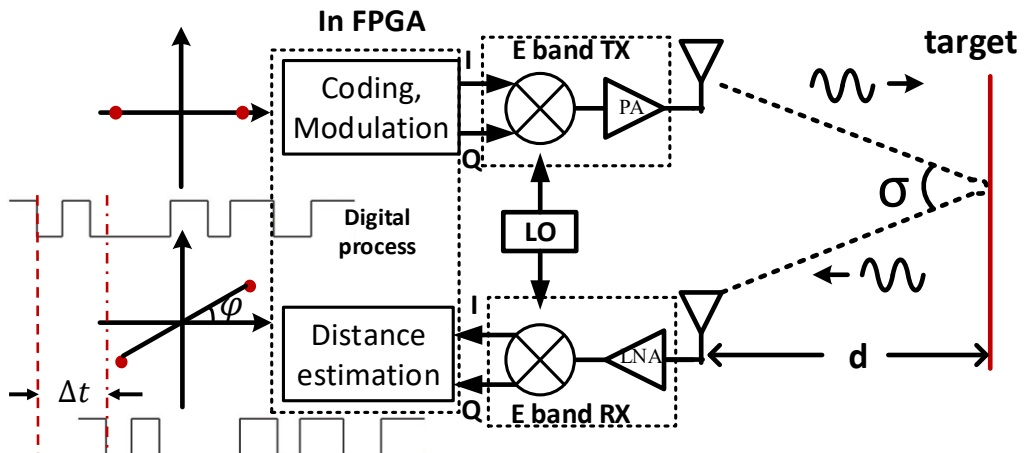


Fig. 4.3 An illustration of the proposed RBPM radar system [D].

The transmitted RBPM signal can be represented as

$$S_{tx}(t) = Ae^{j\theta} e^{j\omega_c t} = Ae^{j(\omega_c t + \theta)}, \quad (4.11)$$

where $\theta = \{0, \pi\}$ carries the binary data. The received signal can be represented as

$$S_{rx}(t) = A' e^{j[\omega_c(t-\Delta t) + \theta]} e^{-j\omega_c t} = A' e^{j(-\omega_c \Delta t + \theta)}, \quad (4.12)$$

where $\Delta t = \frac{2d}{c \times \cos(\sigma/2)}$, d is the distance between the radar and the target, σ is the angle between the transmission and reflection path. We assume that σ is smaller than 5 degrees and can be neglected. The phase offset is

$$-\omega_c \Delta t = \varphi + 2N\pi. \quad (4.13)$$

The distance can be calculated by Eq. 4.10. φ can be calculated from the received I and Q channel signal. The time delay Δt can be estimated by correlating the transmitted and received signal so that N can be estimated.

As introduced in section 4.2.2, a sliding correlator can provide a time delay Δt estimation with one symbol period accuracy. To get N , a higher accuracy within one carrier cycle period is need. For example, when the carrier frequency is 80 GHz and the symbol rate is 1 Gbaud, the accuracy needs to be improved 80 times. A straightforward solution is to sample the RBPM signal with 80 GSps ADC and do the slide correlation. When the transmitted and reflected signals are aligned, the correlator will give the highest output. However, it is impractical to use such high-speed ADCs in a real radar system. In paper [D], a matched filter-based estimation method is proposed that only requires a two times oversampling rate to achieve 80 times accuracy enhancement.

A root raised cosine (RRC) filter is used in the proposed radar system to limit the bandwidth. A received signal with a data rate of 1 Gbps and sampled by 2 GSps can be illustrated as Fig. 4.4 (a). The transmitted signal sampled by 2 GSps with different initial sampling positions are shown in Fig. 4.4 (b). Different groups of points are shown in different colors. Each group of points represents a full waveform matched filter (FWMF). The initial sampling position is changed with a step of $1/80$ sample period, which is also a half carrier cycle period. Applying the slide correlation to each FWMF with the received signal, the highest correlation value appears with the i^{th} FWMF with red color, as Fig. 4.4 (c) shows. Assume there are m samples offset between the received signal and the i^{th} FWMF, the time delay can be calculated as

$$mT_s + \tau_{i_{est}} = mT_s + i \times \frac{T_c}{2}, \quad (4.14)$$

where T_s is the sample period, and T_c is the carrier cycle period.

The random binary sequence used in the proposed system has a length of L . It is repeatedly sent out from the radar side. A flow diagram of coarse estimation implementation is shown in Fig. 4.5. The acquired samples from the reflected signal are first folded at a length L . The sampling points at the same sampling position in the sequence are accumulated to get a higher SNR. Then it passes the FWMFs and gets the coarse estimation.

Several practical aspects affect the reliability of the estimation. Using a higher symbol rate, a longer random binary sequence, a longer acquisition time, a higher sampling rate ADCs can help to increase the estimation reliability.

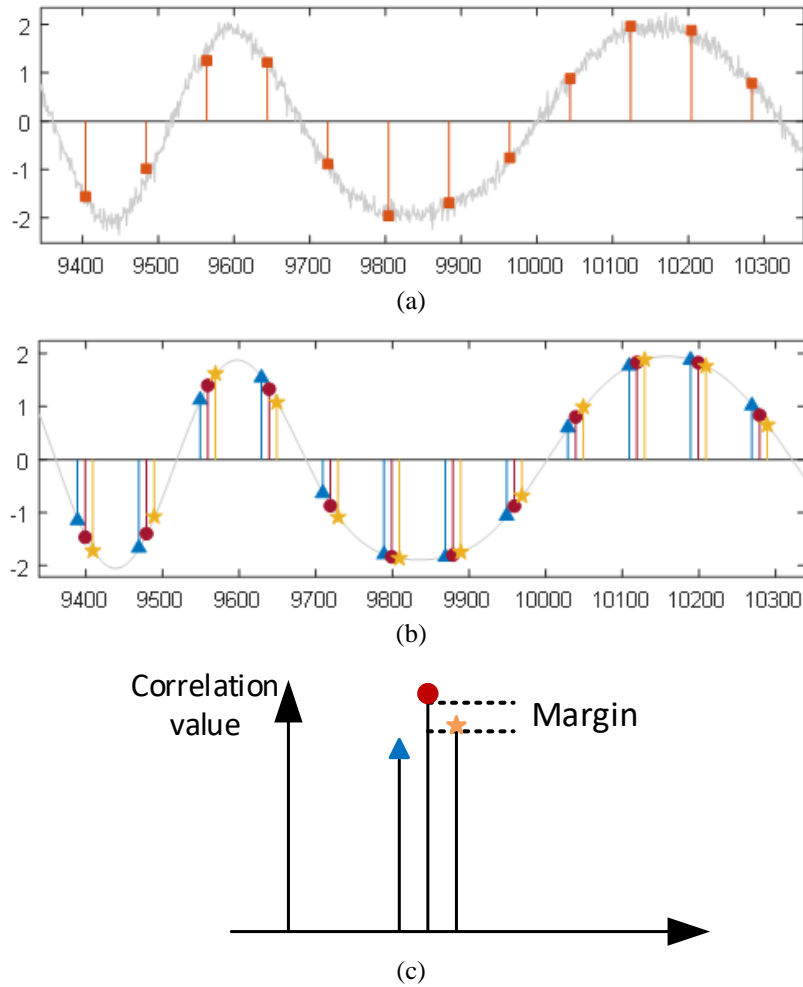


Fig. 4.4. (a) A typical reflected signal samples, (b) FWMFs, (c) Correlation result with different FWMFs [D].

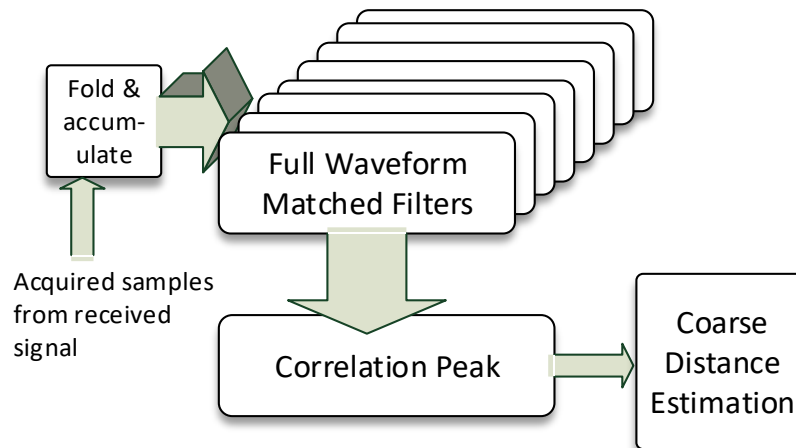


Fig. 4.5 Coarse estimation implementation flow diagram [D].

4.3.2 OFDM radar system

As discussed in section 4.2.3, the range estimation accuracy of the OFDM radar is limited with the number of subcarriers and Δf when using the IFFT. In paper [E], an accuracy enhancement method by using a fractional step of IFFT is proposed.

A fractional factor ma is introduced to Eq. 4.8 as

$$r(k) = \frac{1}{ma \times N_c} \sum_{n=0}^{ma \times N_c - 1} \exp(-j2\pi n \Delta f \tau) \exp\left(\frac{j2\pi}{ma \times N_c} nk\right). \quad (4.15)$$

The number of points that attend the IFFT calculation is increased by ma times. As a result, the search step of τ becomes $\frac{1}{ma \times \Delta f N_c}$. The estimation accuracy is increased correspondingly. This fractional factor insertion can be implemented by adding zeros to the signal and apply IFFT to it.

For example, assume there are 128 subcarriers are used in the system with a Δf of 15.625 MHz, the carrier frequency is 80 GHz, the target distance set at 240 mm and 243.75 mm of two tests. Without the fractional factor ma , the IFFT gives a result shown as Fig. 4.6. Two peak points of the two tests are the same. A distance displacement of 3.75 mm cannot be recognized. When the fractional factor $ma = 20$ is used, the fractional step IFFT results are shown in Fig. 4.7. Two simulation results have different peak locations. The distance estimation accuracy is increased to 3.75 mm.

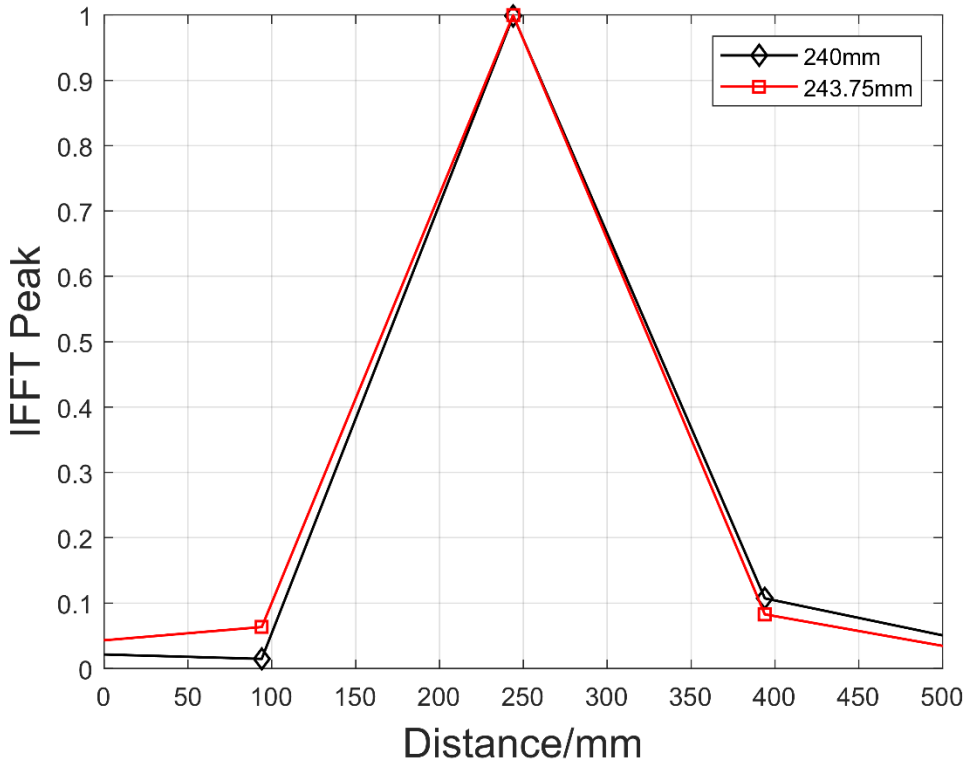
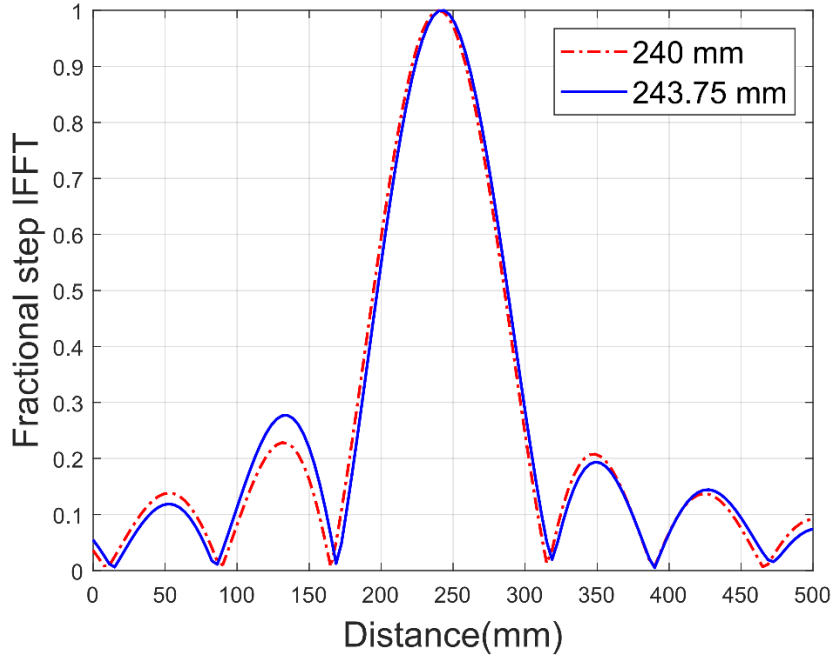
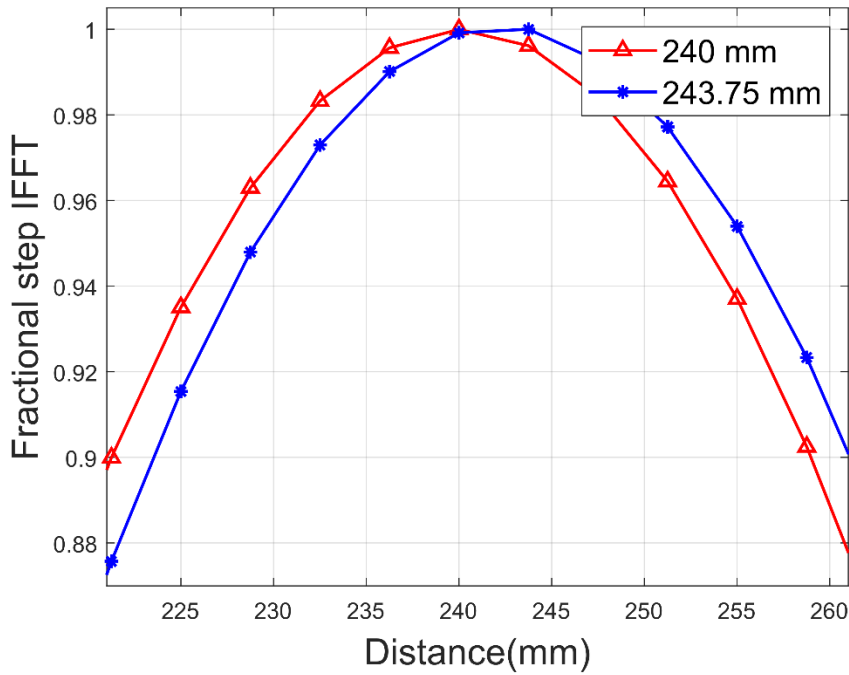


Fig. 4.6 The simulated IFFT results of two tests.



(a)



(b)

Fig. 4.7 (a) The simulated fractional step IFFT results for two tests, (b) a zoom-in view of the simulation results [E].

4.3.3 Fine estimation

For fine estimation, the phase φ in Eq. 4.10 and Eq. 4.13 is calculated by using the amplitude information of the I and Q channel signals. However, when there is an I/Q imbalance exist in the transceiver modules, channel I and channel Q are not 90-degree out of phase, the calculation of φ is inaccurate. The imbalance can be removed by applying equalization as

$$y(n) = x(n) + (\alpha + j\beta)x(n)^*, \quad (4.16)$$

where $x(n) = \cos(\varphi) + j\sin(\varphi)$, $x(n)^*$ is the conjugate value of $x(n)$. By tuning two parameters α and β , the imbalance can be removed [13-14].

Another challenge in phase estimation is the error caused by noise and interference. This problem can be solved by applying averaging to multiple symbols' phases in RBPM radar or phase differences from multiple subcarriers in OFDM radar.

When the distance estimation is applied by using the proposed methods, the internal delay inside the radar is included. To remove the internal delay, a calibration step of defining a measurement start position is needed. The measured distance becomes the relative distance between the target and the start position as

$$d_{meas} = d_1 + d_\epsilon - (d_0 + d_\epsilon) = d_1 - d_0, \quad (4.17)$$

where d_ϵ is the bias error caused by the internal delay, d_0 is the distance between the start position and the radar, and d_1 is the distance between the target and the radar.

4.3.4 Multi-user interference resistance

In the proposed RBPM radar and OFDM radar system, random binary sequences are used. For the OFDM signal, the random binary data is modulated to subcarriers. By using different Pseudorandom binary sequences (PRBS) for each radar in a multi-user scenario, the interference can be resisted. When two different PRBS correlate with each other, the result is very low, around 0. On the other hand, if the two input signals use the same PRBS, will the correlator output a very high value.

4.4 Performance verification and discussion

The measurement setup for both the proposed RBPM radar and OFDM radar is the same, and it is shown in Fig. 4.8. RBPM signal and OFDM signal are generated from an AWG. The reflected signal is sampled by an oscilloscope and sent into Matlab for processing. A pair of commercial E-band transceiver modules are used for up and down conversion. The target is a metal bar with an adjustable manual micrometer resolution positioner. A picture of the measurement setup in the lab is shown in Fig. 4.9.

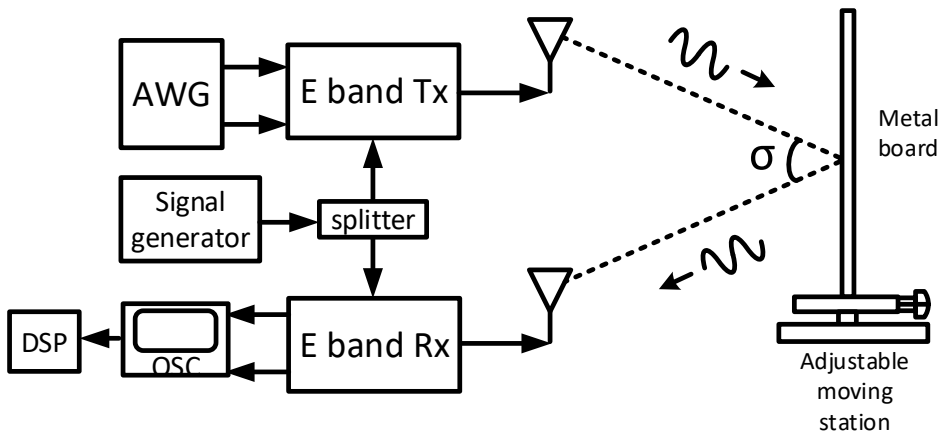


Fig. 4.8 The measurement setup for proposed radar systems [D].

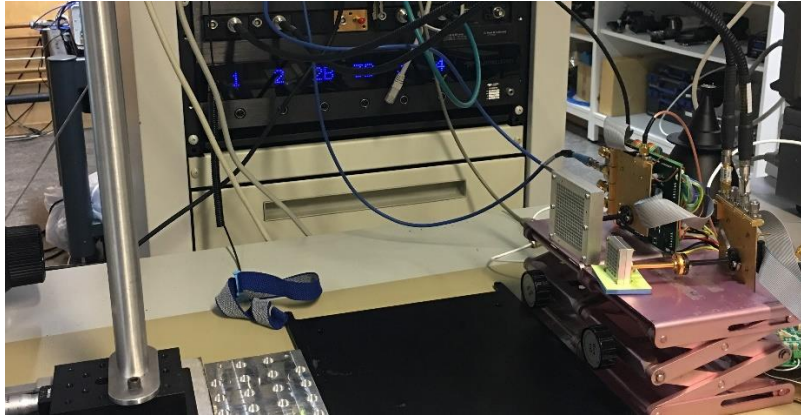


Fig. 4.9 The measurement setup in the lab [D].

4.4.1 Coarse estimation

For the proposed RBPM radar in paper [D], the random binary sequence in use has a length of 2000 symbols. The RBPM signal is 1 Gbuad and sampled by 2 GSps. 4000 samples were used for coarse estimation. The carrier frequency is 80 GHz. The coarse estimation result is shown in Fig. 4.10.

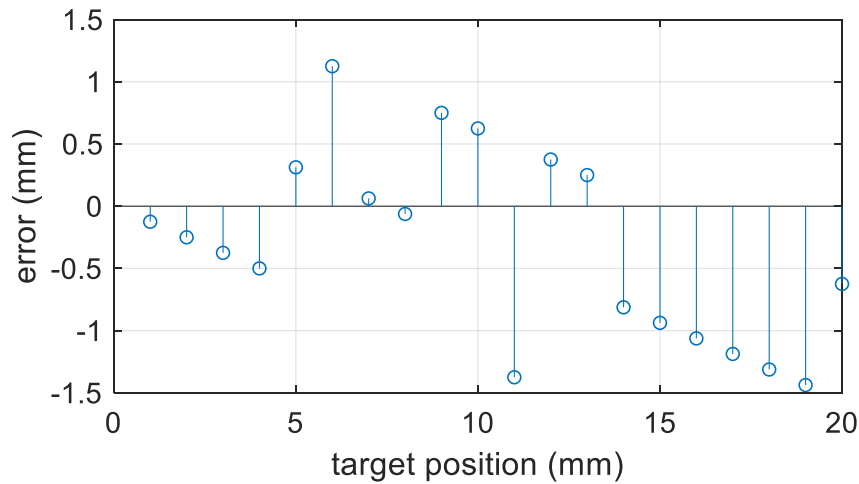


Fig. 4.10 The distance error versus actual target distance after coarse distance estimation [D].

For the proposed OFDM radar in paper [E], the OFDM signal has 128 subcarriers and occupies a total bandwidth of 2 GHz. The carrier frequency is 79 GHz in this measurement. The fractional factor ma in this measurement is 150. Fig. 4.11 shows the fractional step IFFT result when the target locates at three different positions with a relative distance of 3mm in between.

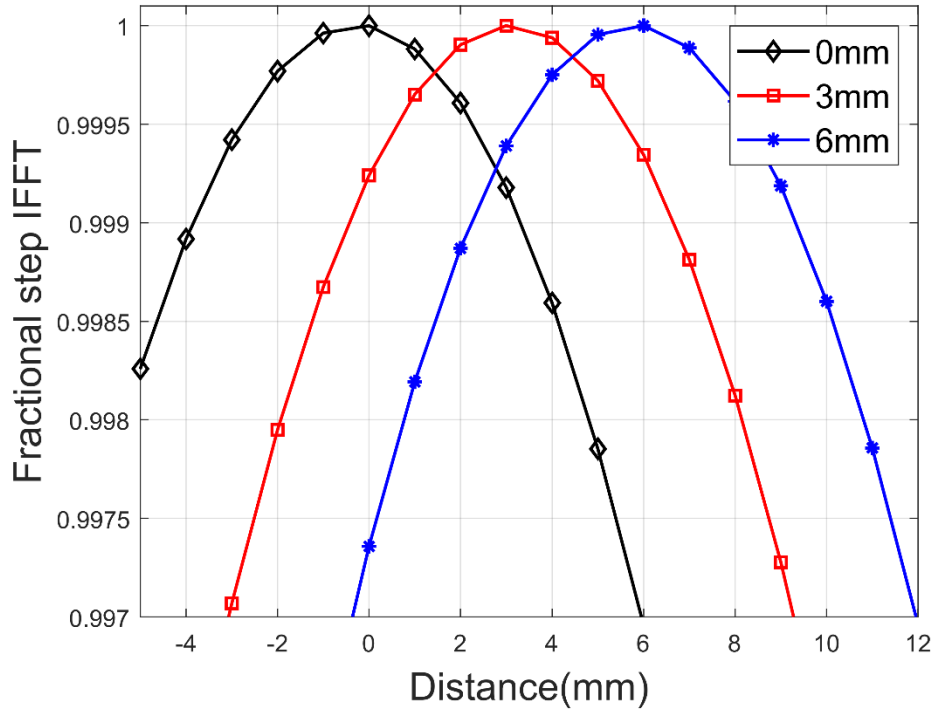


Fig. 4.11 The fractional step IFFT results for three measurements [E].

4.4.2 Fine estimation

For fine estimation, equalization is used in paper [D] to remove the I/Q imbalance [106-107]. The constellation plots of the received signal before and after equalization are shown in Fig. 4.12. 4000 samples are used for phase averaging to get a higher SNR. With equalization and averaging, the total distance estimation error is less than $7 \mu\text{m}$, as Fig. 4.13 shows.

In paper [E], equalization is not applied. The phases calculated from all subcarriers are used for averaging. The total distance error is less than $22 \mu\text{m}$, as Fig. 4.14 shows

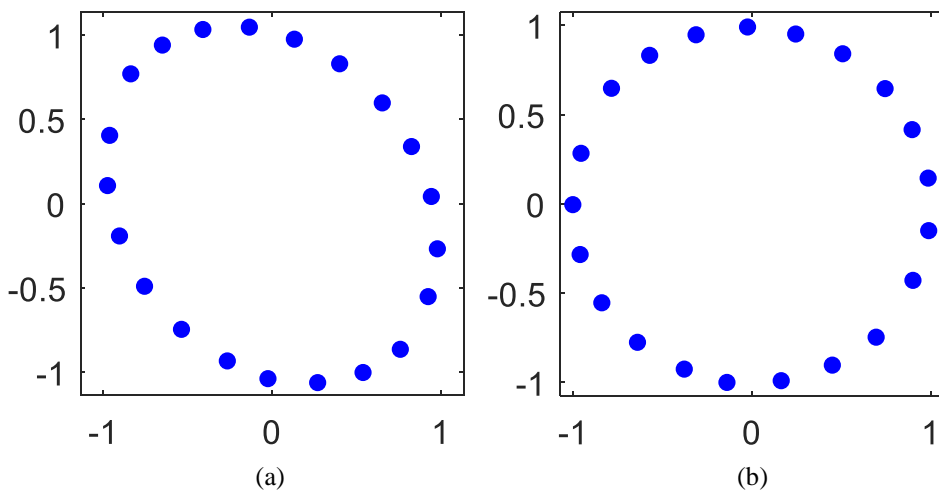


Fig. 4.12 The constellation points (a) in an I/Q imbalanced system, (b) after equalization [D].

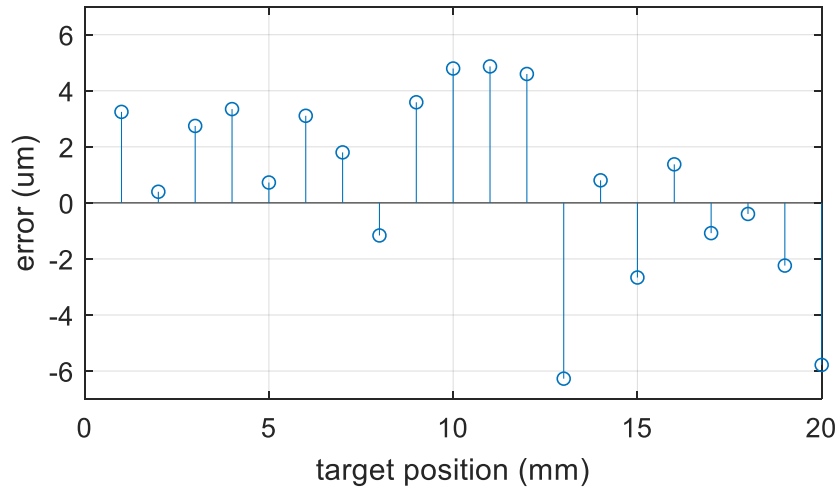


Fig. 4.13 The distance error versus target distance [D].

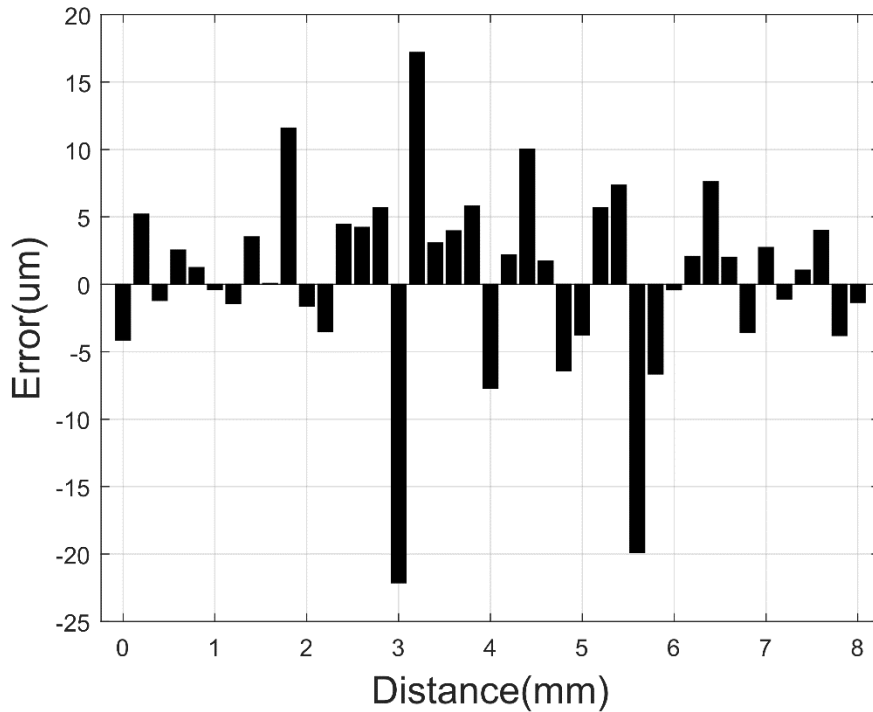


Fig. 4.14 The distance error versus target distance [E].

4.4.3 Discussion

In the proposed two radar systems, the principles of coarse estimation are different. For RBPM radar, the time domain signal is used for estimation. For OFDM radar, the phase offsets of different frequencies subcarrier are used. Both radar systems can be used in a multi-user scenario since they all carry user-specified signature data, which also enable possibilities of realizing radar sensing and communication simultaneously. For OFDM radar, when the bandwidth occupation is larger than 1 GHz, the frequency response ripple of the transceiver will limit the estimation accuracy.

Chapter 5

Conclusions and future work

5.1 Conclusions

In this thesis, two properties of the millimeter-wave are utilized for different applications, wide available bandwidth and short wavelength. Wide available bandwidth enables possibilities to realize high-speed communication systems. Its short wavelength provides opportunities for achieving high accuracy radar sensing. Besides these opportunities, there are also challenges that come along.

Realizing wideband high-speed real-time communication is a challenge. An overview of published millimeter-wave communication demonstrators shows that the real-time transmissions are limited either with low data rates or with low modulation order signals due to lack of real-time wideband carrier synchronization solution. It is difficult to adopt traditional digital synchronization solutions at a higher data rate due to commercial ADCs sampling rate limitation. Two analog-digital hybrid CR solutions [A][B] are proposed as an alternative. These CR solutions are modulation scheme independent and have no data rate restriction. They solve the problem of real-time wideband signal synchronization and avoids using high-speed ADCs. These solutions are also compared in this thesis. Communication links are successfully demonstrated at the E band with the highest data rate of 24 Gbps and the highest modulation order scheme of 64-QAM.

High-frequency synthesis for millimeter-wave is another challenge. The frequency divider is an essential part of high-frequency synthesizers. A wideband frequency divider is desired to have a reconfigurable divide ratio for matching a large range of VCO frequencies to a fixed reference frequency. An overview of published millimeter-wave frequency dividers shows that dual-mode frequency dividers are very rare, and most of them work with low working frequencies and narrow bandwidths. In this thesis, a D-band dual-mode frequency divider [C] is introduced. The dual-mode division is achieved by adding a tunable delay into the traditional injection lock frequency divider structure. Compared with previously published relevant works in Table 3.3, the proposed frequency divider demonstrates the highest input frequency (160 GHz) among the dividers that have dual-modulus, divide-by-2 and divide-by-3, and a state-of-the-art operational bandwidth (41.5%) among divide-by-3 dividers.

For millimeter-wave radar sensors, achieving both high accuracy and long unambiguous measurement distance is a challenge. Besides, we also want the radar can be used in a multi-user scenario. Traditional CW, FMCW, phase modulated, and OFDM radar all have their advantages and shortages. By combining the high-accuracy CW radar with the phase modulated radar or OFDM radar that has a long unambiguous measurement distance, the desired millimeter-wave radar can be realized. Two radar systems [D][E] use this idea to achieve high accuracy of micrometer level with an unambiguous measurement distance potentially over one kilometer. Since both radar systems have the ability to carry data, the signature code can be used to support them work in a multi-user scenario.

5.2 Future work

For the communication applications, the proposed CR solutions are only part of the system. Demodulating symbols to bitstream is yet to be studied. It can be done with high-speed ADCs with few effective bits, or alternatively, a new Intel FPGA that is able to receive four pulse amplitude modulation (PAM-4) signals up to 28.9 GBaud [108] can also be used. For example, by using two channels of this FPGA, a 16-QAM signal can be demodulated. More demodulation solutions can be further investigated.

As discussed in Chapter II, the PN sequence used for carrier recovery can also be used for distinguishing two channels in a MIMO system. It is interesting to build a MIMO system with PN pilots and test its performance. This concept is not yet tested. A full study of the advantages and limitations of this would be carried out in the future.

The multi-radar scenario is desired in industrial applications. The proposed radar system [D][E] can be further tested in a multi-radar scenario to see how much accuracy degradation would happen. Furthermore, a radar-communication system is possible to be built with the proposed radar systems.

Acknowledgment

It really has been a long journey and finally comes to the final stage. Looking back to the past five years, I truly believe I am so lucky. There were many self-doubt moments that I feel I can never make it. And there was always someone who helps me to get through it. I want to take this opportunity to express my gratitude to the people who have supported me throughout this journey.

First of all, I would like to thank my main supervisor and examiner Prof. Herbert Zirath for giving me this great opportunity to work and study in MEL as a Ph.D. student. I am grateful for all the support and guidance you gave. I admire your rigorous attitude and enthusiasm towards scientific research. You give me a clear image of what a researcher looks like. You are a role model to me and inspire me to take my work forward. Also, I want to thank my co-supervisor Assoc. Prof. Zhongxia Simon He for his help and support in both my work and life. You taught me how to do research from the very beginning and helped me to adapt the life in Sweden. Thank you for your understanding, encouragement, and so much care during those dark days of mine. I truly appreciate that you were always available when I need help. I would like to thank my co-supervisor, Dr. Yinggang Li, for his expert advice and feedback. I appreciate that you were always trying to help me when I have problems. Your valuable advice always inspired me. I would also like to thank my friend and co-worker, Dr. Jingjing Chen. When I started my Ph.D. study, you spent a lot of time helping me with the measurement, writing, and courses. I am grateful that you were always such supportive and kind.

I also want to thank my best friend Kai-Hsin Wen for so much company and joy you gave. It must be fate that you asked me to hang out last year. From that moment, I finally started to enjoy life in Sweden and discover all the wonderful things all around. Thank you, Yin and Dingyuan, for being such good friends and giving me so much warm company and support. Thank you, Frida, for always supporting me, putting up with my complaints, and giving me encouragement. Thanks my friend, Han and Junjie, for all the relaxing lunch, fika, parties that we had together. I cherish all these good memories with you. I want to thank my office mates Dhecha and Stavros, as well as my friend Hassona. We started our Ph.D. study more or less at the same time. It is such a pleasure to be in the same group and do research with you guys. We kept each other company for more than five years. I genuinely wish you all good luck with your career. I also owe my thanks to all my colleagues for creating such a pleasant environment to work with you.

I would like to express my gratitude to my aunt Aimin Wang for her caring and encouragement. You gave me so much emotional support and made me feel at home when I first came to Sweden.

Jax, thank you for showing up in my life and bringing me so much joy and laughter. I can't wait to explore this wonderful world with you. Although I hated that you always push me to work on my thesis, I guess I owe you my thanks for that as well.

Last but not least, I want to thank my family for their unconditional love, greatest support, and faith in me. Thank you for telling me it is ok to be just an ordinary person and letting me choose my own way. You never give me pressure but always being my strongest backup. Thank you, and I love you the most.

This research was financed in part by the Swedish Foundation for Strategic Research (SSF) under Project SE13-0020 "High Datarate Wireless Communications (100G)" and in part by the Car2TERA project, which has received funding from the European Union's Horizon 2020 research and innovation program under grant agreement No. 824962.

References

- [1] "Ericsson mobility report," Ericsson AB, November 2020.
- [2] "To be first in 5G, first get to the core, " Ericsson AB, 2018.
- [3] T. S. Rappaport, S. Sun, R. Mayzus, H. Zhao, Y. Azar, K. Wang, G. N. Wong, J. K. Schulz, M. Samimi, and F. Gutierrez, "Millimeter-wave Mobile Communications for 5G Cellular: It Will Work," in *IEEE Access*, vol. 1, pp. 335-349, 2013.
- [4] "5G deployment considerations, " Ericsson AB, 2018.
- [5] "Ericsson White paper, " Ericsson AB, January 2017.
- [6] "Ericsson microwave outlook, " Ericsson AB, December 2017.
- [7] P. Sharma, "Evolution of mobile wireless communication networks-1G to 5G as well as future prospective of next generation communication network." *International Journal of Computer Science and Mobile Computing*, vol. 2, pp. 47-53, August 2013.
- [8] M. I. Baba, N. Nafees, I. Manzoor, K. A. Naik, and S. Ahmed, "Evolution of Mobile Wireless Communication Systems from 1G to 5G: A Comparative Analysis," in *International Journal of Scientific Research in Computer Science, Engineering and Information Technology*, vol. 4, issue 1, April 2018.
- [9] A. U. Gawas, "An overview on evolution of mobile wireless communication networks: 1G-6G," *International Journal on Recent and Innovation Trends in Computing and Communication*, vol. 3, no. 5, pp. 3230-3133, May 2015.
- [10] "Ericsson mobility report," Ericsson AB, November 2019.
- [11] M. Jaber, M. A. Imran, R. Tafazolli, and A. Tukmanov, "5G Backhaul Challenges and Emerging Research Directions: A Survey," in *IEEE Access*, vol. 4, pp. 1743-1766, 2016.
- [12] J. R. Pierce, "Symbol signal and noise," 1961.
- [13] Y. Niu, Y. Li, D. Jin, L. Su, and A. V. Vasilakos, "A survey of millimeter wave communications (mmWave) for 5G: opportunities and challenges." *Wireless networks*, 2015, 21.8: 2657-2676.
- [14] S. Carpenter, Z. He, M. Bao and H. Zirath, "A Highly Integrated Chipset for 40 Gbps Wireless D-Band Communication Based on a 250 nm InP DHBT Technology," *2014 IEEE Compound Semiconductor Integrated Circuit Symposium (CSICS)*, La Jolla, CA, 2014, pp. 1-4.

- [15] Y. Li, M. Hörberg, K. Eriksson, J. Campion, A. Hassona, S. Vecchiattini, T. Dahl, R. Lindman, M. Bao, Z. S. He, F. Dielacher, J. Oberhammer, H. Zirath, and J. Hansryd, "D-band SiGe transceiver modules based on silicon-micromachined integration," *2019 IEEE Asia-Pacific Microwave Conference (APMC)*, 2019, pp. 883-885, doi: 10.1109/APMC46564.2019.9038198.
- [16] D. Lopez-Diaz, I. Kallfass, A. Tessmann, A. Leuther, S. Wagner, M. Schlechtweg, and O. Ambacher, "A subharmonic chipset for gigabit communication around 240 GHz," *2012 IEEE/MTT-S International Microwave Symposium Digest*, 2012, pp. 1-3, doi: 10.1109/MWSYM.2012.6258404.
- [17] N. Pohl, H. Rein, T. Musch, K. Aufinger and J. Hausner, "SiGe Bipolar VCO With Ultra-Wide Tuning Range at 80 GHz Center Frequency," in *IEEE Journal of Solid-State Circuits*, vol. 44, no. 10, pp. 2655-2662, Oct. 2009, doi: 10.1109/JSSC.2009.2026822.
- [18] J. Al-Eryani et al., "Wideband 148–188 GHz push-push VCO using variable inductance and capacitance," *2016 11th European Microwave Integrated Circuits Conference (EuMIC)*, London, UK, 2016, pp. 313-316, doi: 10.1109/EuMIC.2016.7777553.
- [19] S. Breun, M. Voelkel, A. M. Schrotz, M. Dietz, V. Issakov and R. Weigel, "A Low-Power 14% FTR Push-Push D-Band VCO in 130 nm SiGe BiCMOS Technology with -178 dBc/Hz FOMT," *2020 IEEE 20th Topical Meeting on Silicon Monolithic Integrated Circuits in RF Systems (SiRF)*, 2020, pp. 39-42, doi: 10.1109/SIRF46766.2020.9040174.
- [20] Y. Baeyens and Y. K. Chen, "A monolithic integrated 150 GHz SiGe HBT push-push VCO with simultaneous differential V-band output," *IEEE MTT-S International Microwave Symposium Digest*, 2003, Philadelphia, PA, USA, 2003, pp. 877-880 vol.2, doi: 10.1109/MWSYM.2003.1212509.
- [21] S. Shahramian et al., "Design of a Dual W- and D-band PLL," *IEEE Journal of Solid-State Circuits*, vol. 46, pp. 1011–1022, May 2011.
- [22] M. Seo, M. Urteaga, M. Rodwell and M. Choe, "A 300 GHz PLL in an InP HBT technology," *2011 IEEE MTT-S International Microwave Symposium*, 2011, pp. 1-1, doi: 10.1109/MWSYM.2011.5973453.
- [23] S. Shahramian, A. Hart, A. Chan Carusone, P. Garcia, P. Chevalier and S. P. Voinigescu, "A D-band PLL covering the 81–82 GHz, 86–92 GHz and 162–164 GHz bands," *2010 IEEE Radio Frequency Integrated Circuits Symposium*, 2010, pp. 53-56, doi: 10.1109/RFIC.2010.5477284.
- [24] C. Cao, Y. Ding and K. K. O, "A 50-GHz Phase-Locked Loop in 0.13 μ m CMOS," in *IEEE Journal of Solid-State Circuits*, vol. 42, no. 8, pp. 1649-1656, Aug. 2007, doi: 10.1109/JSSC.2007.900289.
- [25] K. Tsai and S. Liu, "A 43.7mW 96GHz PLL in 65nm CMOS," *2009 IEEE International Solid-State Circuits Conference - Digest of Technical Papers*, 2009, pp. 276-277,277a, doi: 10.1109/ISSCC.2009.4977415.

- [26] C. Wagner, A. Stelzer and H. Jager, "PLL Architecture for 77-GHz FMCW Radar Systems with Highly-Linear Ultra-Wideband Frequency Sweeps," *2006 IEEE MTT-S International Microwave Symposium Digest*, 2006, pp. 399-402, doi: 10.1109/MWSYM.2006.249555.
- [27] J. Lee, M. Liu and H. Wang, "A 75-GHz Phase-Locked Loop in 90-nm CMOS Technology," in *IEEE Journal of Solid-State Circuits*, vol. 43, no. 6, pp. 1414-1426, June 2008, doi: 10.1109/JSSC.2008.922719.
- [28] G. Durisi, and S. Benedetto, "Comparison between coherent and noncoherent receivers for UWB communications." *EURASIP Journal on Advances in Signal Processing* 2005. 3: 1-10.
- [29] Z. He, J. Chen, C. Svensson, L. Bao, A. Rhodin, Y. Li, J. An and H. Zirath, "A Hardware Efficient Implementation of a Digital Baseband Receiver for High-Capacity Millimeter-Wave Radios," in *IEEE Transactions on Microwave Theory and Techniques*, vol. 63, no. 5, pp. 1683-1692, May 2015.
- [30] S. Huang, Y. Yeh, H. Wang, P. Chen and J. Lee, "W-Band BPSK and QPSK Transceivers with Costas-Loop Carrier Recovery in 65-nm CMOS Technology," in *IEEE Journal of Solid-State Circuits*, vol. 46, no. 12, pp. 3033-3046, December 2011.
- [31] C. Wang , B. Lu, C. Lin, Q. Chen, L. Miao, X. Deng and J. Zhang, "0.34-THz Wireless Link Based on High-Order Modulation for Future Wireless Local Area Network Applications," in *IEEE Transactions on Terahertz Science and Technology*, vol. 4, no. 1, pp. 75-85, Jan. 2014.
- [32] P. Rodríguez-Vázquez, J. Grzyb, N. Sarmah, B. Heinemann and U. R. Pfeiffer, "A 65 Gbps QPSK one meter wireless link operating at a 225–255 GHz tunable carrier in a SiGe HBT technology," *2018 IEEE Radio and Wireless Symposium (RWS)*, Anaheim, CA, 2018, pp. 146-149.
- [33] T. Nagatsuma, "Breakthroughs in Photonics 2013: THz Communications Based on Photonics," in *IEEE Photonics Journal*, vol. 6, no. 2, pp. 1-5, April 2014, Art no. 0701505.
- [34] S. Carpenter, D. Nopchinda, M. Abbasi, Z. S. He, M. Bao, T. Eriksson and H. Zirath, "A D-Band 48-Gbit/s 64-QAM/QPSK Direct-Conversion I/Q Transceiver Chipset," in *IEEE Transactions on Microwave Theory and Techniques*, vol. 64, no. 4, pp. 1285-1296, April 2016.
- [35] H. Song, J. Kim, K. Ajito, N. Kukutsu and M. Yaita, "50-Gb/s Direct Conversion QPSK Modulator and Demodulator MMICs for Terahertz Communications at 300 GHz," in *IEEE Transactions on Microwave Theory and Techniques*, vol. 62, no. 3, pp. 600-609, March 2014.
- [36] I. Kallfass , J. Antes, T. Schneider, F. Kurz, D. Lopez-Diaz, S. Diebold, H. Massler, A. Leuther and A. Tessmann, "All Active MMIC-Based Wireless Communication at 220 GHz," in *IEEE Transactions on Terahertz Science and Technology*, vol. 1, no. 2, pp. 477-487, November 2011.

- [37] I. Ando, M. Tanio, M. Ito, T. Kuwabara, T. Marumoto and K. Kunihiro, "Wireless D-band communication up to 60 Gbit/s with 64QAM using GaAs HEMT technology," *2016 IEEE Radio and Wireless Symposium (RWS)*, Austin, TX, 2016, pp. 193-195.
- [38] K. Katayama, K. Takano, S. Amakawa, S. Hara, T. Yoshida and M. Fujishima, "CMOS 300-GHz 64-QAM transmitter," *2016 IEEE MTT-S International Microwave Symposium (IMS)*, San Francisco, CA, 2016, pp. 1-4.
- [39] F. Boes, T. Messinger, J. Antes, D. Meier, A. Tessmann, A. Inam and I. Kallfass, "Ultra-broadband MMIC-based wireless link at 240 GHz enabled by 64GS/s DAC," *2014 39th International Conference on Infrared, Millimeter, and Terahertz waves (IRMMW-THz)*, Tucson, AZ, 2014, pp. 1-2.
- [40] C. Lin, B. Lu, C. Wang and Q. Wu, "A 2×40 Gbps wireless communication system using 0.14 THz band oritho-mode transducer," *2015 40th International Conference on Infrared, Millimeter, and Terahertz waves (IRMMW-THz)*, Hong Kong, 2015, pp. 1-2.
- [41] K. Katayama, K. Takano, S. Amakawa, S. Hara, A. Kasamatsu, K. Mizuno, K. Takahashi, T. Yoshida and M. Fujishima, "A 300 GHz CMOS Transmitter With 32-QAM 17.5 Gb/s/ch Capability Over Six Channels," in *IEEE Journal of Solid-State Circuits*, vol. 51, no. 12, pp. 3037-3048, Dec. 2016.
- [42] H. Hamada, T. Fujimura, I. Abdo, K. Okada, H. J. Song, H. Sugiyama, H. Matsuzaki and H. Nosaka, "300-GHz. 100-Gb/s InP-HEMT Wireless Transceiver Using a 300-GHz Fundamental Mixer," *2018 IEEE/MTT-S International Microwave Symposium (IMS)*, Philadelphia, PA, 2018, pp. 1480-1483.
- [43] V. Vassilev, Z. S. He, S. Carpenter, H. Zirath, Y. Yan, A. Hassona, M. Bao, T. Emanuelsson, J. Chen, M. Horberg, Y. Li and J. Hansrydl, "Spectrum Efficient D-band Communication Link for Real-time Multi-gigabit Wireless Transmission," *2018 IEEE/MTT-S International Microwave Symposium (IMS)*, Philadelphia, PA, 2018, pp. 1523-1526.
- [44] H. Takahashi, A. Hirata, J. Takeuchi, N. Kukutsu, T. Kosugi and K. Murata, "120-GHz-band 20-Gbit/s transmitter and receiver MMICs using quadrature phase shift keying," *2012 7th European Microwave Integrated Circuit Conference*, Amsterdam, 2012, pp. 313-316.
- [45] K. K. Tokgoz, S. Maki, J. Pang, N. Nagashima, I. Abdo, S. Kawai, T. Fujimura, Y. Kawano, T. Suzuki, T. Iwai and K. Okada, "A 120Gb/s 16QAM CMOS millimeter-wave wireless transceiver," *2018 IEEE International Solid - State Circuits Conference (ISSCC)*, San Francisco, CA, 2018, pp. 168-170.
- [46] Z. He, D. Nopchinda, T. Swahn and H. Zirath, "A 15-Gb/s 8-PSK Demodulator With Comparator-Based Carrier Synchronization," in *IEEE Transactions on Microwave Theory and Techniques*, vol. 63, no. 8, pp. 2630-2637, Aug. 2015.
- [47] P. Harati, A. Dyskin and I. Kallfass, "Analog Carrier Recovery for Broadband Wireless Communication Links," *2018 48th European Microwave Conference (EuMC)*, Madrid, Spain, 2018, pp. 1401-1404.

- [48] "Multi-band booster, enabling 5G transport everywhere" [Online]. Available: <https://www.ericsson.com/en/mobile-transport/multiband/>
- [49] S. Vaidya, P. Ambad, and S. Bhosle. "Industry 4.0—a glimpse." *Procedia manufacturing*, 2018, 20: 233-238.
- [50] M. Ghobakhloo, "Industry 4.0, digitization, and opportunities for sustainability." *Journal of Cleaner Production*, 2020, 252: 119869.
- [51] L. Xu, E. L. Xu, and L. Li. "Industry 4.0: state of the art and future trends." *International Journal of Production Research*, 2018, 56.8: 2941-2962.
- [52] A. Rojko, "Industry 4.0 concept: Background and overview." *International Journal of Interactive Mobile Technologies*, 2017, 11.5.
- [53] "Connected Manufacturing: A guide to Industry 4.0 transformation with private cellular technology," Ericsson AB, November 2020.
- [54] N. Taylor, "LASER: The inventor, the Nobel laureate, and the thirty-year patent war. " Simon and Schuster, 2002.
- [55] M. Wachspress, "Ultrasonic Doppler for Distance Measurement," in *IRE Transactions on Ultrasonic Engineering*, vol. 8, no. 1, pp. 6-13, March 1961, doi: 10.1109/T-PGUE.1961.29273.
- [56] M. Tanter and M. Fink, "Ultrafast imaging in biomedical ultrasound," in *IEEE Transactions on Ultrasonics, Ferroelectrics, and Frequency Control*, vol. 61, no. 1, pp. 102-119, January 2014, doi: 10.1109/TUFFC.2014.2882.
- [57] S. S. D. Jones, "Technical History of the Beginnings of Radar." *The Journal of Navigation*, 1988, 41.3: 443-444.
- [58] A. Ç. Ulusoy and H. Schumacher, "Multi-Gb/s Analog Synchronous QPSK Demodulator with Phase-Noise Suppression," in *IEEE Transactions on Microwave Theory and Techniques*, vol. 60, no. 11, pp. 3591-3598, Nov. 2012.
- [59] T. Tsukizawa, "A fully integrated 60-GHz CMOS transceiver chipset based on WiGig/IEEE 802.11ad with built-in self calibration for mobile usage", *IEEE Journal of Solid-State Circuits*, vol. 48, no. 12, pp. 3146-3159, Dec. 2013.
- [60] V. Dyadyuk, "A multigigabit millimeter-wave communication system with improved spectral efficiency", in *IEEE Transactions on Microwave Theory and Techniques*, vol. 55, no. 12, pp. 2813-2821, Dec. 2007.
- [61] M. S. Kang, B. S. Kim, K. S. Kim, W. J. Byun, H. C. Park, "16-QAM-based highly spectral-efficient e-band communication system with bit rate up to 10 Gbit/s", *ETRI Journal*, vol. 34, no. 5, pp. 649-654, Oct. 2012.
- [62] K. Okada, "A full four-channel 6.3-Gb/s 60-GHz CMOS transceiver with low-power analog and digital baseband circuitry", *IEEE Journal of Solid-State Circuits*, vol. 48, no. 1, pp. 46-65, Jan. 2013.

- [63] Z. He, D. Kuylenstierna, S. Lai and H. Zirath, "A 12 Gbps analog QPSK baseband receiver based on injection-locked VCO," *2015 IEEE MTT-S International Microwave Symposium*, Phoenix, AZ, 2015, pp. 1-4.
- [64] A. Spalvieri and L. Barletta, "Pilot-Aided Carrier Recovery in the Presence of Phase Noise," in *IEEE Transactions on Communications*, vol. 59, no. 7, pp. 1966-1974, July 2011, doi: 10.1109/TCOMM.2011.051311.100047.
- [65] N. Noels, H. Steendam, M. Moeneclaey and H. Bruneel, "Carrier phase and frequency estimation for pilot-symbol assisted transmission: bounds and algorithms," in *IEEE Transactions on Signal Processing*, vol. 53, no. 12, pp. 4578-4587, Dec. 2005, doi: 10.1109/TSP.2005.859318.
- [66] F. Rice, "Carrier-phase and frequency-estimation bounds for transmissions with embedded reference symbols," in *IEEE Transactions on Communications*, vol. 54, no. 2, pp. 221-225, Feb. 2006, doi: 10.1109/TCOMM.2005.863782.
- [67] R. L. Peterson, R. E. Ziemer, and D. E. Borth. "An introduction to spread-spectrum communications. " Prentice-Hall, Inc., 1995.
- [68] S. Randel, R. Ryf, A. Sierra, P. Winzer, A. Gnauck, C. Bolle, R. Essiambre, D. Peckham, A. McCurdy, and R. Lingle, "6×56-Gb/s mode-division multiplexed transmission over 33-km few-mode fiber enabled by 6×6 MIMO equalization," *Optics Express*, 2011, 19.17: 16697-16707.
- [69] P. Chiang, Z. Wang, O. Momeni and P. Heydari, "14.7 A 300GHz frequency synthesizer with 7.9% locking range in 90nm SiGe BiCMOS," *2014 IEEE International Solid-State Circuits Conference Digest of Technical Papers (ISSCC)*, San Francisco, CA, USA, 2014, pp. 260-261, doi: 10.1109/ISSCC.2014.6757426.
- [70] S. Kang, J. Chien and A. M. Niknejad, "A W-Band Low-Noise PLL With a Fundamental VCO in SiGe for Millimeter-Wave Applications," in *IEEE Transactions on Microwave Theory and Techniques*, vol. 62, no. 10, pp. 2390-2404, Oct. 2014, doi: 10.1109/TMTT.2014.2345342.
- [71] K. Tan, T. Chu and S. S. H. Hsu, "A 76.2–89.1 GHz Phase-Locked Loop With 15.6% Tuning Range in 90 nm CMOS for W-Band Applications," in *IEEE Microwave and Wireless Components Letters*, vol. 25, no. 8, pp. 538-540, Aug. 2015, doi: 10.1109/LMWC.2015.2440765.
- [72] S. Zeinolabedinzadeh, I. Song, M. Kaynak and J. D. Cressler, "A Wide Locking-Range, Low Phase-Noise and High Output Power D-Band SiGe PLL," *2020 IEEE 20th Topical Meeting on Silicon Monolithic Integrated Circuits in RF Systems (SiRF)*, San Antonio, TX, USA, 2020, pp. 35-38, doi: 10.1109/SIRF46766.2020.9040189.
- [73] Y. Chao, H. C. Luong and Z. Hong, "Analysis and Design of a 14.1-mW 50/100-GHz Transformer-Based PLL With Embedded Phase Shifter in 65-nm CMOS," in *IEEE Transactions on Microwave Theory and Techniques*, vol. 63, no. 4, pp. 1193-1201, April 2015, doi: 10.1109/TMTT.2015.2407364.

- [74] P. Zhou, J. Chen, P. Yan, D. Hou and W. Hong, "A low power, high sensitivity SiGe HBT static frequency divider up to 90 GHz for millimeter-wave application," in *China Communications*, vol. 16, no. 2, pp. 85-94, Feb. 2019, doi: 10.12676/j.cc.2019.02.006.
- [75] Y. N. Miao, C. C. Boon, M. A. Do, K. S. Yeo, and Y. X. Zhang, "High-frequency low-power LC divide-by-2/3 injection-locked frequency divider." in *Microwave and Optical Technology Letters*, 2011, 53.2: 337-340.
- [76] S. Jang, C. Lin and C. Lee, "A Low Voltage 0.35 μm CMOS Frequency Divider With the Body Injection Technique," in *IEEE Microwave and Wireless Components Letters*, vol. 18, no. 7, pp. 470-472, July 2008, doi: 10.1109/LMWC.2008.925117.
- [77] S. Jang, C. Lee and W. Yeh, "A Divide-by-3 Injection Locked Frequency Divider With Single-Ended Input," in *IEEE Microwave and Wireless Components Letters*, vol. 18, no. 2, pp. 142-144, Feb. 2008, doi: 10.1109/LMWC.2007.915142.
- [78] S. Jang, R. Yang, C. Chang and M. Juang, "Multi-Modulus LC Injection-Locked Frequency Dividers Using Single-Ended Injection," in *IEEE Microwave and Wireless Components Letters*, vol. 19, no. 5, pp. 311-313, May 2009, doi: 10.1109/LMWC.2009.2017599.
- [79] W. Zhang, L. Zhang, X. Zhang and Y. Liu, "A dual-modulus injection-locked frequency divider with large locking range." in *Microwave and Optical Technology Letters*, 2013, 55.2: 269-272.
- [80] W. Gao, W. Zhang and Y. Liu. "A wide locking range and low power divide-by-2/3 LC injection-locked frequency divider." in *Journal of Circuits, Systems and Computers*, 2016, 25.02: 1650013.
- [81] H. Seo, J. Yun and J. S. Rieh, "SiGe 140 GHz ring-oscillator-based injection-locked frequency divider," in *Electronics letters*, vol. 48, no. 14, pp. 847-848, July 5, 2012.
- [82] Y. Lin, K. Lan and Y. Lin, "W-Band Divide-by-3 Injection-Locked Frequency Divider Using Stacked Cross-Coupled Transistors in 90 nm CMOS," *2019 IEEE Radio and Wireless Symp. (RWS)*, Orlando, FL, USA, 2019, pp. 1-4.
- [83] P. Feng and S. Liu, "Divide-by-Three Injection-Locked Frequency Dividers Over 200 GHz in 40-nm CMOS," in *IEEE Journal of Solid-State Circuits*, vol. 48, no. 2, pp. 405-416, Feb. 2013, doi: 10.1109/JSSC.2012.2223932.
- [84] Hsieh-Hung Hsieh et al., "A V-band divide-by-three differential direct injection-locked frequency divider in 65-nm CMOS," *IEEE Custom Integrated Circuits Conference 2010*, San Jose, CA, 2010, pp. 1-4.
- [85] U. Ali, M. Bober, A. Thiede and S. Wagner, "100–166 GHz wide band high speed digital dynamic frequency divider design in 0.13 μm SiGe BiCMOS technology," *2015 10th European Microwave Integrated Circuits Conference (EuMIC)*, 2015, pp. 73-76, doi: 10.1109/EuMIC.2015.7345071.

- [86] J. Al-Eryani et al., "A 47–217 GHz dynamic frequency divider in SiGe technology," *2015 IEEE Bipolar/BiCMOS Circuits and Technology Meeting (BCTM)*, Boston, MA, 2015, pp. 125-128.
- [87] J. Al-Eryani et al., "A 9-81/38-189 GHz Dual-Band Switchable Dynamic Frequency Divider," *2015 IEEE Compound Semiconductor Integrated Circuit Symposium (CSICS)*, 2015, pp. 1-4, doi: 10.1109/CSICS.2015.7314474.
- [88] U. Ali, M. Bober, A. Thiede, A. Awny and G. Fischer, "High speed static frequency divider design with 111.6 GHz self-oscillation frequency (SOF) in 0.13 μm SiGe BiCMOS technology," *2015 German Microwave Conference*, 2015, pp. 241-243, doi: 10.1109/GEMIC.2015.7107798.
- [89] H. Knapp et al., "168 GHz dynamic frequency divider in SiGe:C bipolar technology," *2009 IEEE Bipolar/BiCMOS Circuits and Technology Meeting*, 2009, pp. 190-193, doi: 10.1109/BIPOL.2009.5314242.
- [90] B. Sene, H. Knapp, D. Reiter and N. Pohl, "A 122-242 GHz Dynamic Frequency Divider in an Advanced BiCMOS Technology," *2020 15th European Microwave Integrated Circuits Conference (EuMIC)*, 2021, pp. 296-299.
- [91] E. Laskin and A. Rylyakov, "A 136-GHz Dynamic Divider in SiGe Technology," *2009 IEEE Topical Meeting on Silicon Monolithic Integrated Circuits in RF Systems*, 2009, pp. 1-4, doi: 10.1109/SMIC.2009.4770526.
- [92] S. Scherr, B. Göttel, S. Ayhan, A. Bhutani, M. Pauli, W. Winkler, J. C. Scheytt, and T. Zwick, "Miniaturized 122 GHz ISM band FMCW radar with micrometer accuracy," in *Proc. Eur. Radar Conf. (EuRAD)*, Sep. 2015, pp. 277-280
- [93] M. Pauli, B. Göttel, S. Scherr, A. Bhutani, S. Ayhan, W. Winkler, and T. Zwick, "Miniaturized 122 GHz ISM band FMCW radar with micrometer accuracy," *2015 European Radar Conference (EuRAD)*, 2015, pp. 277-280, doi: 10.1109/EuRAD.2015.7346291.
- [94] S. Ayhan, S. Thomas, N. Kong, S. Scherr, M. Pauli, T. Jaeschke, J. Wulfsberg, N. Pohl, and T. Zwick, "Millimeter-wave radar distance measurements in micro machining," *2015 IEEE Topical Conference on Wireless Sensors and Sensor Networks (WiSNet)*, 2015, pp. 65-68, doi: 10.1109/WISNET.2015.7127413.
- [95] S. Trotta et al., "An RCP Packaged Transceiver Chipset for Automotive LRR and SRR Systems in SiGe BiCMOS Technology," in *IEEE Transactions on Microwave Theory and Techniques*, vol. 60, no. 3, pp. 778-794, March 2012, doi: 10.1109/TMTT.2011.2181536.
- [96] J. Lee, Y. Li, M. Hung and S. Huang, "A Fully-Integrated 77-GHz FMCW Radar Transceiver in 65-nm CMOS Technology," in *IEEE Journal of Solid-State Circuits*, vol. 45, no. 12, pp. 2746-2756, Dec. 2010, doi: 10.1109/JSSC.2010.2075250.
- [97] F. Barbon, G. Vinci, S. Lindner, R. Weigel and A. Koelpin, "A six-port interferometer based micrometer-accuracy displacement and vibration measurement radar," *2012 IEEE/MTT-S International Microwave Symposium Digest*, 2012, pp. 1-3, doi: 10.1109/MWSYM.2012.6259624.

- [98] S. Lindner, F. Barbon, S. Mann, G. Vinci, R. Weigel and A. Koelpin, "Dual tone approach for unambiguous six-port based interferometric distance measurements," *2013 IEEE MTT-S International Microwave Symposium Digest (MTT)*, 2013, pp. 1-4, doi: 10.1109/MWSYM.2013.6697581.
- [99] F. Strömbeck, Z. S. He, H. Zirath, "AMCW Radar of Micrometer Accuracy Distance Measurement and Monitoring," *2019 IEEE MTT-S International Microwave Symposium (IMS)*, Boston, MA, USA, 2019, pp. 1473-1475.
- [100] H. Yang, and J. Chen, "Design of Costas/PSK continuous wave LPI radar signal." in *International Journal of Electronics*, 2017, 104.3: 404-415.
- [101] R. Feger, H. Haderer, H. Jalli Ng and A. Stelzer, "Realization of a Sliding-Correlator-Based Continuous-Wave Pseudorandom Binary Phase-Coded Radar Operating in W Band," in *IEEE Transactions on Microwave Theory and Techniques*, vol. 64, no. 10, pp. 3302-3318, Oct. 2016, doi: 10.1109/TMTT.2016.2600321.
- [102] S. R. J. Axelsson, "Noise radar using random phase and frequency modulation," in *IEEE Transactions on Geoscience and Remote Sensing*, vol. 42, no. 11, pp. 2370-2384, Nov. 2004, doi: 10.1109/TGRS.2004.834589.
- [103] Liu Guosui, Gu Hong and Su Weimin, "Development of random signal radars," in *IEEE Transactions on Aerospace and Electronic Systems*, vol. 35, no. 3, pp. 770-777, July 1999, doi: 10.1109/7.784050.
- [104] V. Giannini et al., "A 79 GHz Phase-Modulated 4 GHz-BW CW Radar Transmitter in 28 nm CMOS," in *IEEE Journal of Solid-State Circuits*, vol. 49, no. 12, pp. 2925-2937, Dec. 2014, doi: 10.1109/JSSC.2014.2355819.
- [105] C. Sturm and W. Wiesbeck, "Waveform Design and Signal Processing Aspects for Fusion of Wireless Communications and Radar Sensing," in *Proceedings of the IEEE*, vol. 99, no. 7, pp. 1236-1259, July 2011, doi: 10.1109/JPROC.2011.2131110.
- [106] J. Tubbax, B. Come, L. Van der Perre, L. Deneire, S. Donnay and M. Engels, "Compensation of IQ imbalance in OFDM systems," *IEEE International Conference on Communications*, 2003. ICC '03., Anchorage, AK, 2003, pp. 3403-3407 vol.5.
- [107] J. Tubbax, B. Come, L. Van der Perre, S. Donnay, M. Engels, Hugo De Man, M. Moonen, "Compensation of IQ imbalance and phase noise in OFDM systems," in *IEEE Transactions on Wireless Communications*, vol. 4, no. 3, pp. 872-877, May 2005.
- [108] "Intel Stratix 10 TX Device Overview", Intel, March 2020.

